Innovative Use of Earth Observation and Land Surface Modeling for Tracking the Effects of Irrigation on the Terrestrial Water Cycle

Sara Modanesi

Supervisor(s):

Prof. Dr. Eng. Gabriëlle De Lannoy
Dr. Eng. Christian Massari
Prof. Dr. Eng. Renato Morbidelli
Dr. Michel Bechtold

Members of the Examination Committee:

Prof. Dr. Eng. Renato Morbidelli
Prof. Dr. Eng. Gabriëlle De Lannoy
Dr. Michel Bechtold
Prof. Dr. Eng. Jan Diels
Prof.dr. Eng. Enrica Caporali
Prof. dr. Manuela Girotto

External Reviewers:

Prof. Dr. Eng. Viviana Maggioni
Prof. Dr. Eng. Susan Steele-Dunne

June 2022

Doctoraatsproefschrift nr. **1785** aan de faculteit Bio-ingenieurswetenschappen van de KU Leuven

Cover: Sentinel-1, the first in the family of Copernicus satellites, is used to monitor many aspects of our environment, from detecting and tracking oil spills and mapping sea ice to monitoring movement in land surfaces and mapping changes in the way land is used. It also plays a crucial role in providing timely information to help respond to natural disasters and assist humanitarian relief efforts. Credit: © ESA/ATG medialab

Uitgegeven in eigen beheer, SARA MODANESI, PERUGIA (ITALY)

UNIVERSITÀ
DEGLI STUDI
FIRENZE

DOTTORATO DI RICERCA IN INTERNATIONAL DOCTORATE IN CIVIL AND ENVIRONMENTAL ENGINEERING

CICLO XXXIV

COORDINATORE Prof. Luca Solari

Innovative Use of Earth Observation and Land Surface Modeling for Tracking the Effects of Irrigation on the Terrestrial Water Cycle

Settore Scientifico Disciplinare ICAR/02

Dottorando
Sara Modanesi

Tutor italiano
Prof. Eng. Renato Morbidelli

Co-Tutor italiano
Dott. Eng. Christian Massari

Tutor straniero
Prof. Eng. Gabriëlle De Lannoy

Co-Tutor straniero
Dott. Michel Bechtold

Coordinatore
Prof. Luca Solari

Anni 2018/2021

KU LEUVEN

ARENBERG DOCTORAL SCHOOL
FACULTY OF BIOSCIENCE ENGINEERING

Innovative Use of Earth Observation and Land Surface Modeling for Tracking the Effects of Irrigation on the Terrestrial Water Cycle

Sara Modanesi

Supervisor(s):

Prof. Dr. ir. Gabriëlle De Lannoy
Dr. ir. Christian Massari
Prof. Dr. ir. Renato Morbidelli
Dr. Michel Bechtold

January 2022

Abstract

In recent years, human water needs have been steadily increasing and they are currently dominated by agricultural activities for food production worldwide. Furthermore, the increase in population and climatic change are expected to raise the current demand of water highlighting the necessity for more efficient irrigation systems. In this context, the combined effect of human pressure (i.e. irrigation) and the increase of extreme natural phenomena, such as drought events, has a strong impact on the global water budget with a local depletion of water resources, especially groundwater. However, our understanding of the impact of human activities on the water cycle is challenged by the lack of data (such as irrigation benchmark data) and by the difficulty of land surface models (LSM) to represent human processes like irrigation. These knowledge gaps affect water and food security, because they undermine both the ability to accurately monitor and forecast drought events, and the capacity to safely manage water resources.

This thesis aims at shedding light on the utility of new earth observation (EO) data to characterize agricultural drought conditions and to detect water cycle modifications induced by anthropogenic activities like irrigation in order to help models to improve their ability to more realistically represent the terrestrial water cycle. Based on that, this research work tries to address two main important research questions:

1) What is the added value of new EO data (i.e., satellite-based soil moisture) in drought monitoring and to which extent are these data able to provide potential information on crop production with respect to LSMs?

2) Can the new generation of high resolution EO data help LSMs to better represent the impact of human activities like irrigation on the terrestrial water cycle?

To answer question (1) the activity focuses on the use of an innovative long-term record of satellite-based soil moisture for the development of a standardized agricultural drought index for a regional scale analysis. The novelty of this research is to establish the relation between drought indices and crop yields, through a comparison with a benchmark crop dataset, as well

as to analyze the additional information contained in satellite observations about agricultural productivity and water uses as compared to ground-based rainfall and modeled soil moisture. The main findings highlight the crucial role of soil moisture in limiting the crop productivity during drought periods and consequently its key contribution for agricultural drought analysis. Another important aspect highlighted in the results is that satellite estimates of soil moisture contain added information about both water scarcity conditions and anthropogenic impacts on water resources (i.e., irrigation), compared to soil moisture estimates based on model simulations (which do not account for human-related processes). Those outcomes strongly link the agricultural drought analysis with the second part of this research.

To answer question (2), the activity explicitly focuses on the quantification of the water used for agricultural purposes. Hydrological studies are converging on the synergistic use of models and satellite data to detect and quantify irrigation. The parameterization of irrigation in large-scale LSMs is improving but not sufficient by themselves to provide correct irrigation estimates, because they are still hampered by the lack of information about dynamic crop rotations, and by out-of-date maps of irrigated areas as well as unknown timing and amount of irrigation. On the other hand, satellite observations are directly affected by, and hence potentially able to detect, irrigation. Therefore, combining LSMs and satellite information through data assimilation (DA) can offer the optimal solution to quantify water used for irrigation at the desired spatio-temporal scale. This research aims at building an innovative and reliable DA system able to investigate the potential of high-resolution microwave EO data from the Sentinel-1 mission to improve irrigation quantification. The main assumption is that the joint update of soil moisture and vegetation model states, through the ingestion of 1-km radar backscatter, can improve irrigation estimation. This is a topic which was not investigated in previous literature. In this context, the optimization of a coupled system comprising a LSM and a backscatter observation operator, is firstly investigated. Results highlight the importance of equipping the LSM with an irrigation scheme to avoid strong biases between satellite observations and backscatter model predictions over intensively irrigated areas, where anthropogenic activities cannot be neglected. Secondly, backscatter observations are assimilated in the calibrated DA system, taking into account the effects of different backscatter polarizations. DA introduces both improvements and

degradations in soil moisture, vegetation and irrigation estimates. The spatial and temporal scale of the results have a large impact on the analysis and more contradicting results are found for an analysis at the plot scale, which highlights the need for very high-spatial resolution EO data and model parameterizations. Above all, this study sheds light on the limitations resulting from poorly-parameterized irrigation schemes included in LSMs which prevents large improvements in the irrigation simulation due to DA and points out on future implementations and input developments needed to improve LSM estimates of hydrological variables.

The research activities focus on regions characterized by a significant human pressure on the terrestrial water cycle. The first part includes the Karnataka and Maharashtra states, located in central India, whereas the second part includes irrigated areas with a different climate in Europe, i.e. Po Valley, in northern Italy, and Niedersachsen in Germany.

Sommario

Il fabbisogno idrico è in costante aumento e attualmente dominato dalle attività agricole finalizzate alla produzione di cibo a scala globale. Si prevede inoltre che l'aumento della popolazione globale in condizioni di cambiamento climatico aumenterà l'attuale prelievo di acqua mettendo in evidenza la necessità di sistemi di irrigazione più efficienti. Il forte impatto dell'irrigazione sul bilancio idrico globale è evidenziato anche da un generale esaurimento delle risorse idriche a larga scala, soprattutto per quel che riguarda le acque di falda. La riduzione delle risorse idriche è il risultato dell'effetto combinato dell'attività antropica e del cambiamento climatico. Tuttavia, la capacità di quantificare l'impatto umano, ed in particolare l'impatto delle pratiche agricole, sul ciclo idrologico è limitata dalla mancanza di dati osservati (principalmente dati di irrigazione) e dalla difficoltà che i modelli di superficie terrestre (LSM) hanno nel rappresentare pratiche antropiche. Queste limitazioni hanno un impatto significativo sulla sicurezza idrica e alimentare, minando la capacità di monitorare e prevedere eventi di siccità, così come la capacità di gestire in sicurezza la risorsa idrica.

Questa tesi mira a far luce sull'utilità di innovativi dati satellitari di rilevamento da remoto per caratterizzare la siccità agricola e per quantificare cambiamenti del ciclo idrologico indotti da attività antropiche, in particolare l'irrigazione, al fine di aiutare i modelli a migliorare la loro capacità di rappresentare più realisticamente il ciclo idrologico terrestre. Sulla base di ciò, l'attività di ricerca affronta due importanti tematiche:

1) Qual è il valore aggiunto di dati satellitari di ultima generazione (nello specifico l'umidità del suolo da satellite) nel monitoraggio della siccità e in che misura questi dati sono in grado di fornire informazioni potenziali sulla produttività delle colture rispetto ai dati ottenuti da LSM?

2) Dati satellitari ad alta risoluzione possono aiutare a rappresentare l'impatto delle attività umane sul ciclo idrologico terrestre nei LSM?

Per rispondere alla domanda (1) un innovativo dataset di umidità del suolo da satellite a lungo termine è stato selezionato per lo sviluppo di un indice standardizzato di siccità agricola da

utilizzare in un'analisi a scala regionale. L'aspetto innovativo di questa ricerca è quello di stabilire la relazione tra indici di siccità agricola e dati di raccolto, nonché di analizzare le informazioni aggiuntive contenute nelle osservazioni satellitari riguardo la produttività agricola e l'uso antropico di acqua, rispetto a dati in situ di precipitazione e all'umidità del suolo modellata. I risultati principali evidenziano il ruolo cruciale dell'umidità del suolo nel limitare la produttività delle colture durante i periodi siccitosi e di conseguenza il contributo chiave di questa variabile climatica per l'analisi della siccità agricola. Un altro aspetto importante che si evidenzia nei risultati è il grado di informazione contenuto nelle stime di umidità del suolo ottenute da dati satellitari, sia sulle condizioni di scarsità d'acqua che sull'impatto delle attività umane sul ciclo idrologico, rispetto alle stime di umidità del suolo modellato. Tali risultati collegano fortemente l'analisi della siccità agricola alla seconda parte di questa ricerca.

Per rispondere alla domanda (2) l'attività si è concentrata esplicitamente sulla quantificazione della risorsa idrica utilizzata a scopo agricolo. Negli ultimi anni, gli studi idrologici stanno convergendo sull'uso sinergico di modelli e dati satellitari per rilevare e quantificare l'irrigazione. La parametrizzazione dell'irrigazione nei LSM su larga scala è migliorata nell'ultimo decennio, ma non è ancora sufficiente a fornire stime corrette di irrigazione, in quanto ostacolata dalla mancanza di informazioni aggiornate sulla rotazione annuale delle colture, aree irrigue e dal fatto che tempi e quantità di irrigazione sono essenzialmente sconosciuti. D'altra parte, le osservazioni satellitari sono direttamente influenzate dall'irrigazione e quindi potenzialmente in grado di rilevarla. Pertanto, l'assimilazione di tali dati (DA) all'interno di modelli può offrire la soluzione ottimale per quantificare l'acqua utilizzata a scopo irriguo alla scala spazio-temporale desiderata. Questa ricerca mira dunque a costruire un sistema di DA innovativo in grado di studiare il potenziale delle osservazioni satellitari alle microonde ad alta risoluzione della missione Sentinel-1 per migliorare la quantificazione dell'irrigazione. L'ipotesi principale è che aggiornando congiuntamente gli stati di umidità del suolo e vegetazione di un LSM, attraverso assimilazione di dati radar di retrodiffusione (backscatter) alla risoluzione di 1 km, possa migliorare l'irrigazione. Tale aspetto non è stato precedentemente analizzato in letteratura. Nell'ambito di questa attività è stato quindi sviluppato un sistema che accoppia un LSM ed un operatore di osservazione (observation operator) per l'assimilazione di dati di backscatter. I risultati

evidenziano l'importanza di dotare il LSM anche di uno schema di irrigazione per ridurre significativamente il bias tra osservazioni satellitari e previsioni del modello su aree intensamente irrigate, dove le attività antropiche hanno un ruolo non trascurabile. Una volta calibrato il sistema, le osservazioni di backscatter sono state assimilate, tenendo conto dell'effetto delle diverse polarizzazioni del segnale osservato. L'assimilazione sembra introdurre sia miglioramenti che riduzione delle performance nelle stime di umidità del suolo, vegetazione ed irrigazione. È inoltre possibile osservare come la scala spaziale e temporale dell'analisi abbia un forte impatto sui risultati. In tal senso, l'attività fa luce su vantaggi e limitazioni derivanti dall'uso di schemi di irrigazione caratterizzati da una parametrizzazione semplice, mettendo in evidenza gli step futuri necessari per migliorare la stima di irrigazione e delle variabili idrologiche.

L' attività di ricerca è stata svolta su due regioni caratterizzate da una significativa pressione umana sul ciclo idrologico. Nella prima parte si fa riferimento agli stati di Karnataka e Maharashtra, situati nell'India centrale, mentre la seconda parte della ricerca è stata realizzata su aree irrigate in Europa, caratterizzate da condizioni climatiche differenti, ovvero, la Valle del Po, nell'Italia settentrionale, ed il sito di Niedersachsen in Germania.

Samenvatting

De vraag naar water blijft stijgen. Wereldwijd is het vooral de landbouw die grote hoeveelheden water vraagt om voedselproductie te garanderen. Bovendien dreigen de populatiegroei en klimaatveranderingen de waterbehoeften nog te versterken, waardoor efficiënte irrigatiesystemen steeds belangrijker worden. De globale waterverdeling staat onder druk van zowel menselijke activiteiten (e.g. irrigatie) als van toenemende extreme natuurverschijnselen (e.g. droogtes), met lokaal een vermindering van watervoorraden in bijvoorbeeld het grondwater. Onze kennis over de impact van menselijke activiteiten is echter beperkt door het gebrek aan data (e.g. irrigatie referentie data) en de gebrekkige weergave van menselijke processen zoals irrigatie in landoppervlakte modellen (LM). Dit gebrek aan inzicht vormt een bedreiging voor water en voedselveiligheid, omdat we zonder dit inzicht droogtes niet goed kunnen voorspellen en opvolgen, en watervoorraden niet goed kunnen beheren.

Deze thesis wil het nut van nieuwe aardobservatie (AO) data bestuderen voor het karakteriseren van droogtes en het detecteren van veranderingen in de watercyclus door menselijke activiteiten, zoals irrigatie. Deze data kunnen dan vervolgens numerieke modellen helpen om de watercyclus beter te simuleren. Dit onderzoek behandelt twee belangrijke onderzoeksvragen:

1) Wat is de toegevoegde waarde van recente AO data, i.e. satelliet-gebaseerd bodemvocht, voor het monitoren van droogtes, en wat is het potentieel van deze AO data vergeleken met LSM schattingen van bodemvocht voor gewas voorspellingen?
2) Kunnen hoge-resolutie AO data LMs helpen om menselijke activiteiten, zoals irrigatie, beter te schatten in de terrestrische watercyclus?

De eerste vraag (1) wordt in deze thesis beantwoord door lange-termijn satelliet data van bodemvocht te gebruiken voor de berekening van een gestandaardiseerde landbouwkundige droogte-index op een regionale schaal. Dit onderzoek verbindt droogte-indexen met gewasopbrengsten, via een vergelijking met veld data van gewassen. De resultaten tonen ook dat bodemvocht een limiterende factor is voor gewasproductie tijdens droogtes en dus effectief kan gebruikt worden in landbouwkundige droogte analyses. Daarnaast wordt aangetoond dat,

vergeleken met in situ neerslag data en gemodelleerd bodemvocht, satelliet data bijkomende informatie bevatten over landbouw productiviteit en watergebruik. Satelliet schattingen van bodemvocht bevatten meer informatie over zowel watertekorten als menselijke invloeden op watervoorraden (e.g. irrigatie) dan modelsimulaties van bodemvocht (die geen menselijke activiteiten bevatten). Dit maakt de brug naar het tweede deel van dit onderzoek.

De tweede vraag (2) gaat in op de begroting van het watergebruik voor landbouw toepassingen. Hydrologische studies convergeren naar het idee dat modellen en satellietdata in synergie moeten gebruikt worden om irrigatie te detecteren en de hoeveelheden irrigatiewater te schatten. De parameterizatie van grootschalige LMs is momenteel niet toereikend om irrigatie nauwkeurig te schatten, omdat er geen dekkende informatie is over gewasrotaties, omdat er geen goede kaarten zijn waarop geïrrigeerde land fracties zijn aangeduid, of omdat er te weinig veld data zijn om het ogenblik van de toepassing en de hoeveelheid aan irrigatie te kalibreren. Satelliet data zijn direct beïnvloed door irrigatie en zouden dus mogelijk irrigatie kunnen detecteren. Het combineren van LMs en AO data via data assimilatie (DA) kan een optimale oplossing bieden om het watergebruik voor irrigatie te schatten op de gewenste ruimtelijke en temporele schaal. In dit onderzoek is een innovatief DA systeem opgezet om het potentieel van hoge-resolutie microgolf data van de Sentinel-1 satelliet te gebruiken voor irrigatie schatting. De aanname is dat de gezamenlijke toestandupdate van bodemvocht en vegetatie de irrigatie schatting van verbeteren na de opname van 1-km observaties van radar terugkaatsing. Dit is niet eerder beschreven in de literatuur. Een eerste stap in de ontwikkeling van het DA systeem is de koppeling van het LM met een radar terugkaatsing observatiemodel (*observation operator*). Hierbij is het belangrijk dat een ruwe schatting van irrigatie door het LM wordt gesimuleerd om grote persistente verschillen in terugkaatsingen van de satelliet data en model voorspellingen te beperken over intens geïrrigeerde gebieden. In een tweede stap worden de radar observaties geassimileerd in het LM, dat uitgerust is met een ruwe irrigatie simulatiemodule en een gekalibreerd terugkaatsing observatiemodel. De assimilatie van terugkaatsingobservaties in verschillende polarisaties is bestudeerd, en zowel verbeteringen als degradaties van schattingen voor bodemvocht, vegetatie en irrigatie zijn bekomen. De ruimtelijke en temporele schaal van de resultaten heeft een grote invloed op de interpretatie van de resultaten. Op de veldschaal zijn de

resultaten het meest tegenstrijdig, wat een nood voor zeer hoge resolutie AO data en model parameters aangeeft. Deze studie toont bovenal aan dat er beperkingen zijn in de efficiëntie van het DA systeem door een gebrekkiger parameterizatie van de irrigatiemodule in LMs. De implementatie en input voor deze irrigatiemodules moet in de toekomst dus verbeteren.

Het onderzoek focust op twee gebieden met een belangrijke druk van menselijke activiteiten op de watercyclus. Het eerste deel van de thesis gaat over de Karnataka en Maharashtra staten in centraal India. Het tweede deel dekt geïrrigeerde gebieden met verschillende klimaten in Europa, i.e. de Po vallei in noord Italië en Niedersachsen in Duitsland.

Acknowledgements

An International Doctorate is the most exciting and powerful experience that a student can hope to realize in his/her life.

The first person that I wish to thank for this realized dream is my Supervisor Christian Massari. He is a great Scientist and brought me back to Scientific Research when I felt confused about my future. He followed me throughout the PhD with patience and always inspiring me. Thank you Christian for helping me find my way again.

Equally important, I would like to thank all my Supervisors.

Prof. Gabriëlle De Lannoy was a pillar. Her devotion to Research and Science is a lighthouse and without her expertise, experience and help I am sure that nothing would have been the same. Thank you, Gabriëlle, for being so kind and always available to help me. This meant a lot to me.

I would like to thank Prof. Renato Morbidelli for his valuable guidance and to be always supportive and helpful during this PhD. He believed in my capacities and his advices were fundamental to conclude the Doctorate.

Dr. Michel Bechtold had a crucial role for the success of this activity. We spent so many evenings working on the NASA LIS scripts to develop our DA system. Dear Michel, I am very grateful that I could get inspiration from you sharing this exciting experience.

Additionally, I would like to thank all the CNR-Irpi Hydrology group. Without them this experience would not have been possible, literally. I am so lucky to work in such an amazing and inspirational group of people. In the last years we shared joys, successes and difficult moments. They have become my second family. In particular I want to thank Paolo and Jacopo, colleagues but also great friends, who have always helped me when I needed it. A special thought goes also to the RSDA KU Leuven group. Such amazing people! I want to thank all of them for being so inspirational and to make me feel always at home in Leuven. We shared ideas but also dinners and coffees. I will never forget the abroad period in Leuven.

I wish to acknowledge all my family. My mother Anna is my light in the darkness, and she has always believed in me, in what I was, what I am and in what I can become. Thank you, Mamy, for always being there for me. My father Vittorio was always present in his own way and I know he is proud of me. Thank you, Dad, for being an inspiration of dedication to work and wisdom. My brother Alessandro is probably the most important person in my life. He is the person that I trust the most and he makes me confident that any goal is achievable with commitment and dedication. Thank you Hermano! My cousin Federico is my second brother and since I was young he always believed in me. A special thought goes to him too.

I want to thank those who are not here anymore, at my side, because all the people who cross our path influence our life, turning us into the special and unique beings we are. And last, but very important, I want to thank all my old and new friends for always being present. Life is not possible without friends and happiness is only real when it is shared.

Table of contents

List of figures

List of tables

List of main acronyms

- ASCAT: Advanced SCATterometers
- AVHRR: Advanced very high resolution radiometer
- CCI: Climate change initiative
- CGLS: Copernicus Global Land Service
- CR: Cross ratio
- DA: Data assimilation
- EO: Earth observations
- ESA: European space agency
- ESDAC: European soil data center
- ET: Actual evapotranspiration
- FC: Field capacity
- GRIPC: Global rainfed irrigated and paddy croplands
- GVF: Greenness vegetation fraction
- HWSD: Harmonized Soil World Database
- IMD: Indian meteorological Institute
- KGE: Kling-Gupta efficiency
- LAI: Leaf area index
- LDT: Land data toolkit
- LC: Land cover
- LIS: Land information system
- LSM: Land Surface model
- MA: Soil moisture availability referred to root zone
- MW: Microwave
- MERRA-2: Modern-Era Retrospective analysis for Research and Applications 2
- MODIS: Moderate Resolution Imaging Spectroradiometer Moderate Resolution Imaging Spectroradiometer
- NDVI: Normal difference vegetation index
- OL: Open Loop
- PGR SM: Proximal gamma ray soil moisture
- PSO: Particle swarm optimization
- RMSE: Root mean square error
- RS: Remote sensing
- RZ: Root zone
- RZSM: Root zone soil moisture

- SAR: Synthetic aperture radar
- SMAP: Soil moisture active passive
- SMOS: Soil moisture active passive
- SPI: Standardized precipitation index
- SRTM: Shuttle radar topography mission
- SSE: Sum of square errors
- SSI: Standardized soil moisture index
- SSM: Surface soil moisture
- Tb: Brightness temperature
- UMD: University of Maryland
- UN-LCCS: United nations land cover classification system
- WCM: Water cloud model
- WP: Wilting point

Chapter 1: Introduction

The large influence of anthropogenic activities on the terrestrial water cycle have led scientists to identify a new geological era which has been called Anthropocene (Montanari et al., 2013; Savenije et al., 2013; Steffen et al., 2011). Indeed, human water needs have been increasing in recent years and the long-term decrease in water availability due to climate change together with the impact of anthropogenic processes is leading to hydrological cycle modifications with consequent impacts on human well-being. Water resources availability is indeed affected both by natural disasters, such as drought events which are increasing in severity (Mishra and Singh, 2010), and by human water needs for food production worldwide (Wada et al., 2017). In particular, the strong impact of irrigation on the global water budget is evidenced by many studies and it has been estimated that about 70% of the global freshwater withdrawals are used for irrigating crops (Foley et al., 2011; Siebert et al., 2015). Land surface models (LSM) are able to simulate the water cycle but simulations are affected by limitations as they miss or poorly-simulate human activities. Conversely, the new era of earth observations (EO) allows to observe the Earth surface (and sub-surface) processes in a more realistic way providing useful information on both natural risks (i.e., drought events) and anthropogenic activities (i.e., irrigation).

This PhD dissertation investigates how innovative EO can be used to: 1) characterize agricultural drought; and 2) help models taking into account human impacts and improving their ability to better estimate components of the terrestrial water cycle.

Section 1.1 covers the first point and describes the influence of natural disasters, and more specifically agricultural drought events, in the water cycle framework. A review of previous studies on drought characterization is provided and particular attention is given to future directions that drought analysis should take to understand additional information that EO can bring on water scarcity, crop productivity and human impacts on the water resources as compared to ground-truth or modeled data.

Section 1.2 explicitly focuses on human impacts on the terrestrial water cycle, analyzing previous studies on irrigation quantification through the use of models and satellite-based EO observations as well as methods to combine both information via data assimilation (DA). Limitations of

previous studies are highlighted as well as challenges for future DA analysis. Finally, Section 1.3 discusses objectives and structure of this thesis.

1.1 Hydrological water cycle and drought

1.1.1 Hydrological natural hazards: drought events

The natural hydrological cycle is represented by the endless movement of water from one Earth system reservoir to another, with the water status changes regulated by solar energy. The main geophysical processes that regulate water exchanges near the land surface are represented by precipitation, evapotranspiration, infiltration and runoff which connect the hydrological major water storages, such as the soil water content, rivers, lakes, oceans, glaciers, with the atmosphere.

Extreme anomalies in components of the hydrological cycle are often associated with different natural hazards; one of the more complex is represented by drought, an extreme event originating from a period of low precipitation (McKee et al., 1993). The scientific community generally recognizes three types of drought occurring at different timescales: meteorological, agricultural and hydrological. A meteorological drought starts with a deficit in precipitation and can evolve in an agricultural drought, proceeding in a period of declining soil moisture and consequent crop failure (Mishra and Singh, 2010). An additional evolution in time of precipitation deficit can lead to a hydrological drought, represented by an abnormally low streamflow in rivers and abnormally low levels in lakes, reservoirs, and groundwater (Van Loon, 2015). The evolution in time of drought events implies indeed an involvement of various environmental systems (Vicente-Serrano et al., 2020).

Agricultural droughts, in particular, assume key importance from a societal point of view, with crop-yield reductions, economic losses and famine episodes. Since the 1960s, drought events have been one of the main drivers of crop failure worldwide (Cottrell et al., 2019) and with the world's increasing population to 9.1 billion by 2050 foreseen by the Food and Agriculture Organization (FAO, 2009), understanding the impact of drought events on food production has a crucial importance for countries relying on both rain-fed and irrigated agricultural production such as for instance India, or the Mediterranean region (Tramblay et al., 2020).

1.1.2 Agricultural drought indices

Since the 1990s, many drought indices have been developed, using different indicators to characterize and quantify different types of drought (Zargar et al., 2011). Among indicators most commonly used by the scientific community is the Standardized Precipitation Index (SPI, McKee et al., 1993). Developed using long-term rainfall records, this statistics-based index is recommended as a key drought indicator for global applications in the Lincoln Declaration on Drought Indices (Hayes et al., 2011). SPI's ability to detect the rapid development of rainfall deficit makes it particularly appropriate for monitoring meteorological drought (Farahmand and AghaKouchak, 2015) but it can also be used to monitor agricultural drought conditions. Zargar et al. (2011) suggest that applying a three-month timescale to SPI can provide a seasonal estimation of rainfall, reflecting short- and medium-term soil moisture conditions. The advancements of rainfall-based indices have been supported by long-term datasets of rainfall measurements obtained through rain-gauge networks, such as the Global Precipitation Climatology Center (GPCC; Schneider et al., 2014)..

Although rainfall-based drought indices are popular, a more appropriate indicator of agricultural drought is soil moisture, as it controls the amount of water available to support evapotranspiration and, in turn, plant growth (Velpuri et al., 2016). In agriculture, crop failure occurs when there is not enough moisture to support production. However, using conventional "in situ" soil moisture measurements for monitoring drought at large scale is practically impossible. This is due to their point-based nature and limited spatial coverage (Peled et al., 2010), as well as there being wide variability in soil moisture levels across a given area of study (Brocca et al., 2012).

To overcome this issue, some authors have proposed using satellite-based soil moisture measurements (Carrão et al., 2016; Martínez-Fernández et al., 2016) or land surface model outputs (i.e. Farahmand and AghaKouchak, 2015; Dutra et al., 2008; Sheffield et al., 2004). Despite inherent uncertainties (such as issues related to satellite retrievals in the first case, and modeling error and simplified or absent representation of anthropogenic activities in the second) both types of

products guarantee good coverage of the Earth's surface, and thus are well suited for building a spatially consistent representation of drought conditions.

1.1.3 Satellite soil moisture for agricultural drought

The use of satellite-based measurements of soil moisture for monitoring agricultural drought has, in particular, expanded of late thanks to the increased availability of RS-based products derived from active and passive microwave (MW) sensors (Carrão et al., 2016; Mishra et al., 2017; Rahmani et al., 2016; Velpuri et al., 2016; Zhu et al., 2019). The main advantage of satellite-based soil moisture observations over modeled data is their ability to observe the "true" state of soil wetness over the Earth's surface (i.e., "true" as in potentially also taking into account human-related processes such as irrigation; Lawston et al., 2017). Despite this advantage, there are limitations to use satellite soil moisture observations, such as the relatively short data record (which hampers calculation of standardized soil moisture drought indices; Sheffield et al., 2004; Martínez-Fernández et al., 2016), the shallow soil penetration depth (i.e., less than 5 cm; Collow et al., 2012; Kerr, 2007), and errors related to the retrieval algorithm or instrument radiometric inaccuracies, which could partly mask anomalous events (Dorigo et al., 2010; Su et al., 2016; Bauer-Marshallinger et al., 2018).

The interest in retrieving soil moisture data from EO began at the end of 1970s, but the first dedicated soil moisture program – the European Space Agency (ESA) Soil Moisture and Ocean Salinity (SMOS) mission – was launched only in 2009 (Kerr et al., 2010). However, thanks to the work initiated by (Liu et al., 2012), it is now possible to access a long-term (from 1978), consistent soil moisture time series based on multiple products derived from historical active and passive MW EO data. The ESA Climate Change Initiative (CCI) soil moisture product (Dorigo et al., 2017) has such a long coverage, which makes it well suited for implementing soil moisture-based drought indices, such as the Standardized Soil Moisture Index (SSI, Farahmand and AghaKouchak, 2015), the Empirical Standardized Soil Moisture Index (ESSMI, Carrão et al., 2016), the Soil Moisture Deficit Index (SMDI, Narasimhan and Srinivasan, 2005) and the Soil Water Deficit Index (SWDI, Martínez-Fernández et al., 2015). More details about soil moisture drought indicators will be provided in Section 2.1.5.

1.1.4 Agricultural drought indices and crop production

Although widely applied, there is no clear evidence that such soil moisture indices (including those derived from model estimates) can flag-up below-normal soil moisture conditions likely to limit crop production, thus forecasting when famine might occur. In this respect, only a few studies have tried to relate drought indices with crop-yield data (i.e. Carrão et al., 2016; Gibon et al., 2018; Narasimhan and Srinivasan, 2005; Zhang et al., 2017). Moreover, in these studies the authors were more interested in using crop-yield data as an indirect validation tool, or for comparing the validity of different indices built with different variables (i.e., rainfall, soil moisture, Normalized Difference Vegetation Index (NDVI), evapotranspiration). These studies were undertaken without considering either the source of soil moisture data (i.e., satellite observations or model) used to calculate the indices or the ability of these indices to provide information on future crop yields as a function of the drought severity. In this context, particular importance is assumed by the additional information that satellite soil moisture dataset can provide on agricultural crop production and on human-related water uses, such as irrigation, as compared to land surface model (LSM) soil moisture estimates. This is a key research topic considering that human activities can mitigate the impact of droughts on crop production, through an optimized use of water resources (Tramblay et al., 2020), or exacerbate water scarcity (IPCC, 2021). Studies to understand the effects of human activities on the water cycle are of critical importance for an optimal water management and EO data play a central role in providing useful information at large (global) as well as at small (plot) scale.

1.2 Human impacts on the water cycle: irrigation quantification

1.2.1 Irrigation in the water cycle

Humans represent the largest driver of environmental change worldwide, and therefore the current geological epoch has been named Anthropocene (Crutzen, 2002; Falkenmark et al., 2019; Steffen et al., 2015). With the increasing population and urbanization, human needs are also increasing, producing human pressure on the hydrological cycle at different spatial scales (Falkenmark et al., 2019). A consequent decrease in water availability for ecosystem use can lead to ecosystem degradation and hydrological cycle modifications with resulting impacts on overall

water scarcity, human well-being and many ecosystems worldwide (Abbott et al., 2019; Falkenmark, 2003). Thus, it is undeniable that nowadays the interaction between human activities and the hydrological cycle is stronger than ever (Montanari et al., 2013). However, this interaction is still not well represented in water cycle diagrams. For instance, Abbott et al. (2019) analyzed 114 English-language diagrams of the water cycle from textbooks, peer-reviewed articles, government materials and online sources, surprisingly finding that 85% of the diagrams were widely biased, showing no interaction between humans and the water cycle. Those sources of uncertainties and inaccuracies should be reduced to allow an optimal water management from both policymakers and public perspectives.

In this context, several studies have analyzed the water resources differentiating them based on the different human uses. Three main categories were identified: 1) the blue water is the freshwater available for withdrawal in rivers, lakes or shallow aquifers; 2) the green water is the freshwater represented by the precipitation water stored in unsaturated soil and later used for evapotranspiration and mainly for agricultural (i.e., irrigation) or livestock purposes; and finally, 3) gray water, the freshwater used to assimilate waste (Falkenmark, 2003; Falkenmark and Rockström, 2006; Hoekstra, 2011; Postel et al., 1996). Additionally, humans have interfered in the terrestrial water cycle also altering the Earth's land surface through deforestation and converting land uses to agricultural, urban and industrial landscapes (Abbott et al., 2019). Correctly quantifying the different sources of water, the human uses (i.e., water abstractions and applications) and its effect on the terrestrial water cycle is one of the main challenges for the hydrological community.

In recent years, several studies have focused on the quantification of green and blue water resources using LSMs, but a conspicuous source of uncertainties seems to be related to poorly-modeled or unmodeled human processes, such as water abstractions, irrigation and water management (Ozdogan et al., 2010a). Particularly, irrigation represents one of the most impactful human interventions, and consequently disturbance, in the terrestrial water cycle. Foley et al. (2011) reports that irrigated lands are only 17% of global croplands although they produce 40% of the world's food. Those percentages are expected to increase in the next decades due to

population growth and dietary shifts as highlighted by Ozdogan et al. (2010b) and in Matthews and Germain (2007), pointing to an increasing need in quantifying irrigation on a regional to global scale.

Correctly estimating irrigation in LSMs can serve two main purposes. On the one hand, it can help improving the water management (Bretreger et al., 2020; Le Page et al., 2020), on the other hand, it allows to quantitatively assess its effects on the terrestrial water, carbon and energy cycles (Breña-Naranjo et al., 2014; Haddeland et al., 2014; Hu et al., 2016; Qian et al., 2020). In this context, results of large-scale irrigation studies using LSMs have demonstrated that irrigation increases soil moisture and evapotranspiration (ET), and consequently latent heat flux with a decrease in sensible heat flux (i.e., Badger and Dirmeyer, 2015; Lawston et al., 2015; Ozdogan et al., 2010a).

1.2.2 Irrigation in models

Despite the significant impact of irrigation on the water and energy cycles, its simulation within LSMs is not yet common practice (Girotto et al., 2017). In earlier studies, attempts to simulate irrigation in LSMs have relied on different parameterizations of well-known irrigation systems (like sprinkler, flood, and drip systems; Evans and Zaitchik, 2008; Ozdogan et al., 2010a), making simplifying assumptions. For instance, in Ozdogan et al. (2010a) irrigation water is not withdrawn from a source (such as a river) but instead added as fictitious rainfall. In contrast, Nie et al. (2018) accounted for source water partitioning, albeit only partially, by considering groundwater irrigation. Irrigation is normally applied when soil moisture drops below a user-defined threshold (Ozdogan et al., 2010a), typically dependent on the soil properties obtained via soil texture maps.

Moreover, LSMs equipped with irrigation schemes need to be provided with auxiliary information about crop types and whether or not the crops are irrigated. This is because different crop types are characterized by different rooting depths, which means they require more or less water to restore root zone field capacity (FC). This information is normally gathered from static maps derived from statistical analysis and/or EO (Monfreda et al., 2008; Ozdogan et al., 2010a; Salmon et al., 2015) collected during specific historical periods which are normally different to the desired period of analysis. It is thus clear that the modeling of irrigation is subject to many

simplifying assumptions, which span from neglecting the year-to-year crop variability and the irrigation system used to the definition of irrigation application times based on water availability and crop conditions rather than actual farmer decisions.

1.2.3 Irrigation in observations from space

RS technologies are potentially able to monitor irrigated lands worldwide (Ambika et al., 2016; Bazzi et al., 2019; Bousbih et al., 2018; Dari et al., 2020; Gao et al., 2018; Le Page et al., 2020). In the last decade, some authors used visible and near infrared EO jointly with in situ data collected from inventories to map areas equipped for irrigation (Ambika et al., 2016; Ozdogan and Gutman, 2008). Kumar et al. (2015) were the first to propose the use of coarse resolution satellite MW sensors to detect irrigation. The authors compared different coarse-scale active and passive MW surface soil moisture (SSM) retrievals with SSM simulations from the Noah LSM (Ek et al., 2003) without activating an irrigation scheme over a continental US domain. Areas where the distributions of model and EO data sets deviated (based on a Kolmogorov-Smirnov test) were assumed to be irrigated. Even though some of the products showed a potential ability to detect irrigation, the authors concluded that the spatial mismatch between the satellite footprint and the irrigated fields, radio-frequency interference (RFI), vegetation, and topography could all deteriorate the accuracy of the results. Similar conclusions were found over the same area by Zaussinger et al. (2019) who compared coarse-scale satellite SSM products with soil moisture predictions from the Modern-Era Retrospective analysis for Research and Applications 2 (MERRA-2; Gelaro et al., 2017) in the absence of precipitation, and Escorihuela and Quintana-Seguí (2016) who additionally compared a downscaled version of SMOS SSM to SURFEX LSM simulations. Brocca et al. (2018), Jalilvand et al. (2019) and Dari et al. (2020) used a conceptually different approach with the same coarse scale MW SSM products and estimated irrigation by directly inverting a simple water balance equation (Brocca et al., 2014).

The Copernicus Sentinel-1 satellites (Sentinel-1A and Sentinel-1B) offer a new perspective for agricultural applications, thanks to the finer spatial resolution (up to 10-20 m) of the Synthetic Aperture Radar (SAR) backscatter data. For instance, Gao et al. (2018) proposed an approach to map irrigated lands over the Urgell region in Catalonia (Spain), and Le Page et al. (2020) proposed

a methodology to detect irrigation timing in south-west France comparing the SSM signal at the plot scale, derived using Sentinel-1 backscatter and NDVI from Sentinel-2 (El Hajj et al., 2016), with a water budget model forced by Sentinel-2 optical data for the detection of irrigation timing.

1.2.4 Towards irrigation estimation via data assimilation

Despite the high potential demonstrated by EO in detecting, mapping and quantifying irrigation, the uncertainties of the satellite retrievals, the relatively low revisit time of high-resolution active MW products and the too coarse spatial resolution of passive MW products with respect to the mean size of irrigated fields represent main limitations for irrigation information retrieval (Le Page et al., 2020; Romaguera et al., 2014).

Data assimilation (DA) is the most viable way to integrate model estimates (which resolve processes at the desired spatio temporal scales) and EO (which can track human processes and their interaction with the water and energy cycle), and it has been recognized as one of the effective methods to improve hydrologic predictions (Liu et al., 2012; Abbaszadeh et al., 2018). Several studies have explored applications of DA in hydrology, ranging from characterization of soil moisture and/or surface energy balance (i.e., Houser et al.,1998; Dunne et al., 2005) to rainfall-runoff modeling (Vrugt et al., 2005; Chen et al., 2014; Azimi et al., 2019; De Santis et al., 2021 to cite a few). Providing superior hydrologic state estimates, DA can consequently help in optimizing real world applications such as agricultural production and water management (Houser et al., 2012)

In land surface modeling as well, DA is used to reduce predictions' uncertainties. Contrasting LSM simulations with EO offers an opportunity to correct for unmodeled processes or missed events, such as irrigation (Girotto et al., 2017; S. V. Kumar et al., 2015). More generally, DA of satellite-based observations has shown the potential to update soil moisture (De Lannoy and Reichle, 2016a; Kolassa et al., 2017) and vegetation (Albergel et al., 2018; Kumar et al., 2019, 2020) and important impacts have been reported over agricultural areas (Kumar et al., 2020). Furthermore, the assimilation of total water storage (TWS) from the Gravity Recovery and Climate Experiment (GRACE) mission in LSMs has proven to provide important implication in understanding the human impacts on the water cycle (Girotto et al., 2017; Nie et al., 2019) but the

coarse resolution of this product (~1°) limits its direct usefulness for agricultural applications at the district or field level.

The assimilation of MW EO in LSMs often involves retrieval assimilation. However, assimilating retrievals (i.e., SSM or vegetation optical depth rather than MW brightness temperature or backscatter measurements) can be problematic as the retrievals may have been produced with ancillary data that are inconsistent with those used in the LSM (De Lannoy and Reichle, 2016b). This is particularly true for passive MW retrievals while active MW retrievals generally rely on change detection methods that lack land-specific ancillary information altogether. An alternative approach is to directly assimilate MW observations and equip the LSM with an observation operator that links land surface variables of interest (e.g., soil moisture and vegetation) with EO data. This allows to obtain consistent parameters and to reduce the chance of cross-correlated errors between model states and corresponding geophysical satellite retrievals. The direct assimilation of MW observations has already been demonstrated successfully for the update of soil moisture by using Tb derived from the SMOS and the Soil Moisture Active Passive (SMAP) missions (Carrera et al., 2019; De Lannoy and Reichle, 2016b; Reichle et al., 2019), as well as using radar backscatter from the Advanced SCATterometer (ASCAT) (Lievens et al., 2017a), and backscatter from Sentinel-1 in synergy with SMAP Tb (Lievens et al., 2017b). However, to our knowledge, none of these studies considered the joint updating of soil moisture and vegetation, and none specifically focused on the performance over irrigated areas. The backscatter from Sentinel-1 contains information on both soil moisture (Bauer-Marschallinger et al., 2018; Li and Wang, 2018; Liu and Shi, 2016; Zribi et al., 2011) and vegetation (Vreugdenhil et al., 2020, 2018) and assimilating this data in a land DA system could allow to correct for missed irrigation events.

1.3 Objectives and structure of the thesis

1.3.1 Objectives

The main objective of this research is to exploit innovative remotely-sensed data and test their ability to provide useful information on drought anomalies and on the impacts of agricultural human activities on the water cycle, with particular attention on developing methods to address

how much water is actually used for agricultural practices such as irrigation. This work can be divided into two main parts.

The first part (Chapter 2), aims at exploiting how the information contained in satellite EO can be used for monitoring agricultural drought events and crop yield production. **In this context, three aspects are addressed: 1) is SSM (~5 cm depth) appropriate for assessing agricultural drought? 2) What is the added value of using soil moisture data, as opposed to rainfall-based drought indices, for monitoring agricultural drought events? 3) What information do satellite SSM yield on crop production and on human activities over irrigated crops in comparison to LSM estimates, especially during drought conditions?**

The second part (Chapter 3 & 4) of this thesis, aims at developing a DA system able to merge LSM estimates and information contained in satellite observations for the quantification of the water used for agricultural practices (i.e., irrigation). The main target is to assimilate 1-km Sentinel-1 radar backscatter observation for a joint update of soil moisture and vegetation in order to inform the model about actual irrigation application and improve irrigation estimates, as well as land surface variables. **The assimilation is realized by coupling a LSM with a backscatter observation operator which maps land surface state variables to backscatter predictions (forecast). The main aspects analyzed in this part of activity are: 1) What is the optimal procedure to calibrate the backscatter observation operator and, can activating an -even poor- parameterized irrigation scheme into the LSM provide the optimal calibration over irrigated areas? 2) Can the sequential assimilation of Sentinel-1 backscatter to update soil moisture and vegetation improve LSMs irrigation simulations and what is the influence of different backscatter polarizations? 3) Which are the main limitations of the analysis (i.e., temporal and spatial scale, DA consistency and LSM parameterization)?**

1.3.2 Thesis structure

Based on the objectives, the structure of the thesis is as follows. **Chapter 2** describes the agricultural drought analysis of Modanesi et al. (2020), which was conducted over a large study area in India, particularly prone to severe droughts in recent decades. Such events increased in severity, frequency and areal extent between 1961 and 2015 (Mishra et al., 2018). For example,

between 2002 and 2012 India was affected by major droughts in 2002, 2009 and 2012 (D Udmale et al., 2014). These and past events have caused many problems for the population, whose livelihoods largely depend on agriculture. In this analysis, the link between crop production and drought severity predicted by three different standardized drought indices is investigated. These indices were obtained using: 1) satellite-based SSM from the ESA CCI soil moisture product, version 201706.0 (https://climate.copernicus.eu/) which provides a long-term data record (from 1978 to date) feasible for statistical drought analysis; 2) NASA's model-based soil moisture estimates from MERRA-2. Even though previous studies stated that this reanalysis product is affected by limitations (i.e., bias in precipitation over Asia; Yoon et al., 2019) its potential for drought characterization was assessed in recent studies (Le et al, 2020; Chen et al., 2018); and 3) ground-based rainfall data provided by the Indian Meteorological Department. Focusing on the states of Karnataka and Maharashtra, two crop types were considered: maize cultivated during the monsoon season (rainfed), and wheat produced in the dry winter season (usually irrigated). Potentials and limitations of satellite data and models to provide information on agricultural practices (i.e., irrigation) have driven the second part of this dissertation, where the main assumption is that ingesting EO into a LSM can improve the water cycle description and the detection/quantification of irrigation over intensively irrigated areas.

Chapter 3 focuses on coupling a LSM and a backscatter observation operator, based on Modanesi et al. (2021), in preparation for subsequent backscatter DA. Different backscatter models have been proposed to simulate the backscattering contributions of soil and vegetation (Attema and Ulaby, 1978; Baghdadi et al., 2017; Bai and He, 2015; Oh, 2004; Zribi et al., 2005). Most commonly used, the Water Cloud Model (WCM; Attema and Ulaby, 1978) represents the vegetation canopy as a homogeneous cloud containing randomly distributed water droplets. In order to use the WCM as forward operator in a backscatter DA system, it first needs to be calibrated to account for biases between the LSM simulations and satellite observations. However, calibrating a WCM over irrigated areas represents a key research problem if the same satellite backscatter signal is used for calibration and later for DA. Equipping the LSM with an irrigation module that makes the WCM less constrained by inconsistencies between simulated and observed backscatter during irrigation periods is the calibration strategy that was investigated in this activity. The analysis

was carried out over the Po Valley, one of the more intensively irrigated areas in Europe (water withdrawal in the Po basin is estimated to be 20.5 billion m^3/year, of which 16.5 billion m^3/year is withdrawn for irrigation; Po River Watershed Authority, 2016). We used the Noah-MP LSM (Noah-MP hereafter) as part of the NASA Land Information System (LIS) framework (Kumar et al., 2008) together with the WCM for the simulation of both backscatter vertical send and receive (VV) and vertical send and horizontal receive (VH) polarization. Level-1 Sentinel-1 backscatter is used to calibrate the WCM at 1-km resolution, using simulated SSM and Leaf Area Index (LAI) estimates from Noah-MP. The WCM is calibrated for a total of four calibration experiments for each polarization: 1) with or without activating an irrigation scheme within Noah-MP; and, 2) testing two different cost functions.

Finally, **Chapter 4** focuses on the DA of Sentinel-1 backscatter, using Noah-MP, equipped with the sprinkler irrigation scheme and a calibrated WCM in the NASA LIS framework, based on Modanesi et al. (2022, submitted). The ensemble Kalman Filter (EnKF; Evensen 1994) algorithm is selected to perform the DA analysis. The EnKF is optimally used for non-linear dynamics and it is popular in hydrological and land surface modeling studies (Reichle et al. 2002; De Lannoy and Reichle, 2016a, Kumar et al. 2019, 2020; De Santis et al., 2020 to cite a few works). It uses an ensemble of model trajectories to represent the background error covariance at each time of an update. The main assumption in the performed DA analysis is that when coupling the Noah-MP DA system with a simple parameterized sprinkler irrigation module, irrigation water amounts can be optimally estimated when optimal soil moisture and vegetation estimates are available from DA. Additionally, the direct assimilation of Level-1 observations through a backscatter observation operator (here the WCM) allows to avoid bias correction between model states and the RS product before DA, as the bias is previously compensated through the WCM calibration (Chapter 3). This approach reduces the chance of cross-correlated errors between model states and satellite retrievals, as required by classical Bayesian-based filters (the reader can refer to section 1.2.4 for more details). The analysis is carried out over two irrigated pilot sites, the first one sited in the Po Valley and a second one located in northern Germany. Two DA experiments are realized over the two pilot sites, i.e. using Sentinel-1 backscatter in either VV or VH polarization, to update both soil moisture and vegetation. The DA experiments were compared

with the reference Open Loop (OL) run, i.e. a model-only simulation which does not assimilate any satellite data. The main conclusions are drawn in **Chapter 5** together with future perspectives and outlooks of this research.

Chapter 2: Remote sensing for monitoring agricultural drought

This chapter describes the analysis and results published in the following journal article:

Modanesi, S., Massari, C., Camici, S., Brocca, L., G. Amarnath. ***Do satellite surface soil moisture observations better retain information about crop-yield variability in drought conditions?*** *Water Resour. Res., 56, (2), Article e2019WR025855, https://doi.org/10.1029/2019WR025855, 2020.*

The analysis provides insights on information obtained from satellite surface soil moisture (SSM) observations (as compared to modeled soil moisture and observed ground precipitation) on water stress and its impact on crop production variability in India. In particular, this activity aims at showing to what extent satellite soil moisture may help to improve the efficiency of agricultural and irrigation management practices. The analysis involved generating a Standardized Soil Moisture Index (SSI) using 1) satellite soil moisture observations from the European Space Agency (ESA) Climate Change Initiative (CCI); and 2) the Modern-Era Retrospective Analysis for Research and Applications, version 2 (MERRA-2) soil moisture dataset; as well as producing a Standardized Precipitation Index (SPI) using ground-based rainfall observations from the Indian Meteorological Department (IMD). Spanning the period from 1998 to 2015, the study covers Maharashtra and Karnataka states. These states were recently hit by a severe drought, resulting in significant crop failure and human losses. Chapter 2 is organized as follows: i) Section 2.1 describes data and methodologies used; ii) Section 2.2 presents results and discussion and finally iii) conclusions are drawn in Section 2.3.

2.1 Data and methodology

2.1.1 Study area

The analysis was carried out in the states of Maharashtra and Karnataka in India (Figure 2.1), the economies of which are mainly based on agriculture. Located on the Deccan Plateau, a large plain covering part of western and southern India, the study area is bordered to either side by the Western and Eastern Ghats chains and by the Satpura Range in the north. Maharashtra is India's

third-largest state, with a total of 34 districts and a surface area of 307,713 km^2. It experienced droughts in 2012 (D Udmale et al., 2014) and 2015 (Mishra et al., 2016). Karnataka, lying south of Maharashtra, covers 191,976 km^2 and encompasses 27 districts. It experienced severe consecutive droughts in 2001-02, 2002-03, 2003-04, 2009 and 2012 (Jayasree and Venkatesh, 2015).

The major part of India has a tropical monsoon climate that supports rainforests, with the rest defined as semi-arid tropics (in accordance with Koppen-Geiger climate types; Peel et al., 2007). The climate is dominated by the summer monsoon, with the year divided into two main seasons: (1) winter or rabi season, from October to March; and (2) summer monsoon or kharif season, between June and September.

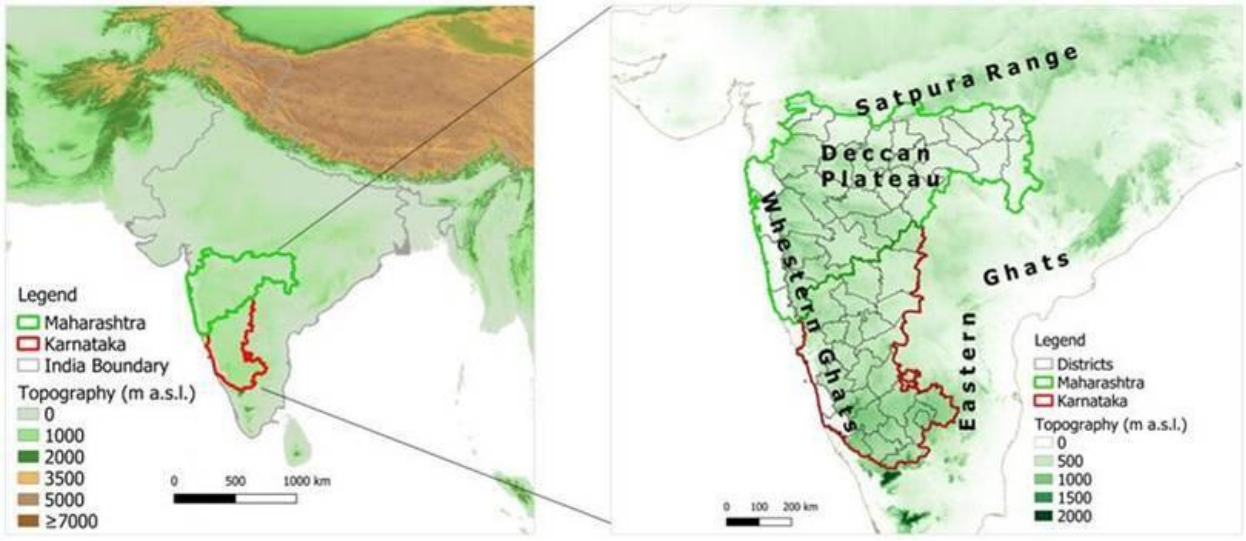

Figure 2.1. Topographic maps showing the states of Maharashtra (green boundary) and Karnataka (red boundary), which are divided into 34 and 27 districts respectively. Topographic data from ETOPO1 1 Arc-Minute Global Relief Model (Amante and Eakins, 2009)

The study area spans two agro-climatic zones. The Western Plateau and Hills zone includes the Deccan Plateau within northern Maharashtra. Here, the July temperature varies between 24°C and 41°C, while in January it ranges from 6°C to 23°C. Major crops cultivated in rainfed areas are wheat, gram, millets, cotton, pulses, groundnut and oilseeds, while wheat, sugarcane and rice are produced in irrigated areas (Ahmad et al., 2017). Maharashtra contributes 9.1% of India's total maize production (https://farmer.gov.in/M_cropstaticsmaize.aspx). The Southern Plateau and Hills agro-climatic zone comprises southern Maharashtra and the greater part of Karnataka. Here the mean July temperature ranges between 25°C and 40°C, while in January it varies between

10°C and 20°C. It is a dry zone, where millets, oilseeds and pulses are major crops (Ahmad et al., 2017). Karnataka contributes 16.5% of India's total maize production (https://farmer.gov.in/M_cropstaticsmaize.aspx) and, together with Maharashtra, it is one of six major areas of wheat cultivation (https://farmer.gov.in/M_cropstaticswheat.aspx).

2.1.2 Crop yield data

A dataset of annual yields (tonnes/ha) for the districts of Maharashtra and Karnataka was provided by the International Water Management Institute (IWMI) of Sri Lanka (Source: SDDS-DES, Ministry of Agriculture, Govt. of India & Ministry of Communications & IT, Govt. of India). These data are available at: https://data.gov.in/resources/district-wise-season-wise-crop-production-statistics-1997.

The analysis was carried out separately for the summer and winter growing seasons. Maize was assessed for the summer (kharif) growing season, corresponding with the southwest monsoon, as more than three-quarters of India's maize is produced in this season (http://ficci.in/spdocument/22966/India-Maize-Summit.pdf) mostly under rainfed conditions (http://ficci.in/spdocument/20386/India-Maize-2014_v2.pdf). Kharif maize is generally sown 12-15 days before the onset of monsoon (i.e., last week of June to first fortnight July; https://farmer.gov.in/imagedefault/pestanddiseasescrops/normalmaizeproductiontechnologies.pdf)

For the winter (rabi) season, wheat was selected, which in India is usually planted in October and harvested in April (Zhang et al., 2017). As one of the country's main dry-season crops, it is cultivated predominantly in irrigated areas (Krishna Kumar et al., 2004). With specific information about irrigated wheat fields not available, wheat harvests were assumed as entirely irrigated as an additional hypothesis. We realize that recognizing wheat as an irrigated crop might be not completely accurate. However, there is a high chance that wheat crops are irrigated during winter, as rainfall is very low at this time and irrigation is generally the only way to achieve successful production. Annual yields for maize and wheat were obtained for each district for the period 1998–2015; this is therefore the study period of our analysis.

2.1.3 Soil moisture and rainfall data

Different datasets were used in this study to estimate drought indices. Specifically, the satellite-based ESA CCI soil moisture product, and the modeled product MERRA-2 were used to estimate the SSI index. Ground-based rainfall observations were used for the SPI computation. A brief description of the main characteristics of each dataset is provided below.

- The ESA CCI product is a complete soil moisture dataset spanning 40 years from 1978. It is derived from data observed by active and passive microwave sensors (http://www.esa-soilmoisture-cci.org/). In this study, we used the version 201706.0 at 0.25°/dekadal (10-day) spatial/temporal resolution, which was created by merging the active and passive products (available at https://climate.copernicus.eu/). Using a combined product such as this increases the likelihood of having at least one observation for a given day and pixel, thereby reducing the number of data gaps. Furthermore, merged products generally perform better than single-sensor products (Dorigo et al., 2017). The dekadal product was selected, as daily satellite observations are not needed when computing a standardized drought index at a monthly time scale. It should be noted that CCI soil moisture data are characterized by irregular temporal coverage prior to 2002. However, as the analysis was carried out on a monthly time scale and spatially averaged at district-level (ensuring that multiple overpasses were considered temporally and spatially) this issue should have a limited impact. Moreover, the choice of the study region and an analysis mask helped us to limit some issues related to reduced accuracy of satellite soil moisture products over snow-covered or densely vegetated areas (Dorigo et al., 2017; Liu et al., 2012; Wagner et al., 1999). Given the climatic characteristics of the study region, inaccuracy of satellite data over frozen soils was not significant, and limiting the analysis to croplands enabled us to significantly reduce (but not eradicate) issues connected to areas of dense vegetation and high topographic complexity. For further details regarding the ESA CCI soil moisture product the reader is referred to Liu et al. (2012, 2011), Dorigo et al. (2017, 2015) and Wagner et al. (2012).

- The MERRA-2 product is an atmospheric reanalysis product produced by Nasa's Global Modeling and Assimilation Office (GMAO) with version 5.12.4 of the Goddard Earth

Observation System (GEOS-5) atmospheric data assimilation (DA) system (Gelaro et al., 2017). It provides global estimates of land SSM conditions from 1980 to present, at 0.5°x0.625°/1-hourly spatial/temporal resolution. In this study, we focused on the daily level of soil moisture at 00:30 UTC from the surface soil layer (0-5 cm). We used data from the Root Zone (RZ) soil layer of MERRA-2 (0-100 cm) as an additional experiment to further test the relationship between soil moisture within different soil layers and vegetation species. For further details regarding MERRA-2 retrospective analysis data products the reader is referred to Gelaro et al. (2017) and Reichle et al. (2017).

- The Indian Meteorological Institute rainfall gridded dataset (IMD, https://mausam.imd.gov.in/) is prepared using daily rainfall data from 6329 stations, archived at the National Data Center, IMD, Pune. Out of these 6329 stations, 537 stations are IMD observatory stations, 522 are operated under the Hydro-meteorology program and 70 are Agriculture meteorological stations. The remaining stations are rainfall-reporting stations maintained by state governments. The product has a 25 km spatial resolution and spans the years 1901 to 2017.

Hereinafter, the three datasets will be indicated as ESA CCI SM, MERRA-2 SM and IMD Rainfall.

2.1.4 Land cover and irrigation maps

The extent of the study area was limited to croplands to focus the analysis on crop yield and ensure good- quality satellite observations, reducing dense vegetation and topography issues. For this, annual ESA CCI Land Cover (ESA CCI LC) maps version 2.0.7 on a global scale were selected. Data products can be downloaded from http://maps.elie.ucl.ac.be/CCI/viewer/download.php. The dataset is available for the whole study period (1998-2015) at a spatial resolution of 300 m. These maps describe the Earth's terrestrial surface in 37 land-cover classes based on the United Nations Land Cover Classification System (UN-LCCS; Di Gregorio, 2005).

An additional analysis, considering only irrigated areas, was carried out for wheat growing during the drier winter period (assumed to be a potentially irrigated crop). High resolution/annual irrigated-area maps are now available through the work of Ambika et al.

(2016). The maps, with a spatial resolution of 250 m, were developed using 250 m Normalized Difference Vegetation Index (NDVI) data from Moderate Resolution Imaging Spectroradiometer (MODIS) and 56 m land use/land cover data.

2.1.5 Standardized drought indices: SSI and SPI

Computing a Standardized drought index follows defined steps, which are almost analogous for SSI and SPI. The rainfall and soil moisture datasets used are summed and averaged, respectively, on a monthly basis, and successively summed (rainfall) or averaged (soil moisture) over k months, called accumulation periods or time scales. A statistical distribution function is fitted to the rainfall/soil moisture values for the different months of the year. The percentile value from this probability distribution is then transformed to the corresponding value in the standard normal cumulative probability distribution function, to obtain a Standardized drought index (Guttman, 1999; McKee et al., 1993). One of the main limitations when computing SPIs, as compared to SSIs, is the presence of long periods with zero rainfall in the time series, especially for short-accumulation periods. This is a common issue in regions that have seasons with extremely low precipitation, as it is the case with the Indian winter. To overcome this limitation, we referred to the work of Stagge et al. (2015), which used the equation (2.1) for computing SPI:

$$p(x) = \begin{cases} p_0 + (1 - p_0)F\left(x_{p>0}, \lambda\right) & x > 0 \\ \frac{n_{p=0}+1}{2(n+1)} & x = 0 \end{cases} \quad (2.1)$$

In this equation, p is the probability distribution, $F(x,\lambda)$ represents a parametric probability distribution function, $n_{p=0}$ is the number of samples in the reference period where total precipitation equals zero, n represents the total number of samples and p_0 is the probability of zero precipitation following the Weibull plotting position function ($p_0 = n_{p=0}/n+1$). When $x=0$ the equation becomes equal to the mean probability of multiple zeros based on the Weibull plotting position formula.

According to previous literature studies (McKee et al., 1993; Stagge et al., 2015), the gamma distribution function can be used to fit rainfall datasets, as it provides a reliable fit to rainfall distribution. Conversely, the selection process of a statistical distribution to be used for soil moisture data requires more attention. Indeed, only a few authors have evaluated SSI, and some

of them (Carrão et al., 2016; Farahmand and AghaKouchak, 2015) made use of a non-parametric empirical distribution approach. In this study, a test using the plotting position formula (Farahmand and AghaKouchak, 2015) to fit soil moisture datasets was carried out. This resulted in SSI peaks being cut in the range [-2,2] and the general loss of exceptional drought events. According to Sol'áková et al. (2014), this can partly be explained by extreme values being better represented by parametric distributions than non-parametric ones. Zhang et al. (2017) used the gamma distribution to fit both rainfall and soil moisture data from the Indo Gangetic Plain of northern India. Following their work, and also to allow a robust comparison between the SSIs and the SPI, we selected the gamma parametric approach for calculating both types of indices. In addition, the Kolmogorov- Smirnov (Massey Jr, 1951; Stephens, 1974) and Shapiro-Wilk (Shapiro and Wilk, 1965) tests were applied to check the fit and normality of the distributions, respectively, for time scales of 1, 3, 6, 12 and 24 months (the reader can refer to Stagge et al., 2015 for further details on the procedure). For short accumulation periods (1-3 months), the soil moisture indices performed well, while the SPI showed acceptable results for time scales of three months or longer.

As a general observation, 99.9% of Standardized index values lie in the range [-3,3] and negative/positive SPI and SSI values indicate an accumulated deficit/surplus of precipitation or soil moisture over a specified period. More specifically, we used the SPI classification system proposed by McKee et al. (1993), which enables drought conditions to be determined at different time scales, and facilitates monitoring of different drought types. The same system was used for SSI following the work of Carrão et al. (2016). Based on that, hereinafter periods characterized by SPI/SSI<0 will be considered as "drought" conditions – i.e., drought events from mild to extreme as denoted by McKee et al., (1993). Conversely, periods characterized by SPI/SSI>0, will be denoted as "non-drought" conditions.

2.1.6 Experimental setup

The methodological approach used for this study was chosen in line with the main objective of this work, i.e. to highlight the added-value of information about crop yields in drought and non-drought conditions contained within satellite-based soil moisture observations, as compared to reanalysis-based soil moisture and rainfall observations. To fulfill the purpose, we took the

following steps (summarized in Figure 2.2):

Step 1. Indices computation: This is a preliminary step for obtaining SSI and SPI drought indices from the ESA CCI SM product, MERRA-2 SM estimates and IMD Rainfall observations. To compare soil moisture products and rainfall at the same spatial resolution, MERRA-2 SM was re-gridded over the ESA CCI SM product spatial grid (0.25°) using the nearest-neighbor approach. Three indices (SSI CCI, SSI MERRA2 and SPI) were calculated using the methodology described in Section 2.1.5. The cropland mask and the identification of irrigated areas were considered as source information to limit the extension of the indices data within the study area in case of an analysis over all croplands, or considering irrigated conditions respectively. ESA CCI LC maps available for the study period were used to derive the percentage of cropland, averaged over time, within each pixel of the SSI and SPI drought indices. In the UN-LCCS classification, cropland areas refer to four different classes: 1) cropland rainfed; 2) cropland irrigated or post-flooding; 3) >50% mosaic cropland / <50% natural vegetation; and 4) >50% mosaic natural vegetation / <50% cropland. Pixels of yearly ESA CCI LC maps accounting for these classes were selected by counting the number included in the 0.25°x0.25° area of each SSI and SPI pixel, and averaging them over the study period. Finally, cropland percentage was calculated for each pixel of the indices, with only ones having a percentage of >50% cropland retained. Creating such an agricultural mask can partly overcome limitations related to soil moisture (linked particularly to microwave retrievals) such as complex topography, surface water, urban structures (Wagner et al., 1999) and vegetation density (Liu et al., 2012). Additionally, irrigated areas of croplands were identified using high-resolution irrigated-area maps (Ambika et al., 2016). The same methodology applied to the ESA CCI LC maps was used, selecting only those pixels having a percentage of irrigated area higher than 2%. This threshold better reproduced the pattern of irrigated area maps from Ambika et al. (2016).

Step 2. Indices intercomparison: The SSI and SPI were evaluated at different time scales to find the appropriate scale for each index to be used for agricultural drought analysis. This highlighted the main difference between the two indices: SPI commonly represents the rapid development of meteorological drought resulting from rainfall deficit, while reduced soil moisture (agricultural

drought) may occur with some time lag (Farahmand and AghaKouchak, 2015). The basic assumption is that a 1-month time scale (SSI-1 – derived from monthly soil moisture values) is an appropriate indicator of soil moisture deficit for assessing agricultural drought, similar to a Soil Water Deficit Index (i.e. SWDI; Martínez-Fernández et al., 2015). For this study, a correlation analysis was conducted between SSI-1 and SPI at different time scales to select the SPI accumulation period that correlated most closely with SSI-1, and was thus more suitable for agricultural drought assessment. The analysis was realized averaging the indices over the study area (considering the cropland mask).

Step 3. Sensitivity analysis: In this step, a spatial average of indices on a district basis was computed to obtain a single monthly time series for SSI CCI, SSI MERRA2 and SPI over each district. Then, the relation between values of the indices for each month of maize/wheat agricultural production and annual yield data was investigated by calculating the Pearson correlation coefficient (R). This was carried out to identify months in which crops were more sensitive to SSI/SPI indices and in this context, the term "sensitivity analysis" refers to the identification of months showing a high correlation between indices and crop yields. Months characterized by the highest number of districts having Pearson R-values higher than 0.5 were selected to obtain a seasonal average for each drought index and, therefore, a district-level annual time series related to crop-yield data. Note that hereinafter the term "annual" will refer to the seasonal average carried out on the months selected in this step. Values above the 0.5 R-value threshold can be considered medium-high correlated (Hinkle et al., 2003) and therefore are deemed sufficiently indicative of a relation between drought indices and crop-yield data.

Step 4. correlation analysis: In accordance with previous literature studies (Carrão et al., 2016; Narasimhan and Srinivasan, 2005; Zhang et al., 2017), a correlation analysis between the indices and crop-yield data was performed to investigate the link between drought conditions and crop production. In a previous phase, crop data series were converted into yield anomalies to get rid of the potential impact of technological advancement during time on crop production. Following the work of Gunst et al. (2014) a linear regression was applied to crop-yield data to remove potential linear trends with a Pearson R-value significance level of 0.05 (when p-value<0.05).

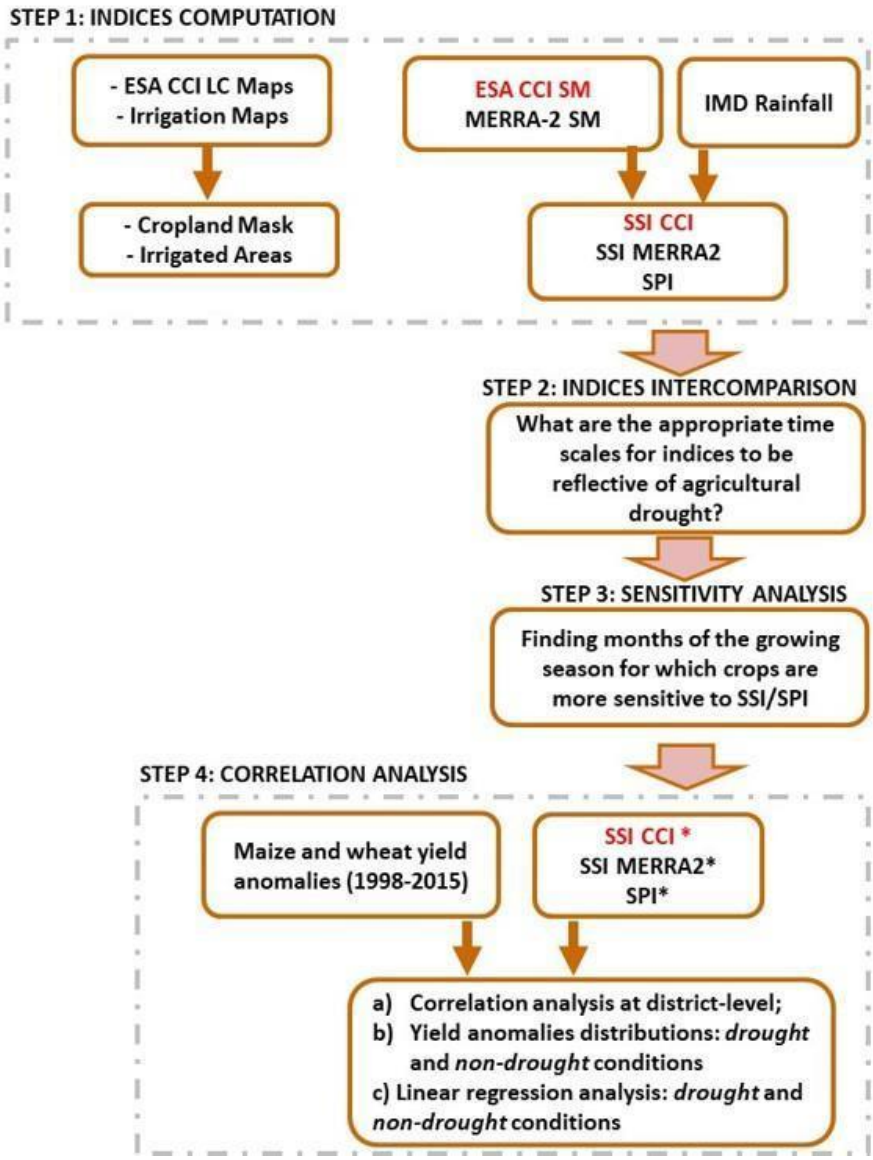

Figure 2.2. Experimental set-up tuned to study objectives: STEP 1 – Indices computation (SSI CCI, SSI MERRA2 and SPI); STEP 2 – Indices intercomparison; STEP 3 – Sensitivity analysis; and STEP 4 – Correlation analysis with crop yield anomalies. Note: * indicates spatially and annually averaged indices time series, for each district, using an appropriate time scale selected for agricultural drought analysis.

When linear trends were not found, the mean was removed from the yield's time series. As an example, plots providing maize and crop yield anomalies for five districts of Maharashtra and Karnataka states are shown in Figure 2.3. Subsequently, the relation between yield anomalies and indices values was explored during the following stages: a) a first correlation analysis at district level over the cropland mask was conducted. Districts characterized by p-value<0.05 were

identified, and the data (index and yield anomalies values) were used to build samples for a further analysis over the whole study area; b) the distributions of crop-yield anomalies in drought and non-drought conditions were investigated; c) same-data samples were used additionally for a linear regression analysis between drought indices and yield anomalies. Plots containing linear regression parameters were also divided into two bands, evaluating the Pearson R-values in drought and non-drought conditions.

The same analysis was then conducted considering only irrigated areas for wheat.

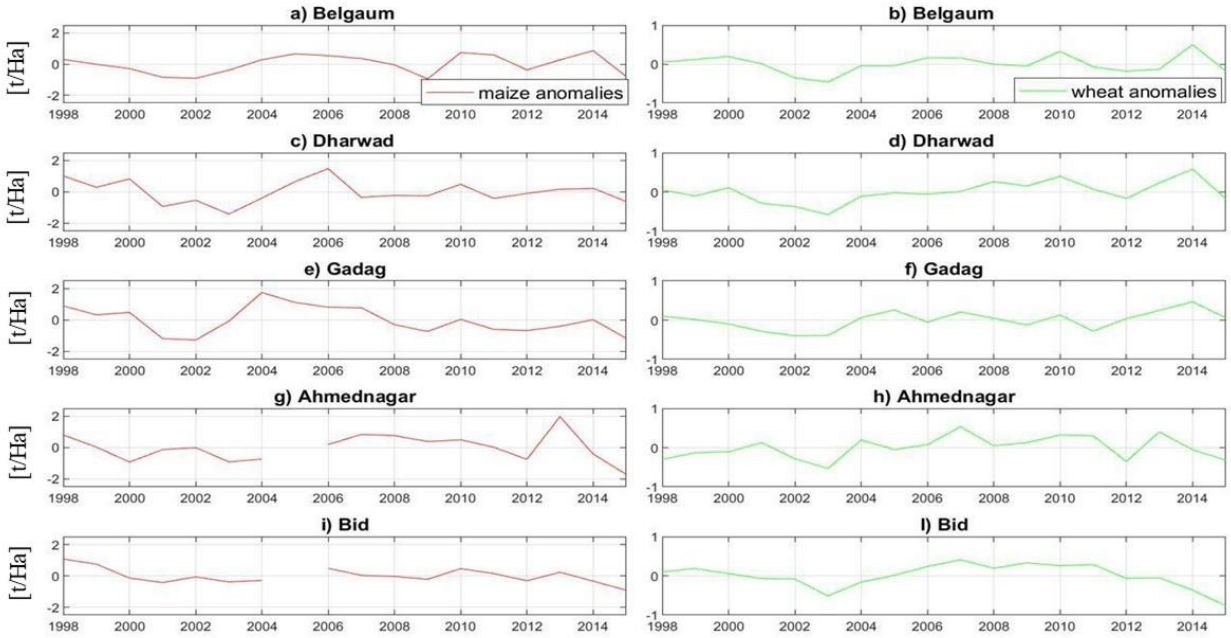

Figure 2.3. Maize and wheat anomalies, respectively in red and green for three districts of Karnataka (Belgaum, Dharwad and Gadag) and two districts of Maharashtra (Ahmednagar and Bid).

2.2 Results and discussion

2.2.1 Assessment of drought indices

The Standardized drought indices were calculated by applying the methodology described in *Step 1* of Section 2.1.6. The maps presented in Figure 2.4 show the SSI and SPI pixels belonging to the cropland mask (Figure 2.4a) and to the irrigated areas (Figure 2.4b) over the two Indian states.

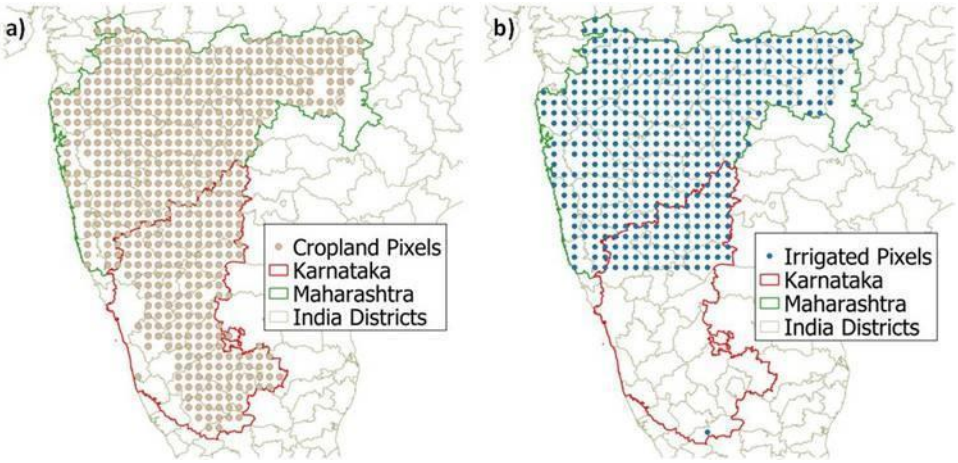

Figure 2.4. Maps of: (a) SSI and SPI pixels (0.25° spatial resolution) belonging to the cropland mask; (b) SSI and SPI pixels (0.25° spatial resolution) belonging to irrigated areas. Pixels with more than 50% of the total area used for agricultural purposes were selected to create the cropland mask, while for the irrigated areas a threshold of 2% was selected.

In this analysis, SSI-1 was chosen as reference for agricultural drought analysis. Assuming that SPI is commonly considered as a meteorological drought index, a correlation analysis was carried out between SSI-1 and SPI time series at different time scales (1, 3, 6, 12 and 24 months) in order to detect the lag time between the two indices for agricultural drought analysis, thus ensuring a meaningful comparison between them. The relation between SPI and SSI-1 CCI showed R-values varying from a maximum of 0.6 for SPI-3 and a minimum of 0.4 for SPI-24. Similarly, in the analysis between SPI and SSI-1 MERRA2, the highest R-value was equal to 0.72 for SPI-3 (Figure 2.5). Based on that, SPI-3 was assumed to be representative for describing agricultural drought conditions. Previous works on agricultural drought analysis also selected SPI-3 (i.e., Bachmair et al., 2018; Lim et al., 2019; Sigdel and Ikeda, 2010), supporting our decision. For example, Bachmair et al. (2018) performed a correlation analysis between SPI at different time scales and RS-based vegetation indices (VIs) for Europe. They showed that short accumulation periods of SPI (in particular three months) relate well to crop vegetation stress in most cases.

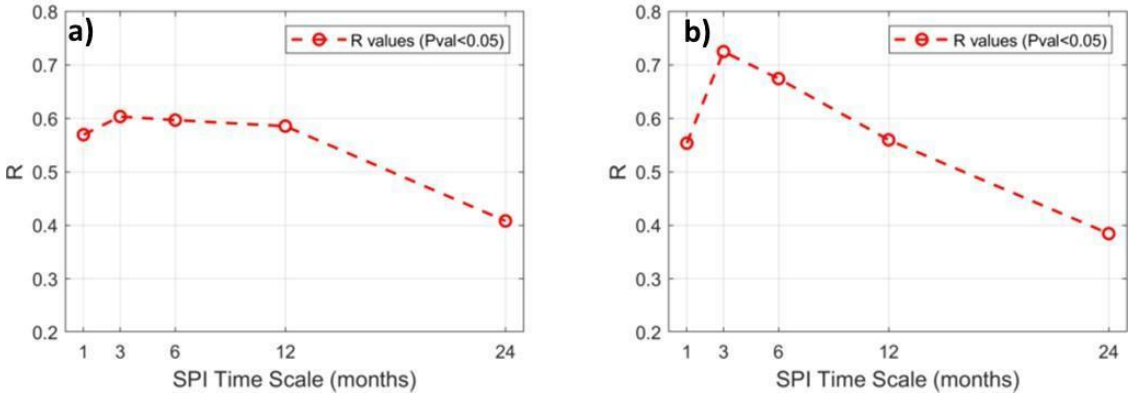

Figure 2.5. Pearson R-values obtained by the correlation analysis between (a) SSI-1 CCI and SPI-1,3,6,12 months' time scale; (b) SSI-1 MERRA2 and SPI-1,3,6,12 months' time scale. The results showed the best correlation between SSI-1 and SPI-3, assuming a lag time of three months between the two indices.

Thereafter, a comparison between the SSI-1 and SPI-3 indices was carried out. The time series of SSI-1 CCI, SSI-1 MERRA2 and SPI-3, averaged over croplands for the two states of Maharashtra and Karnataka in the period 1998-2015 are displayed in Figure 2.6 (a-f). The color blue depicts wet or healthy conditions, while red denotes drought conditions.

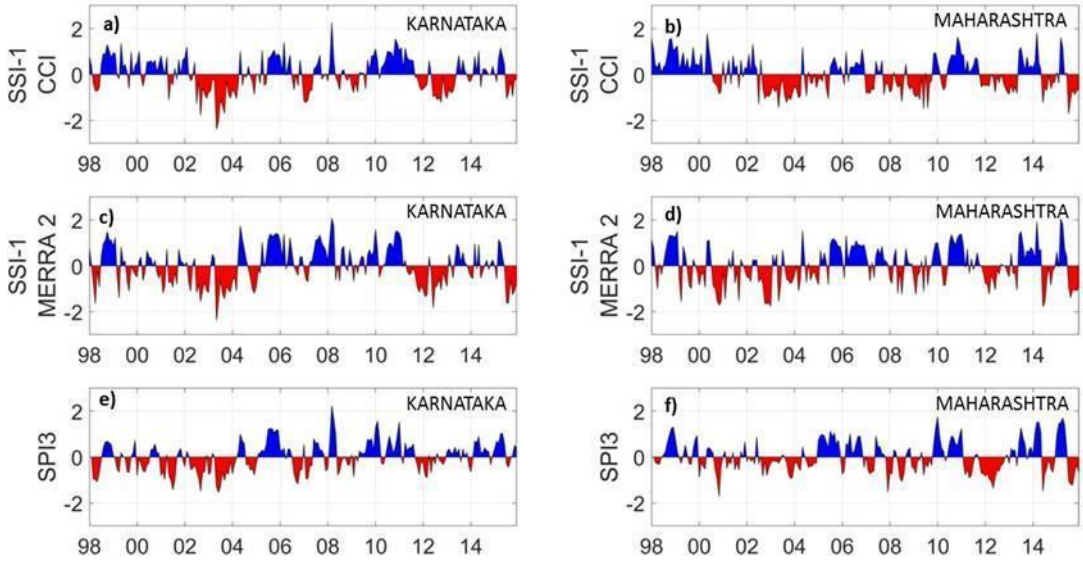

Figure 2.6. Time series of the indices averaged over Karnataka: (a) SSI-1 CCI; (c) SSI-1 MERRA2 and (e) SPI-3. Time series of the indices averaged over Maharashtra: (b) SSI-1 CCI; (d) SSI-1 MERRA2 and (f) SPI-3. Blue depicts wet conditions; red denotes drought conditions.

The time series follow a similar temporal pattern but with some exceptions, particularly in Maharashtra where SSI-1 CCI shows wetter conditions from 1998 until 2000, as compared to the other indices (Figure 2.6b). Otherwise the three indices show good agreement in correctly

detecting typical drought events: 1) for Karnataka (Figure 2.6a, c, e) in 2001, 2002, 2003, 2004 and 2012. Additionally, the 2009 drought event reported by Jayasree and Venkatesh (2015)can be identified as a mild drought; and 2) for Maharashtra (Figure 2.6b, d, f) in 2012 and 2015 (D Udmale et al., 2014; Mishra et al., 2016). Soil moisture and precipitation indices show a different behavior during typical drought events. A good example is given by the consecutive droughts that occurred in Karnataka from 2002. The 2002 event was quite important, having a seasonal rainfall deficit of 21.5% and being 56% below normal for the month of July (Bhat, 2006). SSI-1 CCI shows one big drought event from mid-2002 to the beginning of 2004, reaching extreme drought conditions in 2003, while SPI-3 displays almost two recoveries in the same period with higher index values. Considering the same time window, SSI-1 MERRA2 shows a short recovery in 2003, followed by an extreme drought event. Analogous conditions are shown in 2015 when a drought occurred during the monsoon season and affected the agriculture sector in many parts of the country, including Maharashtra state (Mishra et al., 2016). Figure 2.6b, d and f show that this event persisted until the end of 2015. In general, all the indices identify this event but lower values are displayed by SSI-1 indices as compared to SPI-3. The difference between SSI and SPI in relation to the duration of drought events could be due to the 'persistence' property of soil moisture, which exhibits less variability in time than precipitation (Hao and AghaKouchak, 2013). On the other hand, the higher severity of drought denoted by the soil moisture indices could relate to the low depth of the surface soil layer (0-5 cm), which is more reactive to atmospheric factors (e.g. rainfall events or dry spells). For a supplementary comparison between the time series we calculated the Pearson correlation coefficient (considering p-values<0.05). As expected, highest R-values of 0.78 and 0.74 were obtained for SSI-1 CCI against SSI-1 MERRA2 in Karnataka and Maharashtra, respectively. Also, SSI-1 MERRA2 compared to SPI-3 showed relatively high R-values of 0.69 for Karnataka and 0.71 for Maharashtra. The weaker relation was instead found for SSI-1 CCI against SPI-3 although the Pearson R-value did not drop below 0.55 in both the states.

Thereafter, the spatial distribution of two main drought events was analyzed: 1) the 2003 event which involved mainly Karnataka; and 2) the 2015 event in Maharashtra, which started in the monsoon season and also affected the emergence stage of winter crops (i.e., wheat). In the maps

of Figure 2.7a-c the spatial and frequency distributions for SSI-1 CCI, SSI-1 MERRA2 and SPI-3, respectively, are shown for July 2003. Water stress at this time of year can affect crops cultivated during the monsoon season (i.e., maize). The three indices detect the event in Karnataka. In particular, SSI-1 CCI (Figure 2.7a) and SPI-3 (Figure 2.7c) show more severe drought conditions in Karnataka and in southwestern and western parts of Maharashtra than SSI-1 MERRA2 (Figure 2.7b), which displays the same pattern in Karnataka but with index values closer to -1. The frequency distributions, included in the maps, are skewed to the left in the case of the two soil moisture indices, while SPI-3 shows a more symmetrical distribution, with most of the values lower than zero. Similarly, SSI-1 CCI (Figure 2.7a) displays an asymmetric distribution, featuring more severe drought conditions and reaching index values below -3. For the event of 2015, the spatial distribution of the indices' values during November 2015 was reported, corresponding to the emergence stage of wheat. In Figure 2.7d-f results are shown for SSI-1 CCI, SSI-1 MERRA2 and SPI-3. Here SPI-3 (Figure 2.7f) displays a mild drought in Maharashtra, while the soil moisture indices show the persistence of more severe drought conditions. In particular, the frequency distribution of SSI-1 MERRA2 (Figure 2.7e) is almost totally shifted to the left. The results for November 2015 agree with the averaged time series in Figure 2.6, where the higher severity is reflected by the modeled soil moisture index. It should be noted, with regard to the two soil moisture products, that the maps in Figure 2.7 clearly show the influence of the original coarser resolution of MERRA-2, compared to the highest resolution of satellite soil moisture observations.

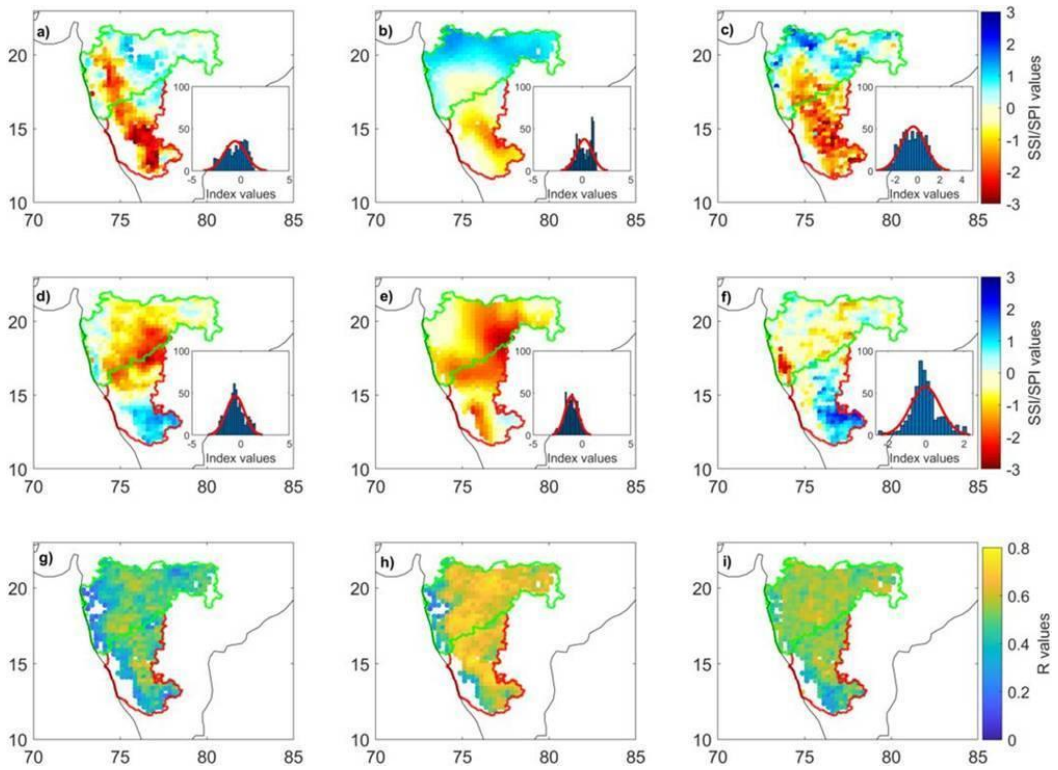

Figure 2.7. Maps and frequency distributions of drought indices: (a) SSI-1 CCI, (b) SSI-1 MERRA2 and (c) SPI-3 in July 2003. Maps and frequency distribution of drought indices: (d) SSI-1 CCI, (e) SSI-1 MERRA2 and (f) SPI-3 in November 2015. Maps of Pearson temporal correlation pattern over the study area between: g) SSI-1 CCI and SPI-3; h) SSI-1 CCI and SSI-1 MERRA2; and i) SSI-1 MERRA2 and SPI-3. In the last three figures, all R-values are taken at a significance level of 5%. In each plot, the x- and y-axes represent longitudes and latitudes in degrees east and north, respectively.

The temporal correlation between the indices over each pixel of the study area was also investigated (Figure 2.7g-i). The map of SSI-1 CCI against SPI-3 (Figure 2.7g) shows a median R-value of 0.46, with lower correlations on the boundaries of the study area and in particular in the western, north-western and northern parts of Maharashtra. A similar but less extensive pattern is found in Figure 2.7h, where SSI-1 CCI is compared to SSI-1 MERRA2. The weaker relations between SSI-1 CCI and the other two indices in these areas could be due to the coarse resolution of the ESA CCI SM product over topographically complex and densely vegetated areas, particularly over the Western Ghats chain and Satpura range. In these regions the cropland mask computational process can be affected by uncertainties in reducing typical satellite soil moisture issues. Based on our hypothesis that at least 50% of each pixel area should be covered by crop in order to consider the pixel itself as cropland, we have to be aware that other land uses can be embedded in 0.25° spatial resolution pixels, and they may marginally affect satellite soil moisture retrievals. In contrast, the map of SSI-1 CCI against SPI-3 shows R-values higher than 0.5 over the

Deccan Plateau, where the issues related to topographic complexity and dense vegetation have negligible relevance. A similar pattern was observed for SSI-1 CCI against SSI-1 MERRA2, with higher R-values (ranging from 0.6 to 0.8). Finally, in the map of Figure 2.7i, showing SSI-1 MERRA2 against SPI-3, R-values between 0.5 and 0.8 are homogeneously distributed over the Deccan Plateau, with lower correlation coefficients in the southwestern part of the study area. Although topography and vegetation can affect satellite retrievals in the study area, problems related to frozen soils, snow and ice (Ulaby et al., 1982) are not significant, given the climatic characteristics of the study region.

2.2.2 Crop yields vs drought indices

In this section, we examine results showing the relation between crop yield and drought indices to understand if satellite SSM observations can provide additional information on crop production, particularly in drought conditions, when compared to soil moisture estimates from land surface models (LSMs) and rainfall-based indices. Following *Step 3* in section 2.1.6, the SSI/SPI indices were averaged at district level to obtain a monthly time series for each district for which crop-yield data were available. Then, the sensitivity analysis was performed to select the months for which crops were most sensitive to SSI/SPI (results are shown in Table 2.1).

For maize, all the indices identify these months as being July, August and September (monsoon period). These months correspond with the later growth stage of maize, starting when potential plant parts are developed and ending when the actual kernel weight is determined. In this period, soil moisture plays a central role warding off potential yield losses; see Darby and Lauer (2004) for more information regarding growing stages of maize. Conversely, for wheat the sensitivity analysis gave a higher number of districts with R-values>0.5 for the soil moisture indices, mostly in the months of October, November and December. As an exception, SSI-1 CCI showed acceptable results also in February. This is consistent with Zhang et al. (2017) who found a close relation between a soil moisture drought index (SSI) and wheat during October, November and February in the Indo-Gangetic Plain, the northern region that separates the Peninsula from the Himalayan chain. Meanwhile, SPI-3 only showed a conspicuous number of correlated districts for the month of October. We decided then to retain the months of October and November. These

months correspond with the emergence stage of wheat; an analysis related to this period could be interesting to understand the positive or negative evolution of the harvest. Note that, given the extension of the study area and the potential differences in timing of rainfall occurrence both within the district and within the entire study area, a monthly time scale seems to be the most appropriate scale to carry out the analysis. Conversely for analyses at smaller spatial scales, a shorter accumulation period should be considered.

Table 2.1. Number of districts with Pearson R-values higher than 0.5 over each month of the growing seasons of maize and wheat for the three drought indices.

	Wheat growing season							Maize growing season			
Drought index	Oct.	Nov.	Dec.	Jan.	Feb.	Mar.	Apr.	Jun.	Jul.	Aug.	Sept.
SSI-1 CCI	11	14	16	9	10	8	3	5	16	19	20
SSI-1 MERRA2	16	16	12	6	2	1	5	2	13	15	14
SPI-3	8	3	2	2	1	1	0	1	10	14	13

The correlation analysis between indices and yield anomalies at district level (described in *Step 4* of Section 2.1.6) was conducted over cropland areas, without specific distinction being made between rainfed and irrigated conditions. The analysis was then carried out on 50 and 43 districts for maize and wheat, respectively, corresponding to croplands where crop-yield data were available. Figures 2.8a to 2.8c show the number of districts characterized by correlations with a significance level of 0.05 (p-value<0.05) and the respective R-values obtained for maize. Light brown was used to display the 50 districts over which the analysis was conducted, with blue shades used to identify the value of Pearson correlation (p-value<0.05) between crop-yield anomalies and the indices. The correlation patterns are similar for the three investigated indices. However, SSI-1 CCI (Figure 2.8a) provided the best performance, with the 54% of the districts (27 districts) showing R-values greater than 0.4, and 21 districts with R-values higher than 0.5. SSI-1 MERRA2 (Figure 2.8b) and SPI-3 (Figure 2.8c) display lower performances, with 32% and 30% of significantly correlated districts, respectively (16 and 15 districts).

Results for wheat are displayed in Figure 2.8d to 2.8f. Soil moisture indices in general seem to

obtain better agreement with yield anomalies than SPI (Figure 2.8f), which accounts only for 16.3% of the districts (7 districts) with Pearson R-values higher than 0.4. Similar results were found for SSI-1 CCI (Figure 2.8d) and SSI-1 MERRA2 (Figure 2.8e), where 34.9% and 39.5% of the districts' (15 and 17 districts, respectively) crop-yield data and indices are significantly correlated.

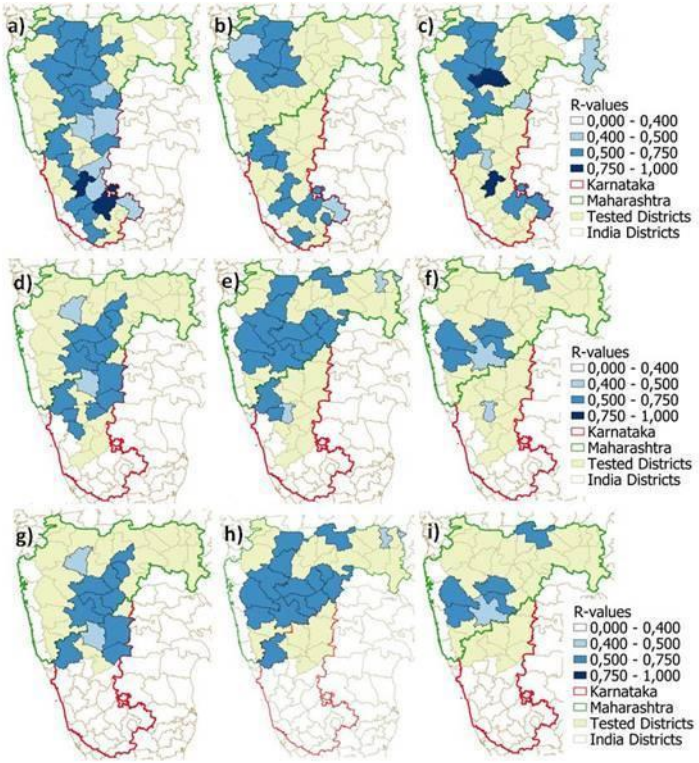

Figure 2.8. Maps showing the relation between district mean annual values of the three indices and crop yield anomalies: maize anomalies against (a) SSI-1 CCI, (b) SSI-1 MERRA2 and (c) SPI-3; wheat anomalies against (d) SSI-1 CCI, (e) SSI-1 MERRA2 and (f) SPI-3; and wheat anomalies against (g) SSI-1 CCI, (h) SSI-1 MERRA2 and (i) SPI-3 over irrigated areas. The tested districts (light yellow) on the maps (a) – (f) represent croplands where crop-yield data were available. The tested districts in the maps (g) – (i) represent irrigated areas where wheat-yield data were available. Only districts characterized by R-values with a significance level of 0.05 (p-values<0.05) are displayed in different blue shades, depending on the Pearson R-values.

One of the most striking aspects of this analysis is that there is a different geographic distribution of districts with significant correlations for the three indices, and this is particularly evident for wheat. In this case, SSI-1 MERRA2 (Figure 2.8e) and SPI-3 (Figure 2.8f) seem to follow the same geographic pattern, even though SPI-3 shows poor performance. A slightly different distribution of significant R-values is instead displayed in the map of SSI-1 CCI (Figure 2.8d). Generally, discrepancies between the two soil moisture indices can be due to the uncertainties of satellite retrievals in areas characterized by complex topography and dense vegetation, along with

uncertainties related to model input data for MERRA-2 soil moisture estimates. For maize, dissimilarities can be detected in the distribution and R-values for significantly correlated districts between SSI-1 CCI (Figure 2.8a) and SPI-3 (Figure 2.8c). Although SPI-3 performs less well, it seems to agree better with maize yield anomalies in four districts: one in the center of Maharashtra, two in the north-eastern Maharashtra and one in the south-eastern Karnataka (this last one in proximity to the eastern Ghats). Considering that maize grows during the monsoon season and that satellite soil moisture can be affected by retrieval uncertainties, the precipitation index can, in practice, show good agreement with crop yields in the rainy season. In this respect, it is worth mentioning that DA techniques could represent a viable solution to integrate model and satellite observations, in order to improve model predictions and to overcome satellite observation limitations.

To further explore the results achieved by the indices for wheat (i.e., irrigated) an additional correlation analysis between indices and yield anomalies was carried out for irrigated areas only. The aim was to investigate whether satellite soil moisture, albeit at coarse resolution, is able to give additional information on harvest data compared to MERRA-2 modeled soil moisture and observed precipitation data, which do not include information on irrigation. For this purpose, high-resolution irrigated-area maps available for the study period (Ambika et al., 2016) were used to find the percentage of irrigated areas over each pixel of the three indices (see Figure 2.4b for the map of irrigated SSI and SPI pixels). Thirty-six districts were selected for this analysis, corresponding to irrigated areas where crop-yield data were available. We obtained significant R-values in 12 districts for SSI-1 CCI (Figure 2.8g), 15 districts for SSI-1 MERRA2 (Figure 2.8h) and 6 districts for SPI-3 (Figure 2.8i), which correspond to the 33.3%, 41.66% and 16.66% of the total number of districts, respectively. At this level of analysis, we did not find improvements in the use of the satellite-based drought index as compared to SSI-1 MERRA2 and SPI-3. This could be explained by the inherent uncertainty associated with the identification of irrigated areas versus the relatively coarse spatial resolution of the satellite soil moisture product. In this respect, it is worth mentioning that irrigation detection is not always straightforward and can lead to significant uncertainties (Brocca et al., 2018; Lawston et al., 2017).

Note that before focusing on modeled SSM, we compared its performance at district level, with that of a RZ-based SSI MERRA2, as crop yield is expected to be physically related to deeper soil layers. After calculating the index, we investigated the correlation between SSI-1 MERRA2 RZ and crop-yield anomalies. Unexpectedly, we found the performance of this index to be lower in terms of R-values as compared to the SSM SSI-1 MERRA2, particularly for wheat. In this case many of the districts significantly correlated are characterized by R-values lower than 0.5. This additional analysis further justified our choice of using the modeled SSM of MERRA2 (0-5 cm) and also highlighted the key role of SSM in the growing process of the selected crops. Details are reported in Figure 2.9.

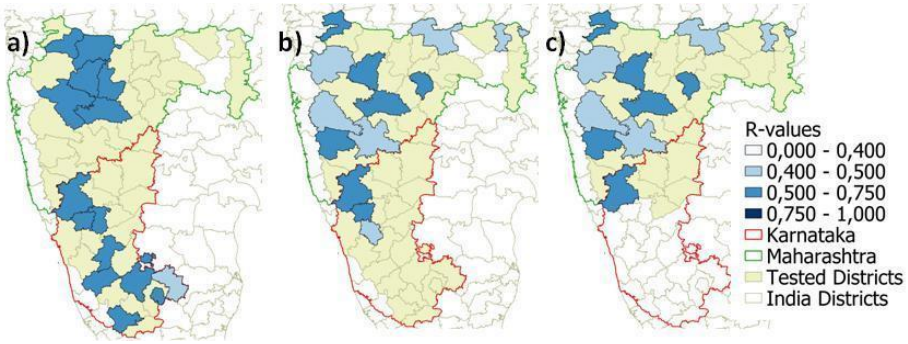

Figure 2.9. Maps showing the relationship between district mean annual values of SSI-1 MERRA2 RZ against (a) maize anomalies; (b) wheat anomalies and (c) wheat anomalies over irrigated areas. The tested districts (light yellow) in the maps (a) – (b) represent croplands where crop-yield data were available. The tested districts in the map (c) represent irrigated areas where wheat-yield data were available. Only districts characterized by R-values with a significance level of 0.05 (p-values<0.05) are displayed in different blue shades, depending on the Pearson R-values.

After the first screening process, all the indices data of the districts with significant R-values over the cropland mask were compared to the related yield anomalies. The analysis was carried out as a function of the drought severity in two main classes, i.e., drought (SSI/SPI<0) and non-drought conditions (SSI/SPI>0). For that, we calculated crop data distributions associated to the two classes (Figure 2.10). For the soil moisture indices (Figure 2.10a for SSI-1 CCI and 2.10b for SSI-1 MERRA2), plots between the first and the third quartile show a distinct separation between drought and non-drought conditions for positive and negative maize anomalies, respectively. The same is obtained for wheat (Figure 2.10d-2.10e), although the pattern is less distinct than that of maize. Conversely, for SPI-3 (Figure 2.10c and f) the two distributions intercross each other (especially for wheat), indicating reduced ability for SPI to explain positive and negative crop

anomalies. The latter analysis provides clear evidence of a relation between soil moisture indices and crop-yield anomalies. To understand the strength of this relation, we carried out a linear regression analysis (by assuming a simple linear model for describing the relation between crop yield and drought indices).

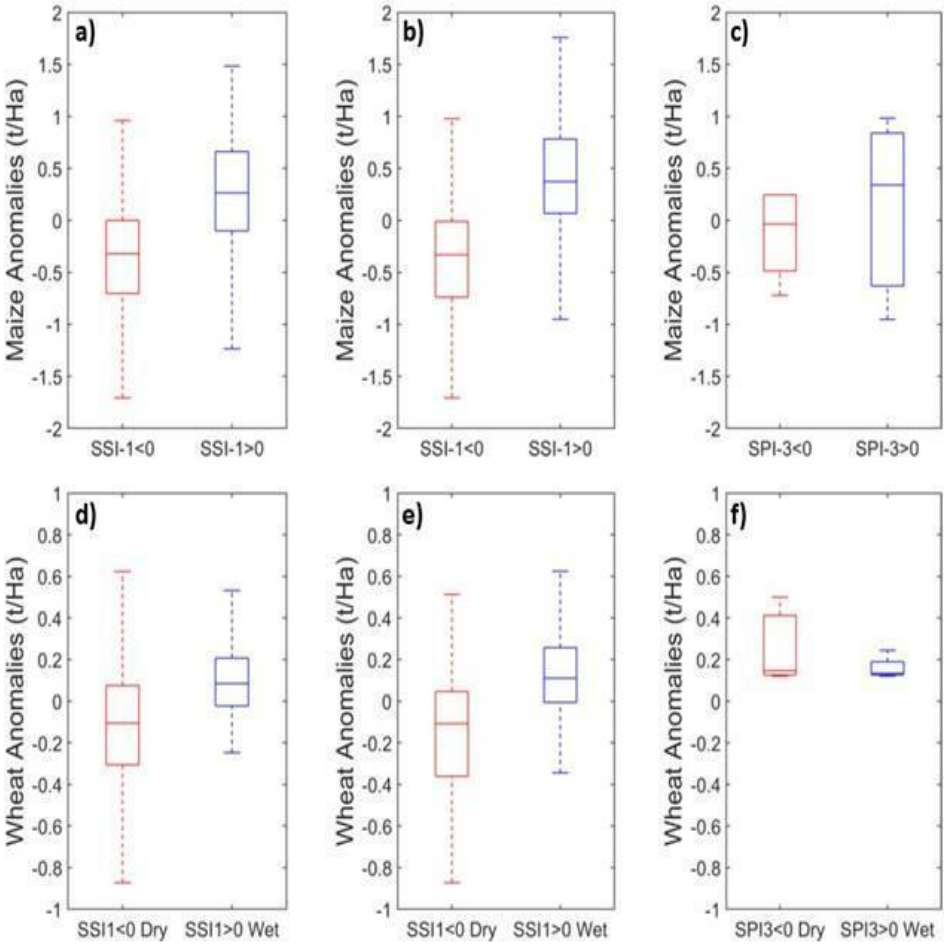

Figure 2.10. Statistics during drought (red) and non-drought (blue) conditions for maize anomalies distribution, with respect to (a) SSI-1 CCI, (b) SSI-1 MERRA2 and (c) SPI-3; and for wheat anomalies distribution with respect to (d) SSI-1 CCI, (e) SSI-1 MERRA2 and (f) SPI-3. Data are related to districts characterized by significant correlation over croplands.

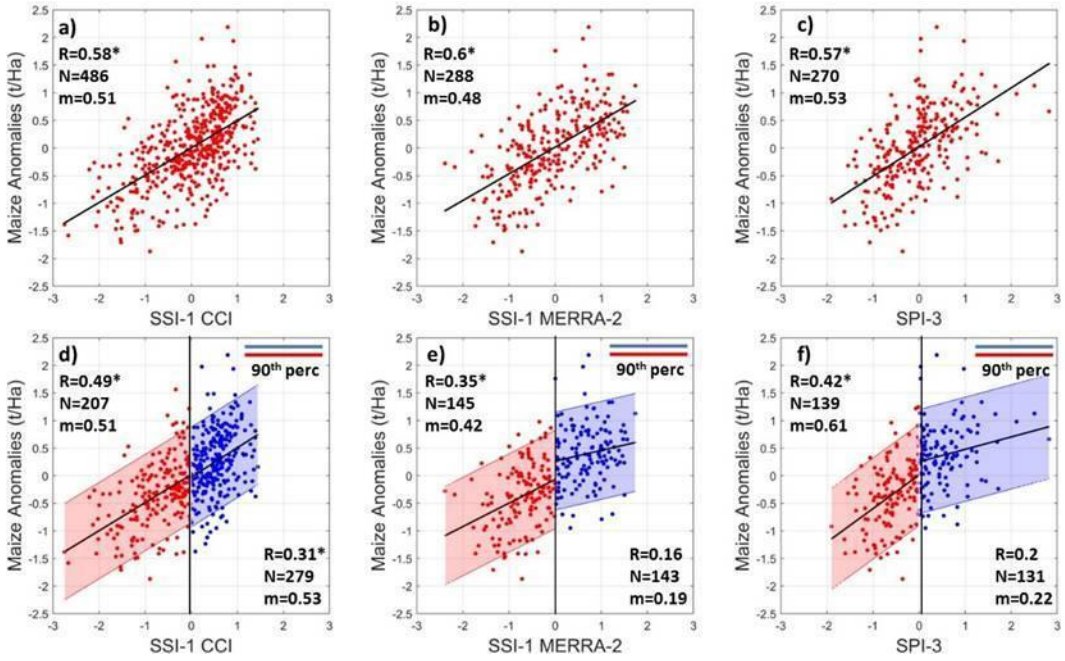

Figure 2.11. Linear regression analysis with data relative to districts characterized by significant correlation over croplands. Samples obtained with maize anomalies and the related SSI-1 CCI, SSI-1 MERRA2 and SPI-3 values are shown in a), b) and c) respectively and then divided considering drought (red) and non-drought (blue) conditions in d), e) and f). Key: (m) is the slope of the regression line, (N) is the sample size and (R) is the Pearson correlation coefficient. Red and blue bands identify the 90th percentiles. Numbers marked as * indicate passing the test of significance ($p < 0.05$).

It is worth notice that the objective of the linear regression analysis here is not to create a model to describe the ability of each index to forecast crop yield, but only to study the sensitivity of harvests data to drought conditions. Additionally, autocorrelation in the data (and their errors) was not accounted for in the marking of significant correlation values. For maize (Figure 2.11) the regression was carried out both regardless of the drought severity (Figure 2.11a-c) and as a function of the severity (i.e. drought vs non-drought, Figure 2.11e-f) for the three indices. In the first case, all the indices show very similar results with R-values of 0.58 for SSI-1 CCI, 0.6 for SSI-1 MERRA2 and 0.57 for SPI-3 (note that the correlations were calculated on different sample sizes N, as a result of the preliminary screening process). For the second case (Figures 2.11d-f), the correlation coefficients are generally lower for the three indices both in drought and non-drought conditions (R-values on the top left- and bottom right-side of each figure). In this case, the results reveal some interesting features that need discussion. That is, SSI-1 CCI displays an R-value of 0.49 in drought conditions with the two bands at 90th percentile showing a similar spread when moving from drought to non-drought conditions. This value is above the values obtained for SSI-

1 MERRA2 (R=0.35) and SPI-3 (R=0.42) suggesting that satellite soil moisture observations retain useful information about the relation between water stress and crop yield. In addition, as correlations during non-drought periods drop significantly for all the three indices, this suggests that the water stress is an important limiting factor for crop production (which is expected) whereas during non-drought periods it plays a minor role, as other factors (i.e., fertilizers) are able to boost the production.

The analysis carried out for maize was then repeated for wheat. As before, we considered two cases: 1) considering all the samples and 2) dividing the samples into drought and non-drought conditions. In the first case, SSI-1 CCI (Figure 2.12a) and SSI-1 MERRA2 (Figure 2.12b) display the same R-value of 0.54, whereas SPI-3 (Figure 2.12c) achieves lower results with R=0.49. For the second case (Figure 2.12d-f), the satellite-based SSI-1 CCI (Figure 2.12d) shows once again highest correlation in drought conditions (R=0.63) as compared to SSI-1 MERRA2 (Figure 2.12e, R=0.5) and SPI-3 (R=0.44). This confirms and strengthens the conclusions revealed by the analysis on maize.

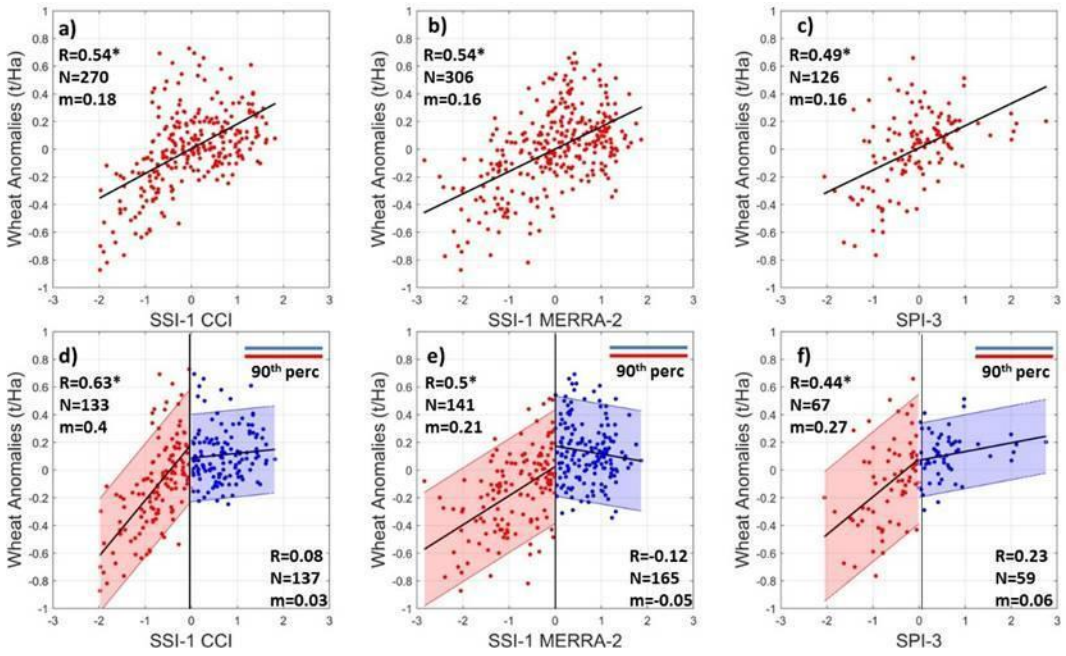

Figure 2.12. Linear regression analysis with data relative to districts characterized by significant correlation over croplands. Samples obtained with wheat anomalies and the related SSI-1 CCI, SSI-1 MERRA2 and SPI-3 values are shown in a), b) and c) respectively, and then divided considering drought (red) and non-drought (blue) conditions in d), e) and f). Key: (m) is the slope of the regression line, (N) is the sample size and (R) is the Pearson correlation

coefficient. Red and blue bands identify the 90th percentiles. Numbers marked as * indicate passing the test of significance ($p < 0.05$).

The same analysis was conducted for wheat in irrigated areas only (Figures 2.13a-c), showing a further increase in the R-value for SSI-1 CCI from 0.63 to 0.66 and a slight reduction of correlation for SSI-1 MERRA2 and SPI. This suggests that satellite soil moisture observations are better able to represent the soil wetness conditions potentially exploited by crops, and related to human processes such as irrigation. This aspect, however, needs further investigation and it will be assessed in the second part of this work.

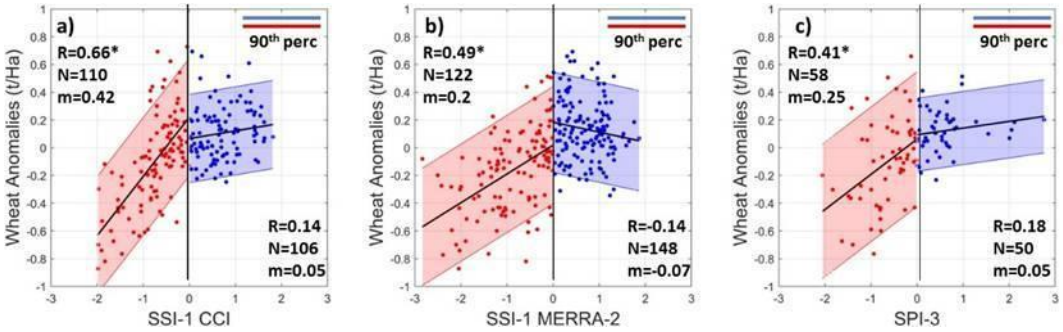

Figure 2.13. Linear regression analysis with data relative to districts characterized by significant correlation in irrigated areas growing wheat. Samples obtained with wheat anomalies and the related SSI-1 CCI, SSI-1 MERRA2 and SPI-3 values, divided considering drought (red) and non-drought (blue) conditions, are shown in a), b) and c). Key: (m) is the slope of the regression line, (N) is the sample size and (R) is the Pearson correlation coefficient. Red and blue bands identify the 90th percentiles. Numbers marked as * indicate passing the test of significance ($p < 0.05$).

It is important to highlight that the reliability of crop data at district level may affect the analysis, adding additional uncertainties. However, satisfactory results were obtained for SSI-1 CCI, especially in drought conditions and particularly regarding wheat. To support our analysis and the good performance achieved by SSI-1 CCI we can refer to the study of Carrão et al. (2016). Here the authors demonstrated the performance of an Empirical Standardized Soil Moisture Index (ESSMI), implemented with the use of ESA CCI SM COMBINED (V02.0), and investigated its relation to maize and wheat in Argentina, over two distinct weather stations. They calculated the Pearson R-value for the whole data sample and obtained high R-values between the index and crop. Although we achieved lower scores than those of Carrão et al. (2016), the performance of SSI-1 CCI seems to be promising, especially in drought conditions.

2.3 Conclusions

In the first part of this thesis, three drought indices were calculated, namely, the SSI-1 derived from long-term ESA CCI soil moisture product from active and passive microwave sensors (combined version), the SSI-1 from MERRA2 reanalysis of SSM estimates, and the SPI-3 from the Indian Meteorological Institute rainfall observations (SSI-1 CCI, SSI-1 MERRA2 and SPI-3 respectively). These indices were examined in relation to maize and wheat crop-yield data in Maharashtra and Karnataka states (India) from 1998 to 2015, to understand their ability in explaining the variability of crop production, months in advance, and thus helping to forecast potential critical situations, such as the drought that hit India in early summer 2019.

A preliminary and rigorous screening process was carried out to 1) exclude non-cultivated areas from index calculations, 2) select meaningful time scales for making comparisons between the different indices (SPI-3 best represented agricultural drought among other SPIs and most closely related to SSI-1, calculated both with ESA CCI and MERRA-2) and 3) find the months when crop production was most sensitive to SSI/SPI indices. For maize these months were July, August and September (monsoon period), whereas for wheat the months of October and November were most sensitive (correlating with the emergence stage of wheat growth).

After this screening process, the relation between the indices and crop-yield data was explored, as a function of crop type, type of variable (rainfall versus soil moisture), method used to estimate soil moisture (satellite versus model), drought severity (drought vs. non-drought conditions) and the influence of the human activity (irrigated vs. non-irrigated land).

Our results show that:

1) There are two main limitations to this approach, primarily identified in the correlation analysis at district level: i) the uncertainties associated to satellite soil moisture retrievals over topographically complex and densely vegetated areas; and ii) the reliability of crop-yield data at district level and the relatively short record of crop data. The satellite soil moisture monitoring depth (0-5 cm) showed good performance in our approach, particularly given the selected crops. Indeed, the additional correlation analysis conducted between SSI-1 MERRA2, calculated with

the root zone soil moisture estimates (0-100 cm), and yield anomalies showed a deterioration of the performances compared to SSI-1 MERRA2 SSM. One of the reasons could be related to model limitation; on the other hand, this also highlights that valid information can be obtained from the surface soil moisture observations regarding the growing process of the selected crops.

2) For maize, the overall performance, in terms of linear regression analysis, is comparable among the indices in both drought and non-drought years. The three indices are similarly able to predict crop yield during rainy periods; the precipitation index also seems to better agree with crop yields during these periods. For wheat, an irrigated crop growing during the winter season, soil moisture-based indices outperform SPI-3, suggesting that soil moisture is generally more informative about crop yield when dealing with non-rainfed crops (for which reduction/increments of moisture produce respectively larger decrease/increase of production during drought events as compared to rainfed crops), and should be preferred in agricultural drought analysis.

3) By separating the linear regression analysis in two main classes, i.e., drought conditions vs non-drought conditions, soil moisture was found to be an important limiting factor for crop production during drought years, significantly reducing crop yields as droughts get more severe. Conversely, it plays a minor role during non-drought years, as other factors potentially help increase production.

4) The ESA CCI soil moisture product seems to better represent the soil wetness conditions than the MERRA-2 LSM estimates. While across a few districts at the boundaries of the study area modeled soil moisture shows higher correlations with crop yields than SSI-1 CCI, the linear regression analysis highlights a stronger relation between crop yields and the satellite-based soil moisture index during drought events, as compared to SSI-1 MERRA2. This is particularly true for wheat, growing under irrigated conditions. Here SSI-1 CCI performs better during drought years, as compared to the analysis over the whole croplands, while SSI-1 MERRA2 displays a slight decrease in performance. A similar result, but in the context of flood forecasting, was found by Crow et al. (2017). Further analysis is needed to explore whether this is a limit related to LSM

parameterization – and the fact that models simply simulate or do not include human-related processes like irrigation – or it is case specific.

5) The sensitivity of maize and wheat to low levels of soil moisture was identified to start in July and October, respectively (months used for the annual average of the indices). While crops are inevitably planted before these dates, knowledge of soil moisture levels could be invaluable for farmers for planning irrigation to overcome yield losses.

In conclusion, the results shed some light on the amount of information retained by satellite-based soil moisture observations, in comparison to rainfall and model-based estimates of soil moisture that have largely been used in academic studies to date, given the lack of in-situ soil moisture observations and their limited spatial representativeness (i.e., Farahmand and AghaKouchak, 2015; Sheffield et al., 2004). Understanding this aspect is important for improving the abilities of land surface and numerical weather prediction models in representing and predicting droughts, as the use of satellite soil moisture observations via DA (Drusch, 2007) can potentially provide additional benefits for forecasting systems. This study is also important for understanding the potential role of satellite-based observations for operational drought forecasting, given that new products have become available with higher accuracy and spatial resolution (Bauer-Marschallinger et al., 2018; Das et al., 2010; Piles et al., 2011). Additionally, this analysis provides the foundations for the operational implementation of a crop-forecasting tool, as it can drive developers and scientists in the right direction for selecting the best variables/periods to consider. This aspect is crucial, as it could help farmers, model forecast developers and agricultural managers to better understand, model and allocate water resources for future crop yields. This could help to reduce the risk of crop losses and mitigate migration, especially in developing regions.

Although only one model was used and only part of India was explored, results show that a question exists on whether drought indices built in different ways with different variables are entirely representative of crop-yield reduction, economic losses and famine episodes.

Chapter 3: Optimization of a backscatter forward operator over irrigated land

This chapter describes the analysis and results published in the following journal article:

Modanesi, S., Massari, C., Gruber, A., Lievens, H., Tarpanelli, A., Morbidelli, R., and De Lannoy, G. J. M. ***Optimizing a backscatter forward operator using Sentinel-1 data over irrigated land****, Hydrol. Earth Syst. Sci., 25, 6283–6307, https://doi.org/10.5194/hess-25-6283-2021, 2021.*

This analysis represents the first and necessary step towards building a reliable land surface model (LSM) data assimilation (DA) system which will investigate the potential of high-resolution radar backscatter observations from Sentinel-1 to improve irrigation quantification. Specifically, the Noah-MP LSM running within the NASA Land Information System (LIS) is coupled with a backscatter observation operator for simulating unbiased backscatter predictions over irrigated lands. In this context, it was first tested how well modeled SSM and vegetation estimates, with or without irrigation simulation, are able to capture the signal of aggregated 1-km Sentinel-1 backscatter observations over the Po Valley, an important agricultural area in Northern Italy. Next, Sentinel-1 backscatter observations, together with simulated surface soil moisture (SSM) and leaf area index (LAI), were used to optimize a Water Cloud Model (WCM) which will represent the observation operator in the DA experiments (Chapter 4). The WCM was calibrated with and without an irrigation scheme in Noah-MP, and considering two different cost functions. Chapter 3 is organized as follows: i) Section 3.1 describes data and methodologies used; ii) Section 3.2 presents results obtained; ii) Section 3.3 discusses the results obtained and finally iii) conclusions are drawn in Section 3.4.

3.1 Data and methods

3.1.1 Study area and in situ data

The analysis was carried out over an area of 24,000 km^2 located within the Po Valley, one of the most important agricultural areas in Europe (Figure 3.1, left-bottom corner: 44°N, 10.5°W; top-right corner: 45.5°N, 12.2°W). The Po Valley is part of the Po river basin district (~74,000 km^2), a

mountain-fed catchment which extends from the Alps in the West, to the Adriatic Sea in the East. The Po district is one of the eight districts mentioned in the Water Framework Directive (WFD; EC, 2000) initiated by the European Commission and has been hit by seasonal drought events which impacted all water use sectors, in particular agriculture (Strosser et al., 2012). The water assessment and impact evaluation of human activities over the Po Valley is thus a topic of major interest, considering the significant requirements from the agricultural management sector.

According to the Köppen-Geiger climate classes (Peel et al., 2007) the study area is classified as "Cfa" (temperate climate, without dry season and with hot summers). From a geographical point of view, the Po river flows from the west to the east, splitting the area of interest in northern and southern areas, respectively. North of the Po river, the agricultural plain area can be additionally subdivided into the Veneto region to the east and the Lombardy region to the west (Figure 3.1). Lombardy lands have a high-water availability, thanks to the presence of several Alpine lakes and reservoirs (Musolino et al., 2017), as does the Veneto region. Wine cultivation plays an important role, especially in the Garda Lake surroundings (located to the north-west side of the study area). In the south, the Emilia Romagna region is an agricultural as well as urbanized-industrialized area. Compared to Lombardy and Veneto, Emilia Romagna is much poorer both in water availability and storage capacity, but its irrigation system is considered the most technologically advanced and efficient in the Po river (Musolino et al., 2017). Specifically, it hosts the Canale Emiliano Romagnolo (CER, https://consorziocer.it/it/), one of the most important Italian hydraulic systems for agricultural water supply. The main crops in the study region include general summer and winter crops, orchards (i.e., peach, pear, kiwi), olive groves, and vineyards (https://sites.google.com/drive.arpae.it/servizio-climatico-icolt/home). The plain area is surrounded by a forested hilly and mountainous area of the Tuscan-Emilian Appennine to the south/south-west.

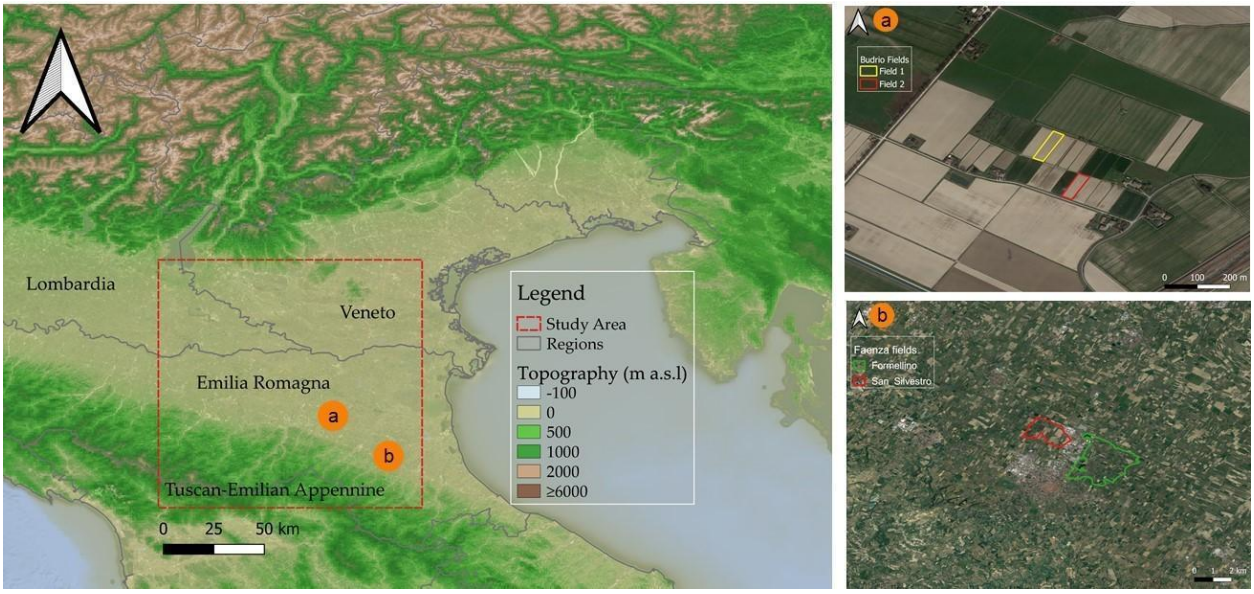

Figure 3.1. The study area and the two test sites of (a) Budrio and (b) Formellino. Data on the topography are obtained from ETOPO1 Arc-Minute Global Relief Model (Amante and Eakins, 2009). Map data ©2015 Google.

In situ data were collected over two test sites, located in the Emilia Romagna region:

- For an analysis at plot scale we selected the Budrio test site (Figure 3.1a), an experimental farm managed by the CER authority which includes two plots of 0.39-0.49 ha. The main crops are maize for field 1 (in yellow) and tomatoes in field 2 (red color). Daily irrigation data, in mm, were collected for the summer 2015-2016 over field 1, whereas daily irrigation water amounts were collected for the summer 2017 over field 2. Additionally, for field 2, hourly in situ soil moisture data, aggregated here at daily scale, were made available from the Department of Physics and Earth Science of the University of Ferrara. The soil moisture data were derived from an innovative Proximal Gamma-Ray (PGR SM hereafter; Filippucci et al., 2020; Strati et al., 2018) station, equipped with a 1L NaI(Tl) detector placed at 2.25 m above the ground and a commercial agro-meteorological station (MeteoSense 2.0, Netsen; Strati et al., 2018).The PGR is a nuclear non-invasive and non-contact technique, which allows to overcome the issue connected to in situ point measurements, probing soil moisture with a field scale footprint (~10^4 m^2) up to a depth of 30 ~ cm. The quantification of PGR soil moisture is derived from measurements of gamma signals emitted by the decay of ^{40}K, which is extremely sensitive to different soil water contents in agricultural soils (for more information on the PGR soil moisture

deriving procedure the reader can refer to Baldoncini et al. (2019). Finally, daily rainfall data were collected from the national rainfall network managed by the Department of Civil and Environmental Protection (DPC) of Italy, for the irrigated periods.

- The second test site (Figure 3.1b) is located around the city of Faenza (hereafter Faenza test site) and has a total extent of 1051 ha, consisting of two fields which allow an analysis at the small-district spatial scale. The first one is called San Silvestro (290 ha) and it is located north of the city. The second one is called Formellino (760 ha), located east to the San Silvestro field and north-east to the city of Faenza. Fruit trees are prevalent on the fields; in particular, pear trees and kiwi dominate the area. The water used for irrigation was provided by CER, at hourly time scale and in mm, for the 2-years time period 2016-2017. Daily rainfall data were collected from the national rainfall network managed by the DPC.

3.1.2 Sentinel-1 backscatter and reference remote sensing products

The Copernicus-ESA Sentinel-1 backscatter observations were used in this study for the calibration of the WCM. The Sentinel-1 constellation consists of two satellites, Sentinel-1A and Sentinel-1B, launched in 2014 and 2016, respectively. Each satellite carries a Synthetic Aperture Radar (SAR) operating at C-band (5.4 GHz) in the microwave (MW) portion of the electromagnetic spectrum. The processing of the ground-range detected (GRD) Interferometric Wide Swath (IW) observations in VV- and VH-polarization was done using Google Earth Engine's Python interface and included standard techniques: precise orbit file application, border noise removal, thermal noise removal, radiometric calibration, and range-Doppler terrain correction. Furthermore, the backscatter observations acquired at 5 × 20 m^2 resolution were aggregated and projected on the 1 km Equal Area Scalable Earth version 2 (EASE-2) grid (Brodzik et al., 2012). After applying an orbit bias-correction (Lievens et al., 2019), the observations (σ^0 hereafter) from different orbits, either from Sentinel-1A or -1B and ascending or descending tracks, were combined at the daily time-scale.

Additionally, EO were used for the evaluation of the SSM and LAI simulated in Noah-MP LSM for the period 31 March 2015 - December 2019:

- The NASA Soil Moisture Active Passive (SMAP; Entekhabi et al., 2010) is an orbiting observatory launched in January 2015 carrying two instruments: a SAR which suffered a failure in early July 2015, and a radiometer measuring Tb at L-band, with a native spatial resolution of 40 km, a revisit time of 2–3 days, and ascending and descending overpasses at 6:00 PM and 6:00 AM (local time), respectively. For this study, the 9-km SMAP Enhanced Level-2 SSM version 4 (0-5 cm; SMAP L2 hereafter) product was used (O'Neill et al., 2020; Chan et al., 2018). The product is derived from SMAP Level-1B (L1B) interpolated antenna temperatures using the Backus-Gilbert optimal interpolation technique. Both ascending and descending tracks were collected.
- The Metop ASCAT SSM Climate Data Records (CDR) H115 and its extension H116 are provided by the European Organization for the Exploitation of Meteorological Satellites (EUMETSAT) Support to Operational Hydrology and Water Management (H SAF; http://hsaf.meteoam.it/, last access 20 May 2021). The SSM is retrieved from backscatter using a change detection algorithm (Wagner et al., 1999), and is characterized by a spatial sampling of 12.5 km and a temporal resolution of one to two observations per day, depending on the latitude.
- The PROBA-V LAI is derived from the PROBA-V satellite mission (Dierckx et al., 2014; Francois et al., 2014) and provided by the Copernicus Global Land Service program (CGLS, https://land.copernicus.eu/global/). The CGLS product at 1 km spatial resolution and 10-day (dekadal) temporal resolution is developed based on the work by Verger et al. (2014).

In order to compare Noah-MP simulations and reference data at the same spatial resolution, Sentinel-1 observations (σ^0-VV and -VH), as well as ASCAT SSM, SMAP L2 SSM and PROBA-V LAI were extracted over the study domain (left-bottom corner: 44°N, 10.5°W; top-right corner: 45.5°N, 12.2°W) and re-gridded over the LIS grid domain (0.01°) using the nearest-neighbor approach.

3.1.3 Land surface and irrigation modeling

3.1.3.1 Noah-MP v.3.6

The analysis was carried out using the Noah-MP (Niu et al., 2011) LSM, running within NASA's LIS 7.2 version (Kumar et al., 2008). LIS is a software framework for terrestrial hydrology modeling and DA, which supports different LSMs that can be conditioned on multiple remote sensing products from active and/or passive MW sensors. The Noah-MP LSM, which was chosen for this study, is an evolution of the baseline Noah LSM (Chen et al., 1996; Chen and Dudhia, 2001; Mahrt and Pan, 1984) wherein main improvements and augmentations are: 1) the presence of four soil layers; 2) up to three snow layers; 3) one canopy layer which allows to dynamically simulate the vegetation and to compute separately the ground surface temperature; 4) a two-stream radiation transfer scheme based on the canopy layer sub-grid scheme; 5) a Ball-Berry type stomatal resistance scheme; 6) and finally, a simple groundwater model with a TOPMODEL-based runoff scheme (Niu et al., 2007, 2005). The model was set up selecting four soil layers at depths 0–10, 10–40, 40–100 and 100–200 cm, a dynamic vegetation model with a Ball-Berry type canopy stomatal resistance model (Ball et al., 1987), and TOPMODEL-based runoff.

The parameterization followed the recommended options provided in the LIS documentation (https://modelingguru.nasa.gov/docs/DOC-2634). A model time step of 15 minutes and a 6 hours output interval were selected together with a spatial resolution of 0.01°. The meteorological forcings used for running Noah-MP LSM were obtained from MERRA-2 (Gelaro et al., 2017). The MERRA-2 original spatial resolution of 0.5°x0.625° was re-mapped to 0.01° through bilinear interpolation. Land model data and parameters were pre-processed and adapted to the LIS longitude/latitude projection using the Land Surface Data Toolkit (LDT; Arsenault et al., 2018) in order to run Noah-MP at the chosen spatial resolution.

For this activity, the default LIS Land Cover (LC) map from the University of Maryland (UMD) global land cover product (Hansen et al., 2000) based on the Advanced Very High Resolution Radiometer (AVHRR) data was replaced with the 2015 global LC map, available from the CGLS at 100 m spatial resolution (Buchhorn et al., 2020; available at https://land.copernicus.eu/global/products/lc). The CGLS provides Dynamic Land Cover Layers

at 100 m spatial resolution (CGLS-LC100), obtained by combining information derived from the vegetation instrument on board the PROBA-V satellite, a database of high-quality LC reference sites, and several ancillary datasets. For a more detailed explanation of the LC maps generation process we refer to the Algorithm Theoretical Basis Document (ATBD; Buchhorn et al., 2020). The 23 classes of the PROBA-V LC map were reclassified to the 14 classes used in the UMD-AVHRR classification supported by LIS. Additionally, the LC map was regridded at 0.01° (Figure 3.2a) by identifying the most representative class over each LIS grid cell.

Similarly, the default FAO Soil Map (FAO Soil Map of the World, 1971) was replaced by the Harmonized Soil World Database (HWSD v1.21, 1 km; Figure 3.2b) and mapped to 5 soil classes over the study region. Other model pre-processed parameters inputs were: i) the Shuttle Radar Topography Mission elevation data (SRTM30, 30 m spatial resolution); 2) climatological global Greenness Vegetation Fraction (GVF) data (0.144°; Gutman and Ignatov, 1998) derived from 5 years (1985-1989) of normalized difference vegetation index (NDVI) data from the AVHRR (Miller et al., 2006); 3) a snow-free albedo and a Noah-specific maximum snow albedo product from NCEP (original resolution 1° and regridded); and finally, 4) soil, vegetation, and other general parameter tables for Noah-MP from the LIS official Data Portal (https://portal.nccs.nasa.gov/lisdata_pub/data/).

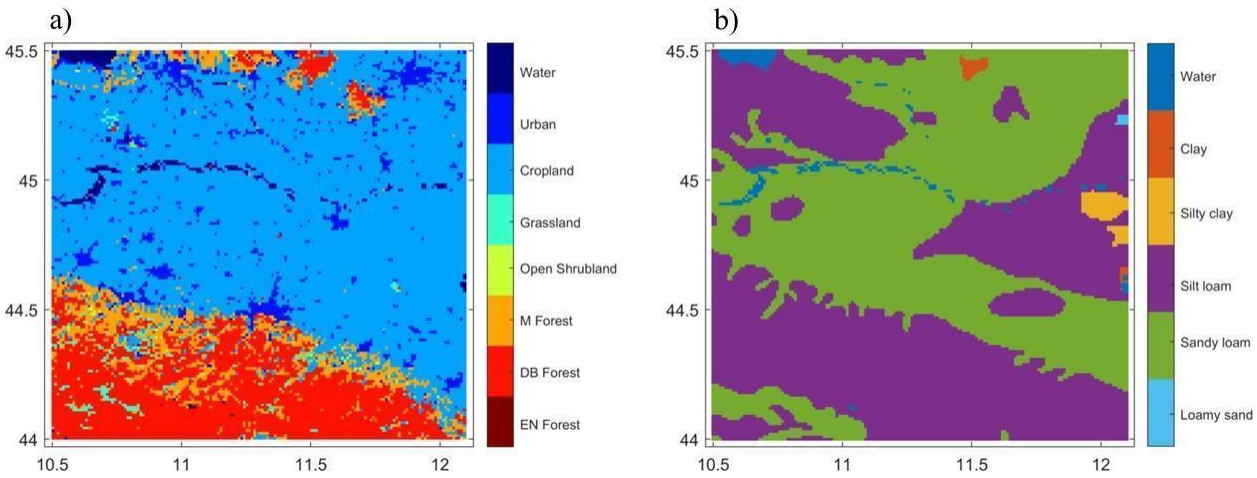

Figure 3.2. Re-gridded and reclassified input data used in the LIS framework: a) the PROBA-V LC map; and b) the HWSD soil texture map. In each plot, the x- and y-axes represent longitudes and latitudes in degrees east and north, respectively.

3.1.3.2 Irrigation modeling

The ability of Noah-MP to dynamically simulate the vegetation and the option to activate irrigation are particularly important considering an extensively irrigated area such as the Po Valley. Indeed, in a recent study by Nie et al. (2018), Noah-MP was coupled with a sprinkler irrigation scheme (where irrigation is applied as supplementary rainfall; Ozdogan et al., 2010a), which requires three pieces of information:

- the irrigation location, only occurring over potentially irrigated croplands (expanding over grassland if the intensity exceeds the grid cell's total crop fraction). This information is extracted from a LC map associated with an additional dataset providing information on the percent of irrigated area per grid cell. In this study, the reclassified PROBA-V LC map was coupled with the information contained in the 500 m Global Rain-fed, Irrigated and Paddy Croplands data set (GRIPC; Salmon et al., 2015);
- the timing of irrigation, which is determined by checking the start and end of the growing season based on a GVF threshold, separately at each grid cell. Following Ozdogan et al., (2010a), we set this threshold to 40% of the GVF;
- the amount of water used for irrigation. This quantity is derived from the root zone soil moisture (RZSM) availability (MA) as $MA=(RZSM-SM_{WP})/(SM_{FC}-SM_{WP})$ where RZSM is the current RZSM, SM_{WP} is the soil moisture wilting point, and SM_{FC} is the soil moisture field capacity. When the MA falls below a user-defined threshold, irrigation is triggered and the quantity is defined by calculating the amount of irrigation needed to raise the RZSM to the SM_{FC}. For this study, the MA threshold was defined as the 50% of SM_{FC} as in Ozdogan et al. (2010a). MA is calculated at each time step but the irrigation is only applied between 06:00 and 10:00 local time. Following Ozdogan et al. (2010a), this time frame is typically chosen by farmers to reduce evaporative losses. In this context, the maximum rooting depth becomes a crucial information to compute the amount of irrigation water. This information is related to an assigned crop type, cultivated over the study area, through a maximum rooting depth table. Considering the high crop variability over the Po Valley as well as the lack of high resolution dynamic crop maps for the entire study area, a generic crop type with 1 m root

depth was selected for the irrigation simulations. The reference rooting depth was verified to be feasible over the study area based on the European Soil Data Center (ESDAC, available at https://esdac.jrc.ec.europa.eu/content/european-soil-database-derived-data) rooting depths map (Figure 3.3).

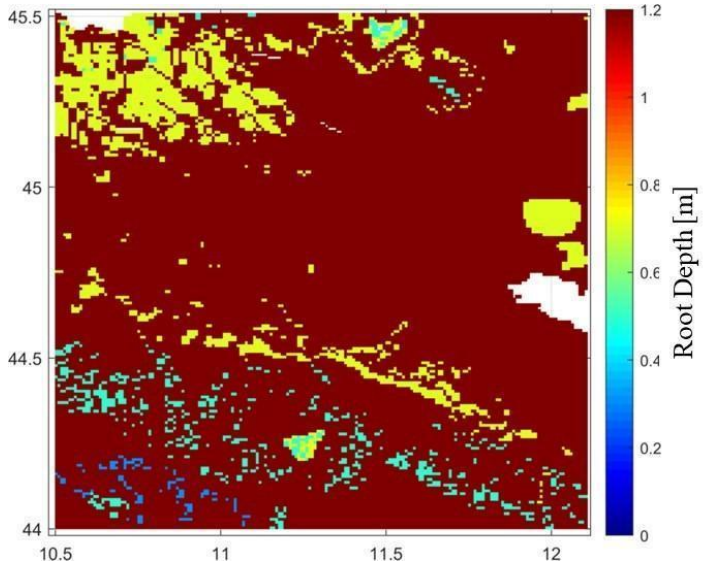

Figure 3.3. 1-km ESDAC root depth data; available at https://esdac.jrc.ec.europa.eu/content/european-soil-database-derived-data. The x- and y-axes represent longitudes and latitudes in degrees east and north, respectively.

3.1.4 Water Cloud Model

The WCM allows to simulate the top-of-vegetation σ^0 as a function of SSM and vegetation, using empirical fitting parameters. σ^0 is modeled as the sum of the backscatter from the vegetation (σ^0_{veg}, in dB) and from the bare soil (σ^0_{soil}, in dB), attenuated by the t^2 coefficient that describes the two-way attenuation from the vegetation layer. Scattering interactions between the ground and the vegetation are not accounted for. As reported in Baghdadi et al. (2017), for a given polarization pq (i.e., VV and VH), the WCM can be written as follows:

$$\sigma^0_{pq} = \sigma^0_{veg,pq} + t^2_{pq}\sigma^0_{soil,pq} \quad (3.1)$$

where:

$$\sigma^0_{veg,pq} = A_{pq}V_1 cos\theta(1 - t^2_{pq}) \quad (3.2)$$

$$t^2_{pq} = exp(\frac{-2B_{pq}V_2}{cos\theta}) \quad (3.3)$$

$$\sigma^0_{soil,pq} = C_{pq} + D_{pq} \cdot SSM \quad (3.4)$$

Equations 3.2 and 3.3 describe the vegetation-related terms. V_1 and V_2 represent two bulk vegetation descriptors, the first one accounting for the direct vegetation σ^0, and the second one representing the attenuation. A_{pq}[-] and B_{pq}[-] are the two related fitting parameters. Common vegetation descriptors used in previous studies are the Vegetation Water Content (VWC, Paloscia et al., 2013), the NDVI (El Hajj et al., 2016; Li and Wang, 2018) and LAI (Bai and He, 2015; K. Kumar et al., 2015), while θ represents the incidence angle, which is assumed to be 37° for Sentinel-1. Following previous studies (see Baghdadi et al., 2017; Li and Wang, 2018; Lievens et al., 2017a) we assumed V_1=V_2 represented by the dynamically simulated LAI vegetation descriptor.

Equation 3.4 describes the soil-related term. Following the work by Lievens et al. (2017a) the σ^0_{soil} can be described, in a simple linear approach, as a function of the SSM. There are several semi-empirical models (e.g., the Oh model; Oh et al., 1992) or theoretical models (e.g., the Integral Equation Model (IEM), Fung, 1994) which describe the scattering processes related to the bare soil, but their application as a forward operator coupled to a LSM has two main limitations: the first one lies in the difficulty in retrieving soil roughness values over extended reference areas required to parameterize these models; the second one is their saturation of σ^0 in moist conditions which causes low variability in simulated σ^0 if the LSM soil moisture simulations are biased wet (for more information see Lievens et al., 2017a). Those limitations justify the use of a linear fitted approach. In Equation 3.4, the C and D parameters (here fitted in dB and dB/m^3/m^3, respectively, but σ^0_{soil} is transformed back to the linear scale in Equation 3.1) describe the linear relation between $\sigma^0_{soil,pq}$ and SSM. Those parameters, as well as A(-) and B (-), need to be calibrated separately for each polarization.

3.1.5 Calibration algorithms

Two different objective functions were considered to optimize the A, B, C and D parameters:

- a Bayesian solution, which minimizes the Sum of Squared Errors (SSE) between σ^0 observations from Sentinel-1 and WCM simulations. The SSE Bayesian calibration solution aims at identifying the optimal parameter vector $\boldsymbol{\alpha}$ which maximizes the probability of the resulting σ^0 simulations $p(\hat{y}^-) = p(\hat{y}^-|\alpha)p(\alpha)$, where $p(\alpha)$ is the prior

parameter distribution and $p(\hat{y}^-|\alpha)$ is the likelihood. Starting from the assumption of an independent and identically distributed normal error model, the posterior probability can be maximized by maximizing:

$$p(\hat{y}^-|\alpha)p(\alpha) = \prod_i^{N_i}\left\{\frac{1}{s_i\sqrt{2\pi}}exp\left(-\frac{(\hat{y}-\hat{y}^-)_i^2}{2s_i^2}\right)\right\}\cdot\prod_j^{N_\alpha}\left\{\frac{1}{s_j\sqrt{2\pi}}exp\left(-\frac{(\alpha_0-\alpha)_j^2}{2s_j^2}\right)\right\} \quad (3.5)$$

i.e., the combination of the likelihood and a prior parameter constraint. The latter helps in reducing problems of equifinality. In Equation (3.5), $\hat{y}$ represents the observed σ^0, $\hat{y}^-$is the simulated σ^0, i is the timestep and s_i is the standard deviation of the residual differences between the observed and simulated σ^0 values for N_i time steps. N_α is the number of parameters to be calibrated, α_0 is the prior parameter constraint and the parameter deviation is limited by s_j^2, the variance of a uniform distribution $s_j^2 = \left(\alpha_{max,j} - \alpha_{min,j}\right)^2/12$ with determined boundaries of the parameters $[\alpha_{min},\alpha_{max}]$. The maximum likelihood solution is found by minimizing the following cost function J:

$$J = \sum_i^{N_i}\left\{ln(s_i) + \frac{(\hat{y}-\hat{y}^-)_i^2}{2s_i^2}\right\} + \sum_j^{N_\alpha}\left\{\frac{(\alpha_0-\alpha)_j^2}{2s_j^2}\right\} = J_0 + J_\alpha \quad (3.6)$$

where s_i is assumed to be constant in time and represented by a target accuracy of 1 dB, leaving the SSE in the first term of J_0 to minimize. The second term (J_α) constrains the optimal solution by avoiding strong deviations from initial parameter guesses.

- a solution that maximizes the Kling-Gupta Efficiency (KGE; Gupta et al., 2009). Even though this objective function does not ensure Bayesian optimality, it is a widely used metric which could help to better tune the dynamic σ^0 behavior:

$$KGE = 1 - \sqrt{(r-1)^2 + \left(\frac{<\hat{y}^->}{<\hat{y}>} - 1\right)^2 + \left(\frac{s[\hat{y}^-]/<\hat{y}^->}{s[\hat{y}]/<\hat{y}>} - 1\right)^2} \quad (3.7)$$

The *KGE* formulation embeds three terms: 1) the first term accounting for the Pearson Correlation (Pearson-R) between the observed ($\hat{y}$) and simulated ($\hat{y}^-$) σ^0 time series; 2) a second term accounting for the bias, where the long-term mean is represented as <.>; and finally, 3) a term accounting for the variability of the simulated and observed signal

through the use of the standard deviation s[.]. *KGE* = 1 indicates a perfect agreement between simulations and observations. Note that *KGE* redistributes the weight of the bias, variance and correlation components, compared to *J* in Equation 3.6, which can help in reducing differences between simulated and observed σ^0 also in terms of temporal dynamics during the calibration. On the other hand, in the *KGE* cost function parameters are not constrained by prior values α_0. This could possibly result in overfitting and a larger prediction uncertainty.

The Particle Swarm Optimization (PSO; Kennedy and Eberhart, 1995) was used to minimize *J* and maximize *KGE*. For our case study the PSO parameters were set as in De Lannoy et al. (2013).

3.1.6 Experimental setup

An optimal DA system requires long-term unbiased σ^0 simulations (with respect to the assimilated observations). The risk, over an intensively irrigated area, is that an unmodelled irrigation signal would manifest itself as a predominant bias in the σ^0 simulations. The calibration would then inadvertently correct for this supposed bias (i.e., the irrigation signal), thus preventing the DA system from propagating the missing irrigation signal from the observations into the model. Even though existing irrigation schemes are evidently unrealistic and inaccurate, it was conjectured that using such a scheme when calibrating the WCM will more likely yield optimal WCM parameters than when neglecting irrigation.

To that end, two different experiment lines were considered (referred to as *Natural* and *Irrigation*, respectively) that produced a total of eight different σ^0 simulation runs (see Figure 3.4). The *Natural* experiment line differs from the *Irrigation* line by the activation of an irrigation module in Noah-MP, and both are subjected to the calibration algorithms described in Section 3.1.5. The *Natural* line was used as a diagnostic experiment against which to compare *Irrigation*, which, according to our initial hypothesis, should minimize the impact of the irrigation signal contained in the σ^0 observations on WCM parameters.

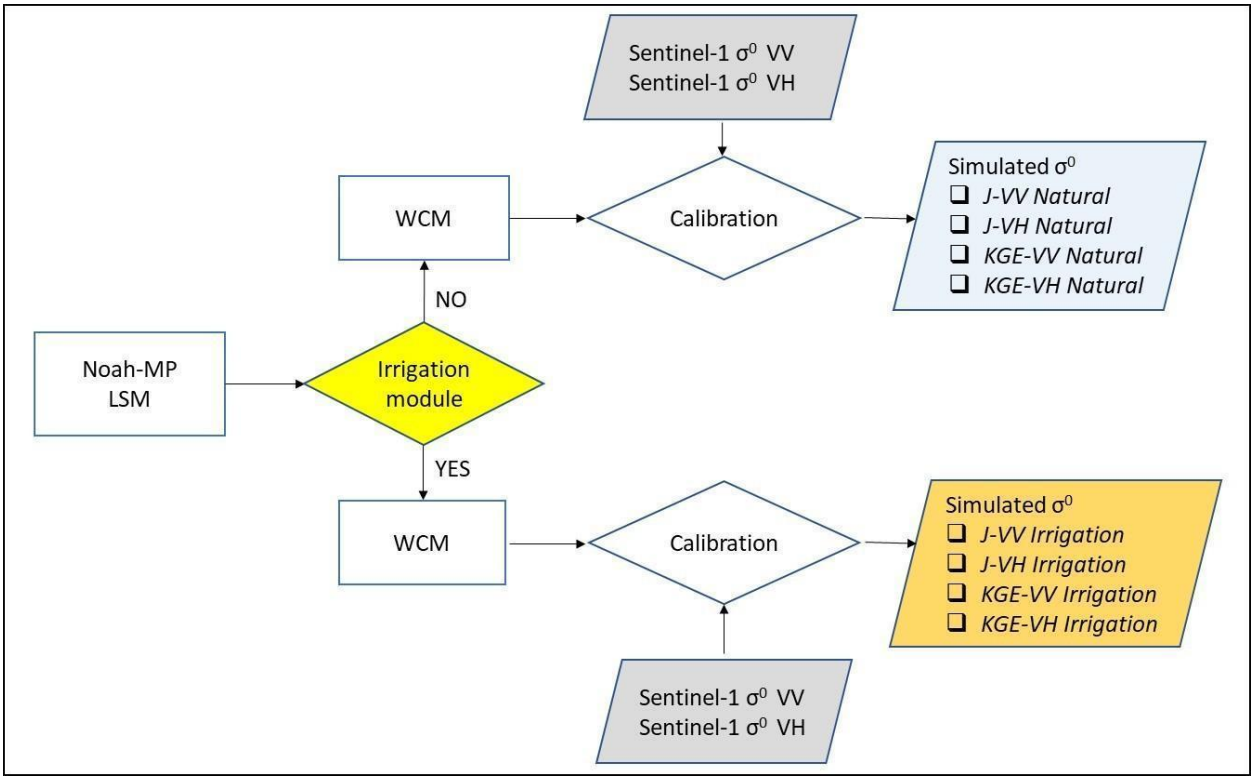

Figure 3.4. Flow chart of the experimental setup used in this study to calibrate the WCM σ^0 signal. A *Natural* and an *Irrigation* experimental line was performed coupling either Noah-MP *Natural* or *Irrigation* simulations with the WCM. For each experimental line σ^0 simulations are driven by the Sentinel-1 signal using two different cost functions (*J* and *KGE*) in order to provide eight different calibration experiments.

As a first step, a model spin up was performed, starting in January 1982 and ending in December 2014. Then, a study period from January 2015 to December 2019 was selected for the different model runs based on the availability of the processed Sentinel-1 σ^0 and reference irrigation data (see Sections 3.1.1 and 3.1.2). Daily surface model and irrigation outputs were produced. Considering that the main source of irrigation in the Po Valley is related to surface water abstraction, the sprinkler irrigation scheme did not account for groundwater withdrawals (see Nie et al., 2018).

The A, B, C, and D parameters of the WCM (see section 3.1.4) were fitted separately to Sentinel-1 σ^0 VV and VH observations, during the period January 2017 - December 2019. Following previous literature (De Lannoy et al., 2014, 2013; Lievens et al., 2017a), we performed a grid cell-based calibration to account for the spatial variability in the simulated and observed σ^0 signals that stems from specific features within the observed footprints as well as from the soil and vegetation

parameterization of Noah-MP. Both the calibration using the SSE with prior constraint (Bayesian *J*) and the *KGE* were applied to the *Natural* and *Irrigation* runs providing eight different experiments named *J-VV Natural*, *J-VH Natural*, *J-VV Irrigation*, *J-VH Irrigation*, *KGE-VV Natural*, *KGE-VH Natural*, *KGE-VV Irrigation* and *KGE-VH Irrigation.*

Lower and upper boundaries as well as prior guess values of the WCM parameters were defined based on the work of Lievens et al. (2017a) and on a sensitivity analysis (not shown here). The selected values are displayed in Table 3.1. Finally, it should be noted that all the calibration experiments were realized by considering daily values of σ^0 simulations and observations.

Table 3.1. Lower boundaries (LB), upper boundaries (UB), and prior guess values of the WCM parameters for both VV and VH polarization

	A-VV [-]	A-VH [-]	B-VV [-]	B-VH [-]	C-VV [dB]	C-VH [dB]	D-VV [dB/m^3/m^3]	D-VH [dB/m^3/m^3]
UB	0.4	0.4	0.4	0.4	-10	-10	80	80
LB	0	0	0	0	-35	-35	15	15
GUESS	0	0	0	0	-20	-30	40	40

3.1.7 Noah-MP LSM and WCM evaluations

The validation aims at i) evaluating the performance of Noah-MP in simulating irrigation, soil moisture, and vegetation and the ability of the WCM to simulate radar σ^0, and ii) unveiling the information about irrigation contained in Sentinel-1 radar σ^0 in order to assess its potential to improve both soil moisture and vegetation representation within Noah-MP.

The evaluation was carried out on both the regional scale (i.e., over the entire study area) and on the two selected sites, Faenza (small-district scale) and Budrio (plot scale), where irrigation data were available. Considering the lack of benchmark data for irrigation evaluation (Foster et al., 2020) we decided to use in situ data for the small Budrio fields spatial scale (i.e., 0.45-049 ha) even though model simulations are made at a much coarser resolution (i.e., ~1 km). We are aware that differences in spatial scale can increase the uncertainty of our evaluation, but 0.01° LSM spatial resolution is still a good compromise for an analysis at regional, small-district and plot scale.

Additionally, limitations are partly reduced by the low chance of including non-irrigated fields within the 1 km LIS grid cells within the Po Valley, as the latter is almost entirely irrigated (Salmon et al., 2015). Noah-MP (with and without using the irrigation module) SSM and LAI simulations were compared with satellite SSM from ASCAT and SMAP, and LAI from PROBA-V, respectively, during the period 2015-2019. Furthermore, these land surface simulations were compared to Sentinel-1 σ^0 to understand how much of the SSM and LAI signal was captured by Sentinel-1.

As the irrigation timing is often driven by the stakeholders' turns to withdraw water and by water availability rather than by the conditions of the soil and crops themselves, the comparisons between simulated SSM and satellite SSM were carried out by aggregating the two variables over a bi-weekly time window. On the other hand, the LAI from Noah-MP was aggregated to 10-days values in order to match the 10-days PROBA-V LAI values. We used the Pearson-R for SSM and LAI evaluation. For SSM, we also computed the Root Mean Square Error (RMSE), calculated considering the original temporal resolution of the satellite products, while for LAI, we also tested the ratio bias, i.e., the ratio between the long-term mean of the simulations and the long-term mean of observations. In particular, this additional score for LAI was used to provide a further evaluation of the ability of the Noah-MP to simulate crop phenology during the irrigated vs non-irrigated periods so as to not rely solely on the evaluation of temporal dynamics, which, due to the uncertainty in the Noah-MP crop type parameterization, could be affected by time shifts in the LAI climatology. This parameterization uncertainty comes from the lack of knowledge of the spatial crop type information and is difficult to be reduced without additional information. Our assumption is that radar σ^0 assimilation can also correct for this with future DA.

Following Vreugdenhil et al. (2018) and Vreugdenhil et al. (2020), Noah-MP LAI and PROBA-V LAI were also compared with the Sentinel-1 σ^0 VH/σ^0 VV cross ratio (CR), which was demonstrated to have a high agreement with the vegetation signal. Though the σ^0 VH was demonstrated to increase with the vegetation signal (Macelloni et al., 2001), the CR will be more sensitive to vegetation changes as the ratio is less sensitive to changes in soil moisture and soil-vegetation interaction (Veloso et al., 2017; Vreugdenhil et al., 2020).

To evaluate WCM simulations, we used bi-weekly values of σ^0 simulations and observations considering a two-years period independent from the calibration period: 2015-2016. Statistical metrics such as grid-based temporal Pearson-R, KGE, and bias were calculated between Sentinel-1 σ^0 and calibrated WCM simulations. The analysis of the parameters was restricted to the cropland area as no difference between our experiment lines exists over other land cover types (i.e., the irrigation module is active only over grid points classified as crop).

3.2 Results

3.2.1 Noah-MP regional evaluation

Figure 3.5 shows maps of the Pearson-R between bi-weekly Noah-MP SSM *Natural* and *Irrigation* simulations and bi-weekly ASCAT and SMAP L2 SSM retrievals, respectively, for April 2015 to December 2019. The Noah-MP SSM *Irrigation* run provides a higher agreement with both satellite SSM data sets compared to the *Natural* run. Indeed, the median Pearson-R between SMAP L2 SSM and Noah-MP SSM increases from 0.68 to 0.73, for the *Natural* run (Figure 3.5a) and the *Irrigation* run (Figure 3.5b), respectively. A similar improvement can be observed considering the ASCAT reference SSM, with an improvement in the median Pearson-R of 0.08 when irrigation is activated in the model (from 0.7 to 0.78; Figure 3.5e). Areas characterized by higher correlation when irrigation is simulated are represented in blue in the Pearson-R difference map of Figure 3.5f (obtained by subtracting the map in Figure 3.5d from the map in Figure 3.5e). Almost all cropland areas are characterized by a higher agreement between observations and simulations for the *Irrigation run*. Note that for the evaluation of Noah-MP against SMAP, we relaxed retrieval quality flags, which would otherwise mask out almost the entire study area. Figure 3.6 shows the SMAP coverage when applying all the recommended quality flags.

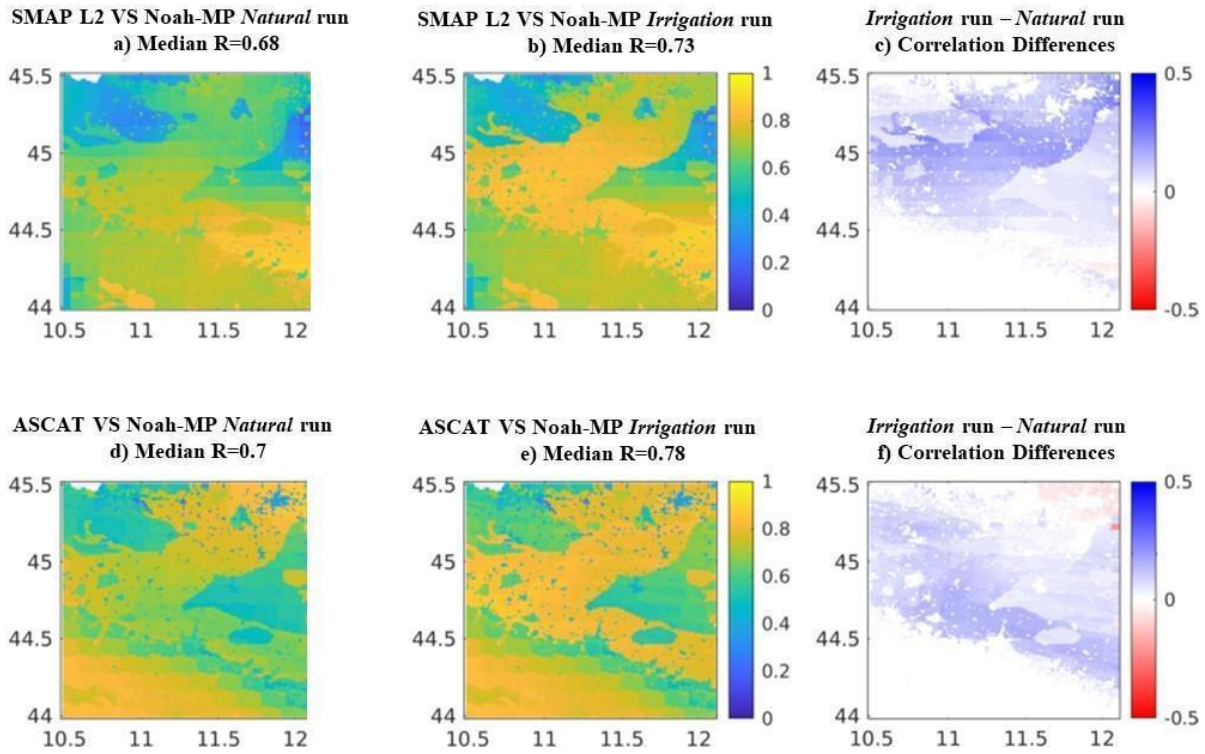

Figure 3.5. Maps of temporal Pearson-R between bi-weekly values of SSM from Noah-MP and satellite retrievals: a) *Natural* run and SMAP L2; b) *Irrigation* run and SMAP L2; d) *Natural* run and ASCAT; e) *Irrigation* run and ASCAT. Maps of the Pearson-R differences display the grid-based difference between: c) map b and map a; f) map e and map d. The reference period is April 2015-December 2019. In each plot, the x- and y-axes represent longitudes and latitudes in degrees east and north, respectively.

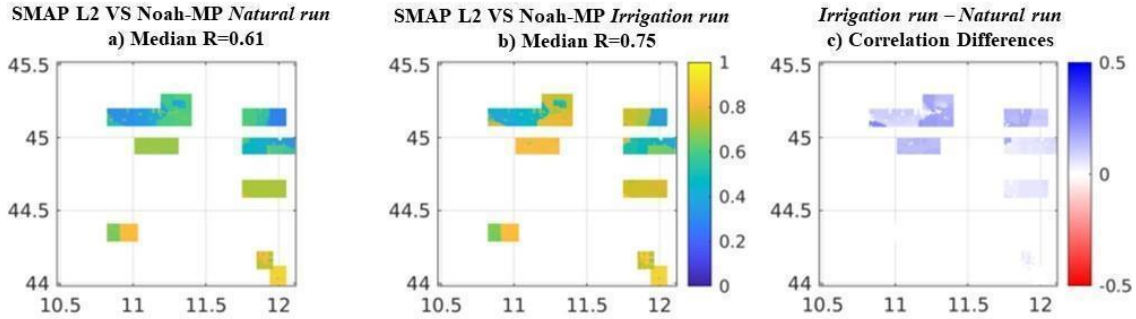

Figure 3.6. Maps of temporal Pearson-R between biweekly values of SSM from Noah-MP: a) *Natural* run and SMAP L2; b) *Irrigation* run and SMAP L2. Map of the Pearson-R differences display the grid-based difference between: c) map b and map a. The maps are obtained applying all the SMAP L2 quality flags. The reference period is April 2015-December 2019. In each plot, the x- and y-axes represent longitudes and latitudes in degrees east and north, respectively.

Results in Figure 3.5 were confirmed by analyzing the RMSE between satellite SSM products and Noah-MP simulations for both the *Natural* and *Irrigation* runs, after rescaling them based on their mean and standard deviation, because SSM retrievals and SSM simulations do not have the same

units. Results are displayed in Figure 3.7 and show, for both the satellite products, a general reduction in RMSE when compared with the *Irrigation* run. An improvement in performances can be observed over the entire cropland area, in particular over the central triangle feature where sandy-loam soil texture is present and where, consequently, more irrigation is simulated in the model due to the higher permeability of the soil.

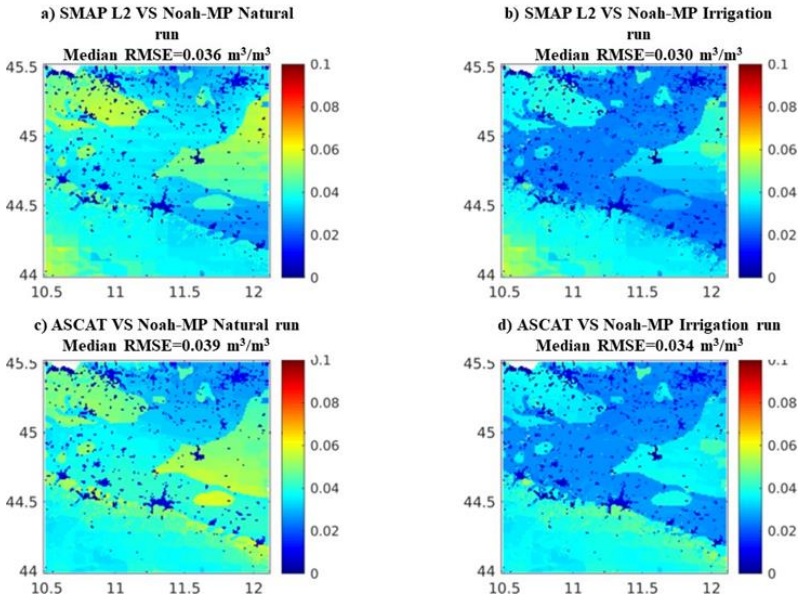

Figure 3.7. Maps of RMSE between SSM from Noah-MP and satellite retrievals: a) Natural run and SMAP L2; b) Irrigation run and SMAP L2; c) Natural run and ASCAT; d) Irrigation run and ASCAT. In each plot, the x- and y-axes represent longitudes and latitudes in degrees east and north, respectively.

The evaluation of the LAI simulation was limited to the regional scale analysis due to a lack of in situ vegetation data over the selected test sites. The comparison between 10-days values of Noah-MP LAI, from both model runs, and the PROBA-V LAI product was carried out over the reference period January 2015 to October 2019 using the temporal Pearson-R and the ratio bias, shown in Figure 3.8.

Figure 3.8a and 3.8b show that the Pearson-R for vegetation has a lower median value of 0.67 when irrigation is simulated in Noah-MP, whereas this value equals 0.72 for the *Natural* run. The difference between the two Pearson-R maps is shown in Figure 3.8c, providing evidence of the areas facing a deterioration of the performance in terms of Pearson-R related to the *Irrigation* run. This deterioration is particularly strong over cropland areas south to the Po river (red color) while the northern area also shows grid cells where the performance improves (blue color).

By contrast, the ratio bias evaluation score (Figures 3.8d, 3.8e, 3.8f) highlights an improvement in long-term mean vegetation simulations when irrigation is included (Figure 3.8e). Here the optimal condition is represented by a ratio bias equal to 1 when the mean of the simulated LAI is equal to the mean of the observed LAI. In this context, Figure 3.8d displays ratio bias values lower than one over a large central triangle-shaped cropland area and median ratio bias value of 0.73, highlighting an underestimation of the LAI simulation related to the *Natural* run. Conversely, Figure 3.8e shows ratio bias values close to one when irrigation is simulated over an extended cropland area and a median bias value of 0.99. The improvement given by the *Irrigation* run is emphasized in Figure 3.8f where the histograms of the ratio bias distributions related to both model runs show the higher performance of the *Irrigation* run (red) compared to the *Natural* run (blue) for which the distribution is more skewed to the zero value.

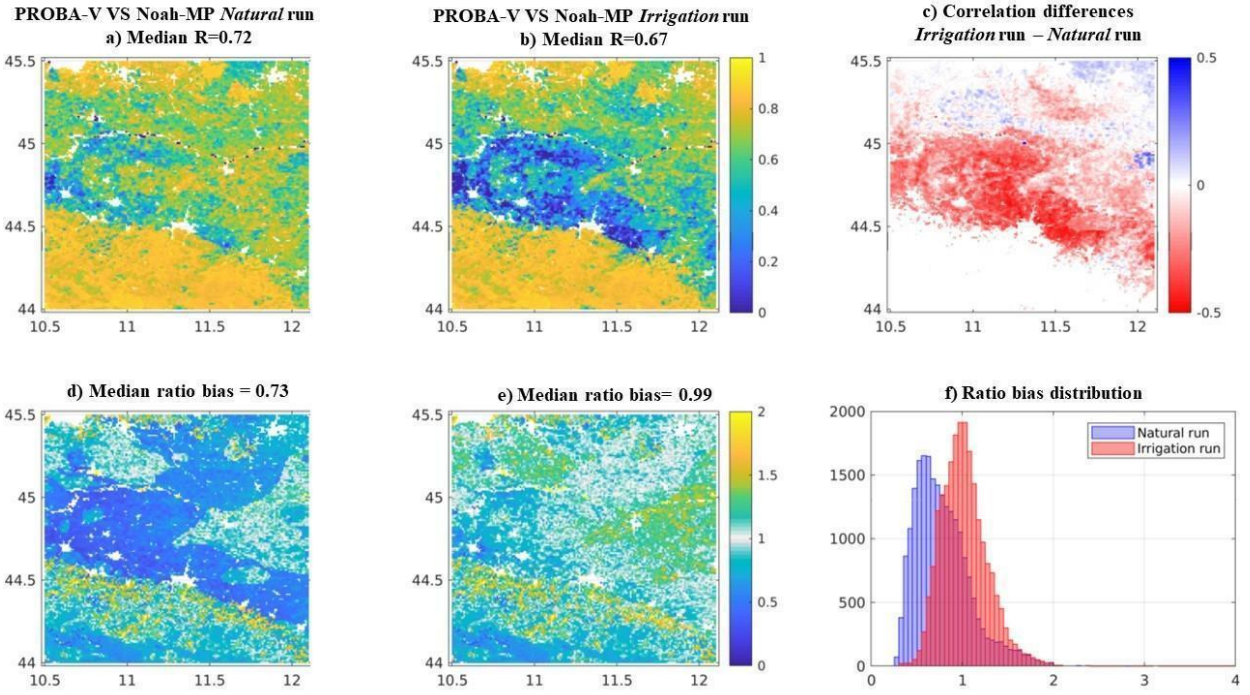

Figure 3.8. Maps of temporal Pearson-R between 10-days LAI values from PROBA-V LAI and Noah-MP LAI: a) *Natural* run; b) *Irrigation* run. Map of Pearson-R differences between: c) map b and map a. Map of ratio bias of LAI from PROBA-V and Noah-MP: d) *Natural* run; e) *Irrigation* run. Additional histogram distributions from: f) map d and map e. The reference period is January 2015-October 2019. In plots a) to e), the x- and y-axes represent longitudes and latitudes in degrees east and north, respectively.

3.2.2 Noah-MP site evaluation

The Noah-MP SSM was evaluated at the Budrio test site field 2 (Figure 3.1a), using the daily reference PGR SM for the year 2017. Comparisons between the SSM simulations of the *Natural* and *Irrigation* runs with in situ PGR SM are shown in Figure 3.9a, while daily observed irrigation and rainfall data are compared with daily irrigation simulations in Figure 3.9b. Soil moisture data are plotted at their original temporal resolution (i.e., daily) to illustrate an issue related to the irrigation timing: SSM simulations in Figure 3.9a show the ability of the sprinkler irrigation scheme to simulate irrigation in the summer season, but there is an inevitable problem in reproducing the correct timing and magnitude of irrigation. Indeed, the total amount of simulated irrigation is 604 mm for the 2017 summer season, which overestimates the total amount of observed irrigation, being 349.5 mm. Furthermore, the model simulations not only miss irrigation, but also suffer from erroneous precipitation input, such as on the 11th of July 2017, where the observed precipitation event in the growing season is not found in the model SSM simulations. In any case, bi-weekly Pearson-R between simulated SSM and in situ PGR SM are higher for the *Irrigation* run than for the *Natural* run (0.54 vs 0.42) suggesting the benefit in activating irrigation.

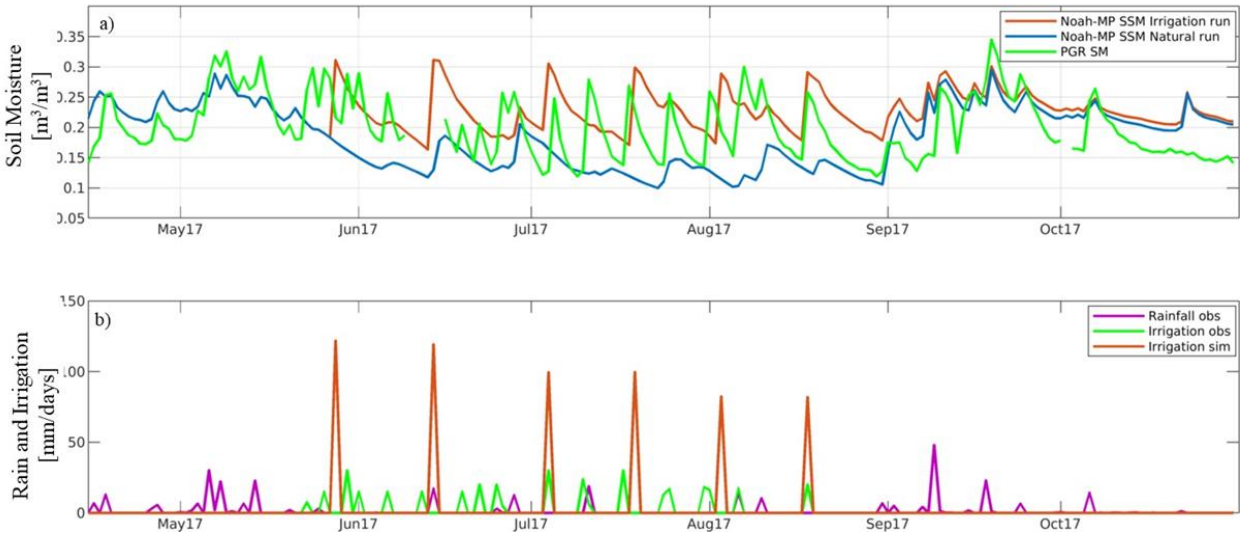

Figure 3.9. Evaluation of SSM over the Budrio field 2, with (green) in situ PGR SM data, (light blue) SSM from Noah-MP *Natural* and (orange) SSM from Noah-MP *Irrigation*. Additional information is provided in the bottom plot: b) observed irrigation (green), simulated irrigation (orange) and observed rainfall (magenta) in mm/day.

For the Budrio field 1 test site (Figure 3.1a), two summer seasons of irrigation data were available. To assess the irrigation information contained in Sentinel-1 σ^0 observations (and the potential added value for a forthcoming DA experiment) we compared bi-weekly values of Sentinel-1 σ^0 VV and VH with SSM estimates from both the *Natural* run and *Irrigation* run (Figure 3.10a) for this site. Although the σ^0 VV is generally used to retrieve SSM (Bauer-Marschallinger et al., 2018; Gruber et al., 2013; Wagner et al., 2013), data at both polarizations were analyzed in order to understand the soil contribution contained in the two signals. Information related to the irrigation periods are shown in Figure 3.10c, where irrigation observations and irrigation simulations from Noah-MP are compared. Figure 3.10a indicates that the SSM simulations are better reflected in the Sentinel-1 σ^0 VV than σ^0 VH data, particularly when irrigation is simulated (orange line). The SSM estimates from the *Natural* run (light blue line) agree poorly with the Sentinel-1 data, with Pearson-R values equal to 0.32 and -0.1 for the σ^0 VV (blue dots) and σ^0 VH (cyan dots), respectively. When irrigation is simulated, the σ^0 VV data better follow the modeled SSM signal (Pearson-R of 0.53) especially during the summer irrigation season when the backscatter signal remains higher and stable. On the other hand, σ^0 VH seems to provide poor performances also when irrigation is simulated, with a Pearson-R value equal to 0.06, confirming findings by Baghdadi et al. (2017) which highlighted how the use of VH alone to retrieve SSM is suboptimal when vegetation cover is well developed.

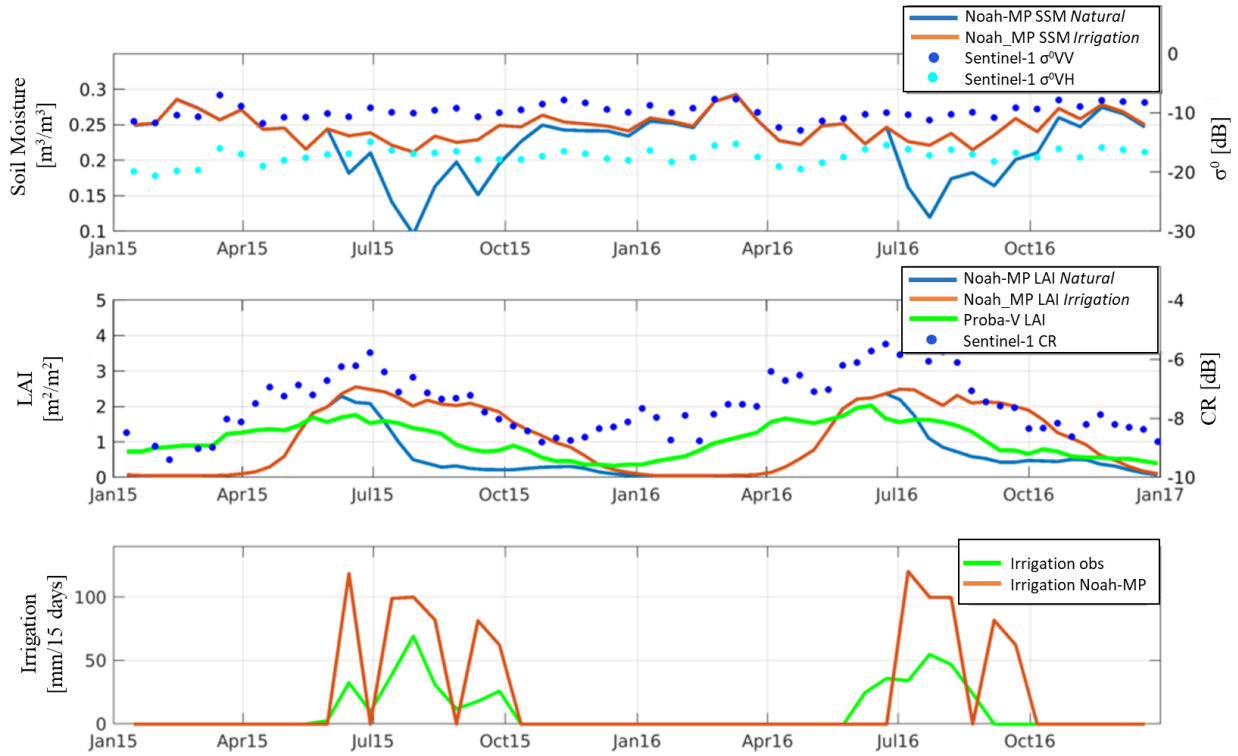

Figure 3.10. Sentinel-1 σ^0 VV and VH data for the Budrio field 1 test site compared with Noah-MP SSM, for a) *Natural* and *Irrigation* runs. Sentinel-1 CR (VH/VV) compared with PROBA-V LAI and Noah-MP LAI for b) *Natural* and *Irrigation* runs. Also shown are: c) observed irrigation (in green) and simulated irrigation from Noah-MP (in orange).

In Figure 3.10b, the Sentinel-1 σ^0 CR (VH/VV) is compared with Noah-MP LAI from the *Natural* run (light-blue line) and *Irrigation* run (orange line). The performance in terms of Pearson-R decreases from 0.76 to 0.65, when the irrigation is simulated. This is due to a time shift of the Noah-MP LAI growing season in the *Irrigation* run. PROBA-V LAI (in green) was additionally compared with the Sentinel-1 CR (blue dots) showing a Pearson-R of 0.84. The higher agreement between EO products (Sentinel-1 and PROBA-V) highlights the strong relation between the σ^0 CR and the vegetation signal, suggesting a potential benefit of Sentinel-1 assimilation to correct the simulated vegetation phenology.

Finally, Figure 3.10c shows a comparison between 15-days accumulated mm of simulated irrigation (in orange) and observed irrigation (in green). The Pearson-R is equal to 0.77, indicating that the sprinkler irrigation scheme can provide acceptable irrigation estimates at this temporal resolution though absolute irrigation amounts are overestimated.

3.2.3 WCM calibration

The WCM parameters A and B (vegetation parameters), and C and D (soil parameters) were calibrated for each grid cell separately during the reference period January 2017 to December 2019 (Figure 3.5), using daily σ^0 simulations and observations. The calibrated parameters related to the entire study area for each of the eight experiments are shown in Figure 3.11 where the blue left parts of the violin plots identify experiments of the *Natural* run, while the orange right parts of the violin plots are related to the *Irrigation* run.

Generally, the *J*-calibration provides parameter distributions closer around their prior guess as compared to the *KGE*-calibration for which the distributions are often multimodal, especially for the C and D parameters (i.e., Figure 3.11d, 3.11h). This is due to the prior parameter penalty, which is included in the Bayesian solution but not in the *KGE*. In general, the calibration of the two functions using the *Natural* run provides wider distributions between lower and upper boundaries for the A vegetation parameter with a high number of grid cells characterized by A-values higher than 0.1 (see *KGE-VV Natural* and *J-VV Natural* experiments in Figures 3.11a and 3.11e respectively). Conversely, the *Irrigation* run provides A distributions more skewed to the lower boundary (being also the guess value in each calibration experiment), with a smaller number of grid cells characterized by high A values compared to the *Natural* run. In a preliminary sensitivity study (not shown), we observed that high values of the vegetation parameters A and B, as obtained for the *Natural* run, have the tendency to generate high peaks in the simulated σ^0 during the growing season. Indeed, in the summer, the SSM *Natural* signal is low and not consistent with the Sentinel-1 σ^0, which observes irrigation. In order to follow the temporal dynamics of the Sentinel-1 σ^0, the calibration algorithms attribute a relatively higher weight (higher A values) to the LAI than to SSM to compensate for the underestimated SSM in the *Natural* run. By contrast, the *Irrigation* run provides vegetation parameter distributions more skewed to the lower boundaries (see also Section 3.2.4.2). The C and D parameter distributions feature a better sensitivity to soil moisture dynamics using the *Irrigation* run input data, which is the expected behavior considering that they describe the σ^0_{soil}. This is true especially when using the *J* cost function (see parameters distributions for the *J-VV Natural* and for the *J-VV Irrigation*

experiments in Figures 3.11g and 3.11h), which results in more spread in the calibrated C and D distributions for the *Irrigation* simulations (especially in VV polarization), whereas the mode of the C and D parameter distributions for the *Natural* experiments is more shifted to the upper and lower boundaries, respectively.

Figure 3.12 shows an example map of the spatial pattern of the parameters over the study area to better understand the differences between the *Natural* and *Irrigation* calibration runs, for the *J-VV* experiments. We found a connection between the WCM parameters distribution and model parameters, in particular with the HWSD soil texture map (shown in Figure 3.2). For both the *J-VV Natural* and *J-VV Irrigation* experiments (Figures 3.12a-h), the activation of the irrigation scheme reduces the dependency of the vegetation-related parameters A and B on soil texture (Figures 3.12a-b for the *J-VV Natural* and Figures 3.12e-f for the *J-VV Irrigation* experiment). This is also shown in the parameter maps of the *KGE* calibration experiments (not shown here). Additionally, the activation of the irrigation scheme, more realistically, shifts the soil texture dependency towards the soil parameters C and D (Figures 3.12g and 3.12h), highlighting another important reason for simulating irrigation.

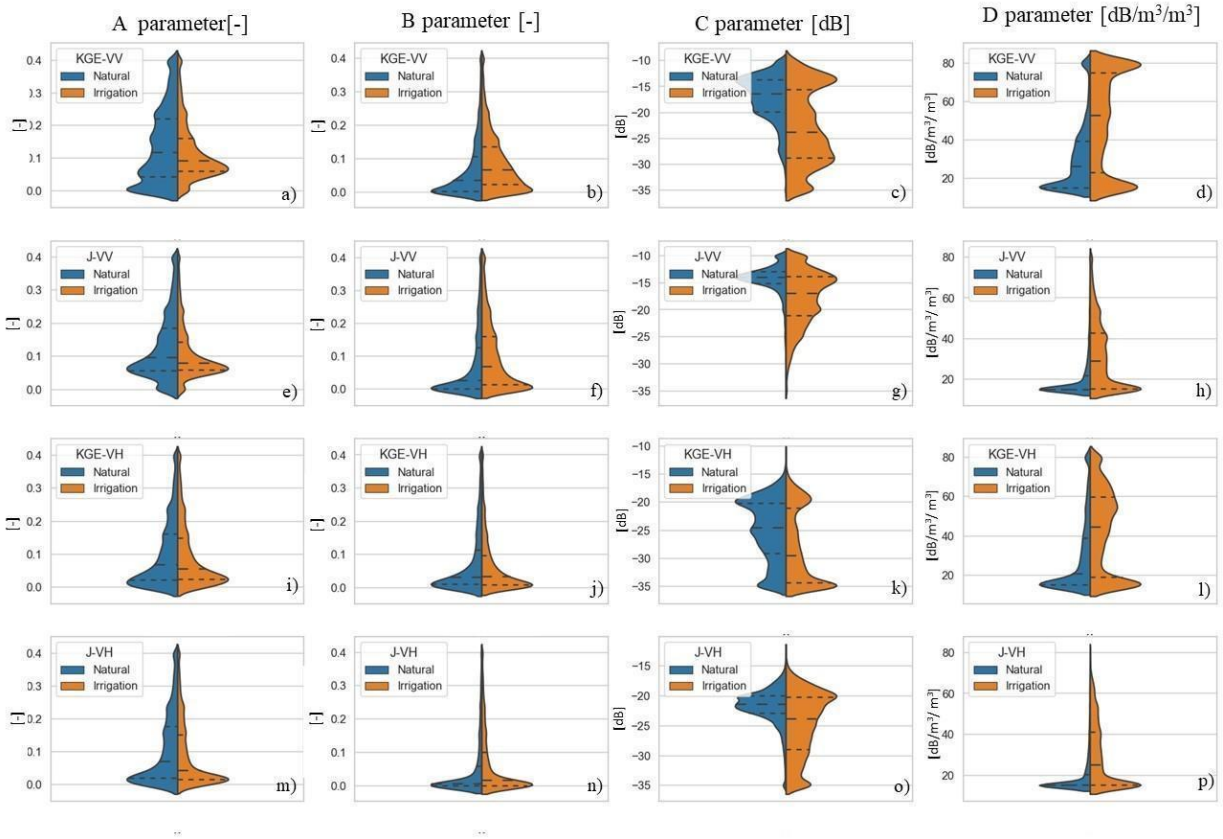

Figure 3.11. Split violin distributions of the calibrated parameters over the entire study area for the eight calibration experiments. For both the Natural (blue) and Irrigation (orange) experiments, the distributions are shown for the A, B, C, and D parameters, (a, b, c, d) using the *KGE* objective function for VV polarization, (e, f, g, h) *J* objective function for VV polarization, (i, j, k, l) *KGE* objective function for VH polarization, and (m, n, o, p) *J* objective function for VH polarization. Note that the areas under the histograms on both left and right sides of the violins are automatically scaled for optimizing the visualization.

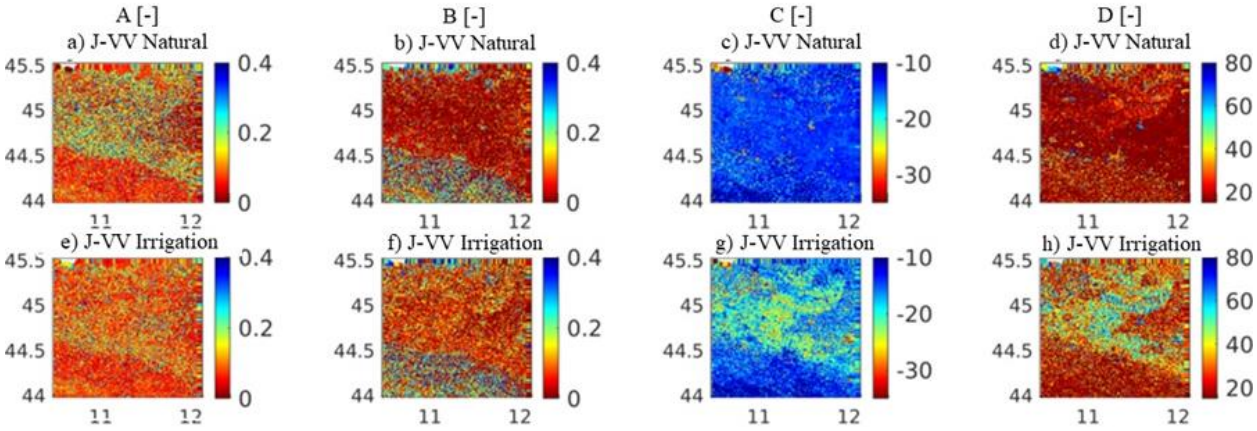

Figure 3.12. Maps of: a) A parameter, b) B parameter, c) C parameter, and d) D parameter for the *J-VV Natural* calibration experiment; e) A parameter; f) B parameter; g) C parameter; and h) D parameter for the *J-VV Irrigation* calibration experiment. In each plot, the x- and y-axes represent longitudes and latitudes in degrees east and north, respectively.

Finally, the different polarization experiments generally provided similar distributions for the vegetation A and B parameters and the D soil parameter. The largest differences between the VV and VH polarizations are identified for the C parameter distributions. This is due to the lower σ^0 signal associated with the VH polarization. Indeed, Figure 3.11c and 3.11g are characterized by higher values of the C in VV polarization, as compared to the distributions for VH polarization in Figures 3.11k and 3.11o. In the latter, the C-VH distributions are generally more skewed to the lower boundary of the parameters, with median values closer to the defined guess parameter value.

3.2.4 WCM evaluation

3.2.4.1 Regional evaluation

The regional evaluation of the calibration experiments was carried out during the period January 2015 to December 2016 for agricultural areas within the study domain (almost 15,000 km^2), by comparing bi-weekly σ^0 simulations with Sentinel-1 σ^0 in terms of Pearson-R, KGE, and bias. The distribution of the evaluation metrics for the eight experiments is shown in Figure 3.13. A comparison of the metrics for the *Irrigation* and *Natural* runs confirms better results when irrigation is activated, with violin plots skewed towards more positive values for both KGE and Pearson-R. When stratified by the cost function, the Pearson-R distribution in Figure 3.13a-d indicates slightly higher performance for the *KGE* (Figures 3.13a and 3.13c) than for *J* (Figure 3.13b and 3.13d). In terms of the KGE score, simulations are naturally closer to the observations when the *KGE* cost function is used. On the other hand, in terms of bias, generally better performances are found when the Bayesian solution is used (Figures 3.13i-l). The latter is particularly evident for the VH polarization when comparing the *KGE-VH* and *J-VH* experiments (Figure 3.13k and 3.13l).

The VH simulations exhibit a better performance in the *Irrigation* run than VV simulations (Figure 3.13c-d and Figure 3.13a-b). Indeed, considering all the statistical scores, the VV polarization is characterized by more similar distributions between the *Natural* and *Irrigation* run for both cost functions. This suggests a higher sensitivity of the VH polarization to the change of vegetation introduced by irrigation, confirming the Sentinel-1 σ^0 VH to be strongly influenced by irrigation

as witnessed by the larger score improvement obtained for the calibration experiments *KGE-VH Irrigation* (Figure 3.13g) and *J-VH Irrigation* (Figure 3.13h), compared to the *Natural* runs experiments.

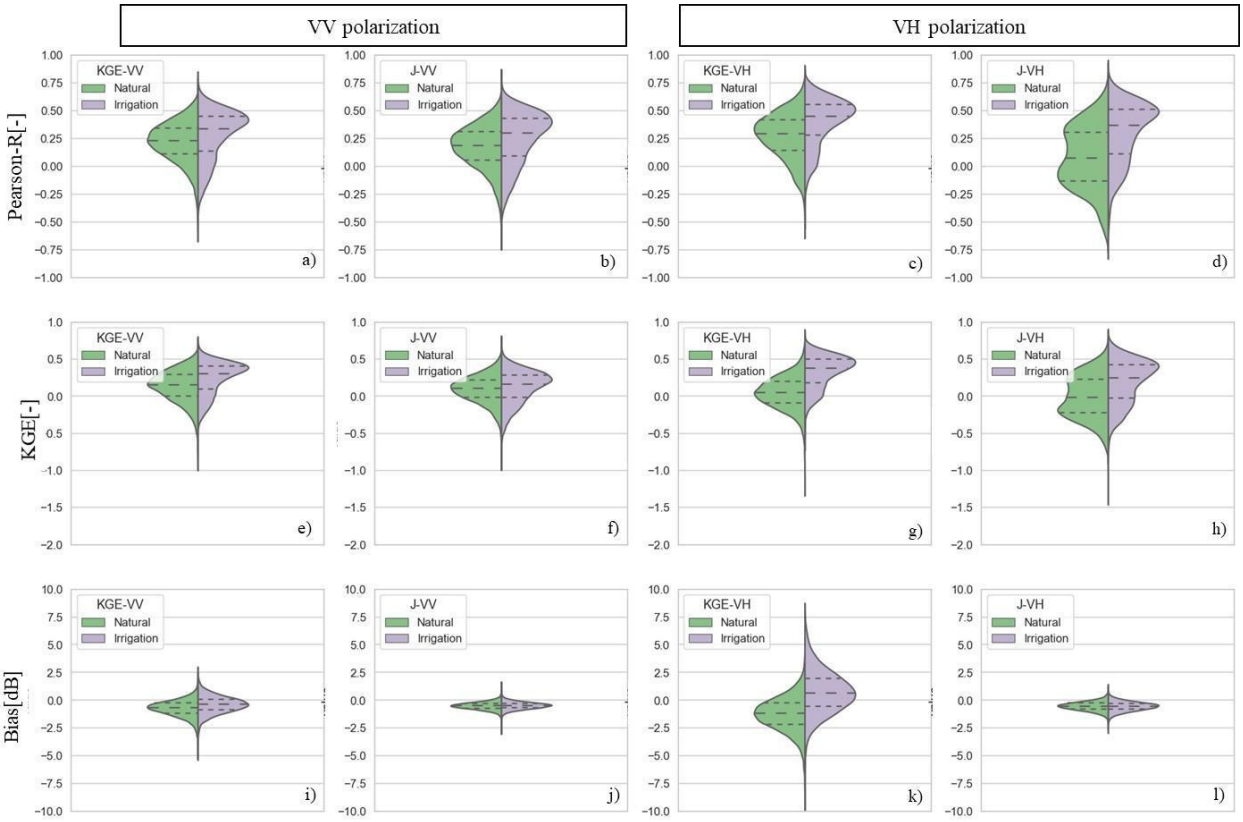

Figure 3.13. Split violin distributions of (a, b, c, d) Pearson-R, (e, f, g, h) KGE and (i, j, k, l) bias calculated between σ^0 simulations and observations for the validation period, for all the calibration experiments and considering only the cropland areas, using simulations from the *Natural* run (left, green) and the *Irrigation* run (right, violet). The results are shown for VV (first two columns) and VH (right two columns), and alternating for both the calibration with a *J* and *KGE* cost function. Note that the areas under the histograms on both left and right sides of the violins are automatically scaled for optimizing the visualization.

In summary, i) VH polarization is more sensitive to the change in the cost function and input data (*Irrigation* or *Natural* run) than VV polarization likely due to its higher sensitivity to vegetation change (Macelloni et al., 2001; Vreugdenhil et al., 2018) which, in the area, is related to the crop development after irrigation, ii) the combination of *J* with activation of the irrigation scheme is able to provide the best unbiased estimates of simulated σ^0 for both VV and VH *(J-VV Irrigation* and *J-VH irrigation* experiments) at the price of generally lower correlations (compared to the *KGE* cost function). This is, however, beneficial for DA as it minimizes the chance of potential error

cross correlation between model estimates and observations. Indeed, the match of the temporal dynamic of the signals induced by the correlation term is stronger in the *KGE* than in *J*, which additionally includes a parameter constraint. The higher weight of the correlation in the *KGE* cost function can negatively impact the parameter calibration even when irrigation is turned on in Noah-MP because the simulated irrigation applications are in general not temporally consistent with those seen by Sentinel-1 (see Figure 3.9). As a general comment, the R and KGE are mainly used as reference scores to understand deterioration or improvements of the calibration when irrigation is simulated. On the other hand, the reduction of bias between observation and simulations is a requested feature for the DA analysis.

3.2.4.2 In situ evaluation

The WCM simulations are further analyzed in detail at the Faenza test site (specifically for the San Silvestro field), because it has a larger extent than the Budrio site (see Figure 3.1), although the same overall conclusions were found for Budrio. Figure 3.14 shows simulated and observed σ^0 time series for the different experiments highlighted in Figure 3.4, and Table 3.2 summarizes the statistics (i.e., Pearson-R, KGE and bias) of each experiment.

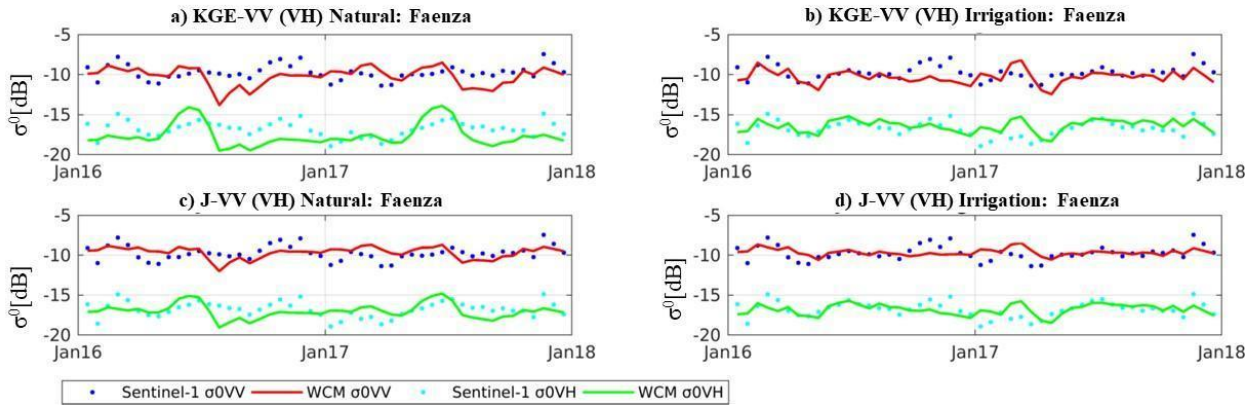

Figure 3.14. Comparisons between σ^0 observations (VV polarization in blue dots and VH polarization light blue dots) and simulations (VV polarization in red and VH polarization in green) in the Faenza San Silvestro field, after calibration with a *KGE* cost function for a) the *Natural* run, b) *Irrigation* run, and after calibration with the *J* cost function for c) the *Natural*, and d) *Irrigation* run.

The agreement between simulated and observed σ^0 measured by the Pearson-R and KGE in Table 3.2 generally gives better performances after calibration with the *KGE* cost function than with the *J* cost function. An example is in the higher correlations found for the *KGE-VH Irrigation*

experiment as compared to the *J-VH Irrigation* (Figures 3.14b and 3.14d respectively). On the other hand, in terms of bias the cost function *J* significantly outperforms the calibration with *KGE* in all experiments with surprisingly comparable values between *Natural* and *Irrigation* runs *(*Table 3.2*)*.

One undesirable feature of *Natural* runs is the presence of high σ^0 peaks during the summer, clearly detectable over the Faenza test site, especially in the VH polarization, which are less evident in the *Irrigation* run *(*see Figure 3.14b and 3.14d). A similar behavior was found for Budrio (not shown). These peaks are likely attributed to the poor estimation of model vegetation parameter values, previously discussed in section 3.2.3, when the WCM attempts to compensate for bias in SSM and vegetation input, i.e., input that is not consistent with observations over irrigated areas. This is particularly true for the *KGE* calibration, which does not use a prior parameter constraint. In contrast, the *J* calibration still provides reasonable σ^0 simulations that are closer to the ones of the *Irrigation* run due to the Bayesian technique itself.

Table 3.2. Results of the site WCM evaluation considering the test site Faenza San Silvestro for each WCM experiment

	KGE-VV Natural	*KGE-VV Irrigation*	*J-VV Natural*	*J-VV Irrigation*	*KGE-VH Natural*	*KGE-VH Irrigation*	*J-VH Natural*	*J-VH Irrigation*
Pearson-R [-]	0.14	0.27	0.14	0.18	0.33	0.41	0.22	0.38
KGE [-]	0.12	0.26	0.12	0.03	0.20	0.38	0.22	0.31
Bias [dB]	-0.46	-0.55	0.07	0.09	-0.82	0.38	-0.22	-0.02

3.3 Discussion

3.3.1 Noah-MP irrigation modeling

The Noah-MP LSM, used as input for the WCM calibration, was evaluated in two configurations, either with a sprinkler irrigation scheme activated or without irrigation (i.e., *Irrigation* run and *Natural* run). Although not all of the Po Valley is irrigated by sprinkler systems, it most likely still leads to more realistic LSM simulations than not considering irrigation at all.

The main limitation found in the irrigation simulations was related to the irrigation timing and magnitude that was inconsistent with observations. Although this finding is based on only a

single study site, it is very likely that it is a widespread issue within the study area for several reasons. In LSMs, the irrigation application is driven by the RZSM availability and consequently by the soil type and the rooting depth parametrizations. Moreover, it is also influenced by the accuracy of the meteorological forcing (especially precipitation) which can determine errors in the soil moisture representation. The main reason, however, is likely that irrigation is often the result of subjective farmer decisions rather than objective rules based on the soil state and crop conditions. In theory, the irrigation timing issue could be partly solved by using temporally consistent high-resolution crop maps which should provide a more realistic information of crop phenology and rooting depth. However, in practice, this is unfeasible over many areas of the world given the absence of this information on a large scale. Also, given that irrigation applications are mainly linked to unmodelled processes like rotation schedules for farmers to withdraw water, the correct simulation of the timing can be unsolvable when using models only.

Despite the potential problems related to the unrealistic assumptions in the simulation of irrigation, results demonstrated that even the use of simple irrigation schemes within Noah-MP can be beneficial. In the regional evaluation, SSM simulations of the *Natural* and *Irrigation* runs were compared with satellite SSM from SMAP and ASCAT (Figure 3.5) on a bi-weekly temporal scale. For both products, large improvements in temporal Pearson-R were found when irrigation was simulated, confirmed by a decrease in the RMSE values over croplands, suggesting that the activation of irrigation modeling provides more realistic SSM estimates. Our findings further confirm the potential of coarse resolution datasets for providing irrigation-related information over intensively irrigated and relatively large agricultural areas, as was shown by S. V. Kumar et al. (2015).

While the impact of irrigation was clear in terms of SSM, the regional evaluation of the simulated LAI against the PROBA-V-based LAI provided contradicting results. In this case, the Pearson-R analysis suggested a deterioration of the Noah-MP simulated LAI when irrigation was activated over the cropland area. This correlation deterioration was interpreted by the absence of specific information about the crop phenology in the model parameterization. In practice, information about the specific crop type is not available and the rooting depth is the sole parameter controlling

water uptake from the soil layers. Additionally, information on sowing and harvest periods are not included in the current version of Noah-MP, while irrigated areas are defined based on a global dataset (Salmon et al., 2015) which can suffer accuracy limitations. Indeed, the absence of annual dynamic information on irrigated fields, the unknown yearly variability of the crop types and the impact of the meteorological conditions in the stakeholders decision process (i.e., sowing) make the simulation of Noah-MP prone to LAI peak shifts, as compared to observations, when irrigation is simulated. Another important aspect affecting LAI simulations is its sensitivity to RZSM, which might be more difficult to simulate than SSM during the irrigation season due to larger impacts of the soil texture and transpiration processes along with the high frequency of the wetting and drying phases caused by irrigation events. This results in a significant performance deterioration (often worse than LAI simulation not including irrigation which are mainly driven by seasonality, see Figure 3.10). By contrast, irrigation modeling helps in reducing the bias of the LAI simulated time series, which, in the cropland area, show a significant underestimation when irrigation is not considered.

The limitations found in simulating LAI and vegetation by Noah-MP even when irrigation was simulated could potentially be overcome by assimilating Sentinel-1 σ^0 data. To explore this potential, we compared the LAI from both model runs, and from PROBA-V, with the observed Sentinel-1 σ^0 CR, which should provide information about the vegetation dynamics (Vreugdenhil et al., 2020, 2018). The Natural run drastically underestimated the LAI during the late summer months which can be explained by the lack of both irrigation simulation and a specific crop model in Noah-MP. Indeed, this issue is partly compensated in the Irrigation run. The correlation between σ^0 CR and LAI from PROBA-V was much higher than that between σ^0 CR and the simulated LAI by Noah-MP (see Figure 3.10) suggesting that Sentinel-1 σ^0 DA could help in correcting poor LAI model simulations. Additionally, a higher correlation was found between the σ^0 VV observations and the simulated SSM when irrigation was turned on than in the absence of irrigation, suggesting that the assimilation of σ^0 VV could improve SSM where irrigation is poorly or not modeled. On the other hand, considering the low correlation between the VH signal and SSM in presence of vegetation (Baghdadi et al., 2017), and its close relation with vegetation

(Ferrazzoli et al., 1992; Macelloni et al., 2001), future DA experiments will investigate the contribution of VH and CR in improving LAI predictions and irrigation quantification.

Finally, bi-weekly accumulated irrigation estimates in Figure 3.10 agree well with real irrigation applications, suggesting that the large-scale LSM irrigation scheme is helpful for intensively irrigated areas. On the other hand, the poor soil and crop parameterization along with other unknown parameters related to the irrigation management (e.g., the farmers can apply more water than actually needed) can cause large biases in these irrigation simulations. Again, ingestion of radar σ^0 data could correct for unmodelled processes. More specifically, Sentinel-1 σ^0 could correct: (i) for the magnitude and timing of the irrigation simulations; and (ii) for Noah-MP irrigation predictions over not irrigated regions.

3.3.2 WCM backscatter simulation

The purpose of the presented WCM observation operator calibration and evaluation was to optimize the parameters for the future assimilation of the Sentinel-1 σ^0 VV and VH into Noah-MP. Such an optimization would ideally minimize the long-term bias between the simulated and observed σ^0 signals. This can be achieved by calibrating the observation operator with long-term observed σ^0 prior to DA, but in this process, it is crucial to avoid potential error cross-correlation between model observation predictions and observations. Furthermore, a good observation operator should not already compensate for missing processes in the LSM by accepting effective, but unrealistic, optimized parameters, because it would then lose its physically-based ability to accurately convert misfits between observations and simulations to LSM updates during DA.

One way to avoid parameters compensation for erroneous LSM input into the WCM would be to use observed time series of e.g. LAI. However, LAI products from different sensors have different biases themselves which can add bias to the σ^0 simulations, and more importantly, replacing simulated LAI or SSM with external datasets would undermine the possibility of updating these variables in the future assimilation system. Based on that, we performed the WCM calibration considering SSM and LAI model input from two different experiments: a *Natural* run and an *Irrigation* run, as well as two cost functions, a Bayesian solution *J* and a *KGE* solution which

resulted in four calibration experiments for each polarization (i.e., eight calibration experiments in total).

The calibration experiments using simulations from the *Natural* run as input showed a limited performance and provided presumably bad vegetation parameter estimates which resulted in unrealistic peaks in the simulated σ^0 during the summer, when driven by higher modeled LAI during this period. The inclusion of the irrigation within Noah-MP was very beneficial for all the calibration experiments helping in reducing the bias and increasing the correlation with Sentinel-1 σ^0 as well as removing the anomalous σ^0 increase during warm periods especially for the *KGE*-based calibration. This corroborates our initial hypothesis that, over intensively irrigated areas, the simulation of irrigation is a mandatory task for an optimal calibration of the WCM. Irrigation modeling, even if only done approximately and perhaps with inaccurate timing, reduces obvious land surface (soil moisture, vegetation) bias and avoids that the WCM needs to compensate for this bias.

Our results show overall higher performance in terms of KGE and Pearson-R scores for the *KGE*-based calibration, whereas the long-term bias was better reduced for the *J*-based calibration, which is beneficial in anticipation of future DA. This is because in the *J* cost function i) a target accuracy term which takes into account also the Sentinel-1 observations error is present; and, ii) a parameter deviation penalty based on the prior parameters constraints is used, which avoid parameters to largely deviate to their prior values.

In terms of polarization, we found σ^0 VH simulations much more sensitive to the inclusion of the irrigation (vs non inclusion) in Noah-MP, suggesting that observed σ^0 VH might also contain much more information about irrigation (via the influence of the vegetation change due to irrigation) than that contained in σ^0 VV which is normally used for SSM retrieval (Vreugdenhil et al., 2020). We believe that the cause of this is related to a comparatively larger σ^0 of vegetation with respect to that of the soil when the crops are well developed. This was also corroborated by the better agreement between CR and LAI from PROBA-V in one of the study sites mentioned above. Despite this, further investigations are required to confirm this hypothesis and DA will certainly help to test this aspect.

3.4 Conclusions

Starting from the hypothesis that satellite observations should contain useful information about human impacts such as irrigation on the water cycle, the second part of this thesis addresses the potential use of innovative EO for tracking human-induced changes to the terrestrial water cycle, and particularly on irrigation quantification. With the specific focus on intensively irrigated land, the first step of this activity was to investigate the optimal calibration of the WCM as observation operator for the future ingestion of Sentinel-1 backscatter into the Noah-MP LSM via DA. In this context, additional objectives were: 1) unveiling strengths and limitations of irrigation simulation in LSMs from the perspective of calibrating the WCM; 2) identifying the potential irrigation-related information contained in the Sentinel-1 backscatter observations to improve soil moisture and vegetation states as well as irrigation estimates in a calibrated DA system.

To reach these objectives the Noah-MP LSM was coupled with a sprinkler irrigation scheme within LIS and performed two different simulation experiments, one with and one without irrigation (i.e., *Natural* and *Irrigation* runs). Moreover, a WCM was coupled with Noah-MP and different calibration options were tested to prepare for optimal, future, assimilation of backscatter VV and VH to update both soil moisture and vegetation states.

The main conclusions drawn from our evaluation are as follows:

- Over highly irrigated areas, the simulation of irrigation in LSMs helps to provide better soil moisture and vegetation simulations which can be used with benefit as input for the WCM calibration. However, the performance of the irrigation simulations is limited by the simplistic model parameterization of this human process and the necessity to consider realistic and updated land cover information (e.g., crop types). This results in poor simulations of the irrigation timing and quantities as well as vegetation dynamics.
- The Sentinel-1 backscatter observations contain useful information about SSM and vegetation over highly irrigated areas. This information can be exploited to overcome LSM deficiencies in simulating soil moisture and vegetation over highly irrigated regions, e.g., when irrigation is unmodeled, or poorly modeled because of uncertainties due to

crop types, irrigation timing, and farmer agricultural practices. In particular, there is a high chance that the assimilation of Sentinel-1 backscatter can help in correcting LAI dynamics.

- The optimal assimilation of Sentinel-1 backscatter into a LSM must rely upon a well calibrated WCM as observation operator to provide unbiased backscatter simulations with a minimal chance of having error cross-correlations between model and observations, while ensuring a realistic operator controllability or realistic connection between observed signals and land surface state variables. Calibrating the WCM with inclusion of irrigation modeling consistently led to a better agreement with Sentinel-1 backscatter. The modeling of irrigation in the LSM simulations, even if not done optimally, avoids that the WCM calibration compensates for LSM biases.
- It was demonstrated that the WCM calibration with a Bayesian cost function, including a prior parameter constraint, provides the optimal WCM parameters, able to generate the lowest bias in the backscatter simulations for both VV and VH. Although slightly higher correlations are obtained when using a *KGE* cost function, unbiased estimates are particularly beneficial for DA as this minimizes the chance of potential error cross-correlation between model estimates and observations.

The results obtained in this chapter improve the understanding of the LSM limitations in simulating irrigation and highlight the information content in Sentinel-1 backscatter data. The latter will be used in a subsequent DA system (Chapter 4).

Chapter 4: Data assimilation of Sentinel-1 backscatter

This chapter describes the analysis and results based on a preprint of the following publication, submitted to HESS:

Modanesi, S., Massari, C., Bechtold, M., Lievens, H., Tarpanelli, A., Brocca, L., Zappa, L. and De Lannoy, G. J. M. ***Challenges and benefits of quantifying irrigation through the assimilation of Sentinel-1 backscatter observations into Noah-MP****. Submitted to HESS, 2022.*

In this Chapter the potential information contained into Sentinel-1 backscatter observations to improve irrigation estimates was tested in the framework of a data assimilation (DA) system composed by the Noah-MP land surface model (LSM), equipped with a sprinkler irrigation scheme, and a backscatter operator represented by a Water Cloud Model (WCM), as part of the NASA Land Information System (LIS) framework. The calibrated WCM was used as observation operator in the DA system to map model surface soil moisture (SSM) and leaf area index (LAI) into backscatter predictions and, conversely, map observation-minus-forecast backscatter residuals back to updates in soil moisture and LAI through an ensemble Kalman filter (EnKF).

The benefits of Sentinel-1 backscatter observation in two different polarizations (VV and VH) were tested in two separate DA experiments, performed over two irrigated sites, the first one located in the Po Valley (Italy) and the second one located in northern Germany. Chapter 4 is organized as follows: i) Section 4.1 describes data and methodologies used; ii) Section 4.2 presents results obtained; ii) Section 4.3 discusses the results obtained; and finally, iii) conclusions are drawn in Section 4.4. It is worth noticing that the WCM setup in Chapter 4 slightly differs from that in Chapter 3. More details are given in Section 4.1.

4.1 Data and methods

4.1.1 Study area and in situ data

Two European pilot sites characterized by different climatic conditions were selected (Figure 4.1). The first one is located in the Niedersachsen region in Northern Germany and has an extent of 160 km^2, marked by the transparent red box in Figure 4.1a. It can be classified as Cfb (temperate

oceanic climate) in the Koeppen–Geiger classification (Peel et al., 2007). Mean annual temperature and precipitation are around 9 °C and 550 mm, respectively. For more general information on this pilot site the reader can refer to the work by Zappa et al. (2021). The test site is composed of 49 fields (ranging from 1.3 ha to 30 ha) characterized by a wide variety of crops, which include potatoes, sugar beet, summer barley and winter wheat. Daily irrigation data, available for each field, were provided for the year 2018.

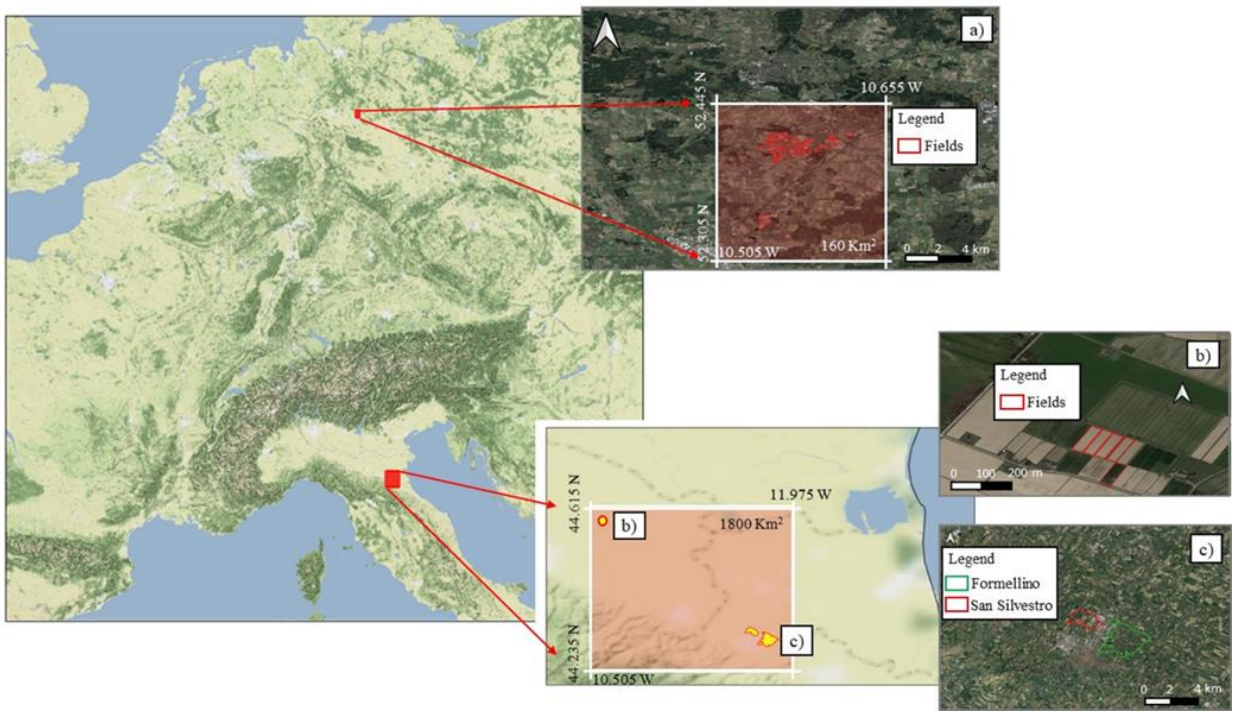

Figure 4.1. Study area composed by the Italian and German pilot sites (represented by the red boxes). The pilot sites include three test sites: a) Niedersachsen; b) five fields in Budrio; and c) two small districts close to the city of Faenza, called San Silvestro and Formellino. Map data ©2015 Google.

The second pilot site is located within the Po Valley, one of the most important agricultural areas in Italy, intensively equipped for irrigation (Salmon et al., 2015). According to the Köppen-Geiger climate classification this area can be ascribed to the Cfa class (temperate climate, without dry season and with hot summers). The simulation area (red box on Figure 4.1b-c) is mainly characterized by croplands, except the south, south-western area where forests and more complex topography are dominant. This pilot site has an extension of 1800 km²; it is located in the Emilia Romagna region and is characterized by one of the most technologically advanced Italian irrigation hydraulic system - the Canale Emiliano Romagnolo (CER,

https://consorziocer.it/it/). In recent years, this area was affected by frequent water scarcity periods (Ceppi et al., 2014; Strosser et al., 2012), which have increased the need for optimal water management. In situ data, used for evaluation, were collected over the test site of Budrio (Figure 4.1b) and Faenza (Figure 4.1c). In particular, the Budrio farm is managed by CER and includes five small fields extended for 0.4 ha each. The most common crop types are tomatoes and maize and daily irrigation data are available for the period 2015-2016 for four out of the five fields and for the year 2017 for the last plot. The second Italian test site is located around the city of Faenza, consisting of two small-districts: San Silvestro (hereafter Faenza F1) which has an extension of 290 ha, and Formellino (Faenza F2 hereafter), reaching 760 ha. The crops growing on the Faenza small-districts are pear and kiwi which typically require a significant amount of water. The water used for irrigation at daily time scale was provided by CER for the two years 2016-2017.

4.1.2 Remote sensing observations

The European Space Agency (ESA) and Copernicus Sentinel-1 mission collects active microwave (MW) backscatter data at C-band (5.4 GHz) at a high spatial (~ 20 m) and temporal (less than weekly) resolution in Interferometric Wide (IW) swath mode. In this Chapter, the backscatter observations used in Chapter 3 (sigma-nought [σ^0]) were replaced with an improved backscatter product (gamma-nought) which takes into account topographic variations. The complete processing of the ground-range detected (GRD) backscatter observations in VV- and VH-polarization was done using the ESA Sentinel Application Platform (SNAP) software and included standard techniques: precise orbit file application, border noise removal, thermal noise removal, radiometric calibration to backscatter as beta-nought, terrain flattening to backscatter as gamma-nought (γ^0 hereafter), and range-Doppler terrain correction. Furthermore, the γ^0 observations, originally acquired at ~20 m spatial resolution, were aggregated by multilooking, masked for urban area and water bodies, and projected on the 0.01° latitude-longitude grid as used in LIS Noah-MP LSM. After applying an orbit bias-correction (Lievens et al., 2019), the observations from different orbits, either from Sentinel-1A or -1B and ascending or descending tracks, were combined at the daily time-scale.

Additional remote sensing (RS) observations were used for the evaluation of Noah-MP LSM simulations:

- The Metop ASCAT surface soil moisture (SSM) Climate Data Records H115 and its extension H116 are provided by the European Organization for the Exploitation of Meteorological Satellites (EUMETSAT) Support to Operational Hydrology and Water Management (H SAF; http://hsaf.meteoam.it/). The SSM retrieval is characterized by a spatial sampling of 12.5 km and a temporal resolution of one to two observations per day, depending on the latitude.
- The PROBA-V Leaf Area Index (LAI) is provided by the Copernicus Global Land Service programme (CGLS, https://land.copernicus.eu/global/). The CGLS product at 1 km spatial resolution and 10-day temporal resolution is developed based on the work by Verger et al. (2014).
- The Moderate Resolution Imaging Spectroradiometer (MODIS) is a multispectral sensor on-board TERRA and AQUA satellites acquiring image data of the Earth's surface simultaneously in visible/infra-red bands. For this work the MOD16A2 Version 6 Evapotranspiration product was used for evaluation. This is an 8-day composite product characterized by 500-meter spatial resolution.

ASCAT SSM, PROBA-V LAI and MODIS ET were extracted over the test sites and re-gridded over the LIS grid spatial domain (0.01°) as well as subsampled to a daily time scale in order to match the LIS outputs.

4.1.3 Land surface and irrigation modeling

The LSM selected for this study is the Noah-MP.v.3.6 (Niu et al., 2011). This model is able to dynamically simulate vegetation and soil moisture in 4 layers, i.e., 0–10, 10–40, 40–100 and 100–200 cm depth. For this study, the Noah-MP model was coupled to a sprinkler irrigation module (Ozdogan et al., 2010a) embedded within the NASA's LIS version 7.3 (Kumar et al., 2008). For a more detailed description of the Noah-MP parameterization used in this study the reader can refer to Modanesi et al. (2021).

The irrigation module adds water as pseudo-precipitation to mimic sprinkler systems (Ozdogan et al., 2010a), and does not further change processes related to e.g., vapor fluxes (which would be needed for highly efficient drip irrigation systems; Evans and Zaitchik, 2008). In order to identify the timing and location of irrigation, four conditions need to be met: (i) irrigable land cover (i.e., croplands), (ii) irrigated land fraction, (iii) growing season and (iv) dry enough root-zone soil moisture (RZSM). The first two conditions are tested against static land cover (LC) and irrigation intensity (areal fraction) maps. The growing season was defined based on a user-defined threshold of simulated LAI (LAI>1). The LAI value is then converted to the greenness vegetation fraction (GVF) following Fang et al. (2018):

$$GVF = 1 - e^{-b*LAI} \quad (4.1)$$

where b [-] is an empirical parameter that depends on plant canopy (Fang et al., 2018; Norman et al., 1995). Finally, the irrigation is applied when the RZSM availability falls below a user-defined threshold, which has been set to 50% of field capacity (FC) as in Ozdogan et al. (2010) for the German pilot site and 45% in Italy (a previous analysis has shown large overestimations using a threshold of 50% in the Po Valley). The irrigation amount is determined by the amount of water needed to increase the RZSM back to FC. In this context, the maximum rooting depth is an important input parameter, impacting the frequency of irrigation events as well as the amount of irrigated water.

The modelled irrigation estimates are thus primarily controlled by five datasets: static LC, irrigation fraction, soil texture, crop type, and dynamic meteorological forcing. In this study, the static 1-km LC is derived from the CGLS 100 m global LC map for the year 2015 (Buchhorn et al., 2020; available at https://land.copernicus.eu/global/products/lc). The 23 classes of this global LC map were reclassified to the 14 classes supported by LIS and re-gridded to 0.01° (for additional details on the reclassification the reader can refer to Modanesi et al., 2021). The global 500-m rain-fed, irrigated, and paddy croplands dataset (GRIPC) by Salmon et al. (2015) is used to map the irrigation fractional area. However, the GRIPC input lacks important information over the German test site, which is classified as non-irrigated. In order to allow irrigation simulations over Germany, the irrigation fractional area was set to 100% over the known irrigated LIS grid pixels

(based on our irrigation benchmark data). Soil texture and the associated parameters were extracted from the 1-km Harmonized Soil World Database (HWSD v1.21) and mapped to discrete soil classes with their associated soil hydraulic parameters as in Modanesi et al. (2021). Given the lack of European or large-scale dynamic crop map datasets, the crop type was set to a generic type with a maximum rooting depth of 1 m in Italy (Modanesi et al., 2021) and 0.8 m Germany. In particular, in the Niedersachsen test site, an averaged rooting depth was calculated based on the main crop types cultivated at the irrigated fields.

The dynamic meteorological forcing data were extracted from Modern-Era Retrospective analysis for Research and Applications, version 2 (MERRA-2; Gelaro et al., 2017), which is not corrected for surface or screen-level observations (and are thus unlikely to contain feedback from -unmodelled and unobserved- irrigation). The meteorological data were mapped to 0.01° spatial resolution via bilinear interpolation.

4.1.4 Observation operator and calibration

The observation operator used to ingest Sentinel-1 γ^0 observations into the Noah-MP LSM is represented by the Water Cloud Model (WCM) introduced by Attema and Ulaby (1978). The WCM simulates the total γ^0 as the sum of the γ^0 from the vegetation (γ^0_{veg}) and the γ^0 from the soil (γ^0_{soil}) attenuated by the vegetation (t^2) as follows:

$$\gamma^0_{tot} = \gamma^0_{veg} + t^2\gamma^0_{soil} \tag{4.2}$$

For more information on the WCM the reader can refer to Chapter 3 or to Lievens et al. (2017a) and Modanesi et al. (2021). The WCM includes four fitting parameters, two of them related to the scattering and attenuation by vegetation and the other two parameters to model the soil backscatter contribution as a linear function of the SSM. Those parameters were calibrated to limit long-term biases between Sentinel-1 observations, which include an irrigation signal over irrigated areas, and the LSM simulations. The WCM calibration was performed for each individual grid cell using the procedure designed in Chapter 3 and Modanesi et al. (2021) which includes: i) the use of Noah-MP SSM and LAI as inputs for the WCM (ensemble mean time series from an open loop (OL) simulation); ii) the use of Sentinel-1 γ^0 VV and VH separately to tune the

parameters for the simulation of γ^0 VV and VH independently; iii) the activation of the irrigation scheme to reduce seasonal inconsistencies between simulated and observed γ^0 during irrigation periods; iv) the optimization of a Bayesian objective function represented by the Sum of Square Error (SSE) between γ^0 observations and simulations, and a constraint on prior parameter estimates, using the DiffeRential Evolution Adaptive Metropolis (DREAM(ZS); Vrugt et al., 2008; De Lannoy et al. 2014) instead of the PSO used in Chapter 3. In the WCM (see equations 3.1 to 3.4), the incidence angle was set to zero, considering that the γ^0 terrain-flattened version do not include information on the incidence angle. As a final note, the WCM calibration procedure addresses the general Bayesian assumption of unbiased observations and simulations. Relying on that, a subsequent bias correction between simulated and observed backscatter is not needed before DA. The calibration was realized for the period January 2018-December 2020.

4.1.5 Data assimilation

The DA system was developed in order to directly assimilate Sentinel-1 γ^0 observations into Noah-MP and sequentially update both soil moisture and vegetation within the LIS framework. The direct assimilation of γ^0 observations requires that simulated land surface state variables are first mapped to γ^0 predictions (forecast) via a second modelling step, i.e. via the WCM as observation operator. The assimilation was performed via an ensemble Kalman filter (EnKF; Evensen, 2003, 1994) which updates the land surface state, where and when satellite-based γ^0 observations are available. Specifically, a 1-dimensional EnKF was applied (Reichle et al., 2002), using Sentinel-1 observations at the same spatial grid as that of the model simulations. In this study, the updated land surface state variables during the assimilation include both SSM (0-10 cm) and LAI, and the deeper profile layers are also updated (10–40, 40–100 and 100–200 cm) via error cross correlations. All other fluxes and state variables, including irrigation estimates, are consistently adjusted via model propagation.

The EnKF assumes unbiased observations and forecasts. This is achieved by calibrating the WCM parameters as described in Section 4.1.4. The optimality of the Kalman filter further strongly depends on the characterization of the random component of forecast and observation errors. In this context, the forecast errors are diagnosed from an ensemble of 24 land model (including

WCM) trajectories from which the error covariances are estimated at the time of an update. The ensembles are generated by perturbing selected meteorological input forcings (i.e., rainfall, incidence longwave and shortwave radiations) and state variables. The perturbation parameters, summarized in Table 4.1, are based on Kumar et al. (2014) aiming at a unit standard deviation of normalized γ^0 innovations (De Lannoy and Reichle, 2016b; Reichle et al., 2017a). In terms of state variables, only the SSM and LAI are perturbed and no temporal autocorrelation is used to avoid excessive uncertainty estimates. The observation error standard deviation is set to 1 dB, regardless of the polarization or orbit of the γ^0 observations.

The main equation of the EnKF can then be written as follows:

$$\widehat{x_i^+} = \widehat{x_i^-} + K_i\left[y_{obs,i} - h_i(\widehat{x_i^-})\right] \tag{4.3}$$

where i represents the time step, $\widehat{x_i^+}$ is an ensemble of model states after assimilation and $\widehat{x_i^-}$ represents the forecast ensemble state (i.e., SSM and LAI), $y_{obs,i}$ are the assimilated observations at time i and $h_i(.)$ is the WCM observation operator. The term $y_{obs,i} - h_i(\widehat{x_i^-})$ is the γ^0 observation-minus-forecast (O-F) residual in dB, and is mapped to updates in the model state via the Kalman gain K_i described as follows:

$$K_i = [C_{YM}(C_M + C_v)^{-1}]_i \tag{4.4}$$

In Equation (4.4) $C_{YM,i}$ is the error cross covariance matrix between the state and observation predictions, $C_{M,i}$ is the forecast error covariance matrix of the backscatter (observation) predictions.

Generally, DA has the potential to contribute to the estimation of irrigation as follows. First, the amount of water or vegetation added to the system via DA (i.e., the increments) could be related to irrigation amounts i) if the true precipitation is used as input; ii) if no irrigation is simulated; and iii) if the observation operator is also not compensating for irrigation. More specifically, positive and autocorrelated increments in the growing season would be indicative of irrigation, and this would also be indicative of a suboptimal assimilation system. In this study, we use imperfect reanalysis precipitation input and we simulate irrigation through an irrigation scheme. Increments of any sign could thus be related to over- or underestimation of irrigation.

Table 4.1: Perturbation parameters for forcing (i.e. rainfall, incident and shortwave radiation) and state variables (i.e., SSM and LAI)

Variable	Perturbation Type	Standard deviation
Rainfall [kg/m^{2}s]	Multiplicative	0.5
Incident longwave radiation [W/m2]	Additive	50.0
Incident shortwave radiation [W/m2]	Multiplicative	0.3
SSM [m^3/m^3]	Additive	0.012
LAI [-]	Additive	0.04

4.1.6 Experiments

In this study we considered two different experimental lines: i) the assimilation of Sentinel-1 γ^0 VV (*Sentinel-1 γ^0 VV DA* hereafter), and ii) the assimilation of Sentinel-1 γ^0VH (*Sentinel-1 γ^0VH DA* hereafter), both to sequentially update SSM and LAI. The DA experimental workflow is described in the scheme of Figure 4.2.

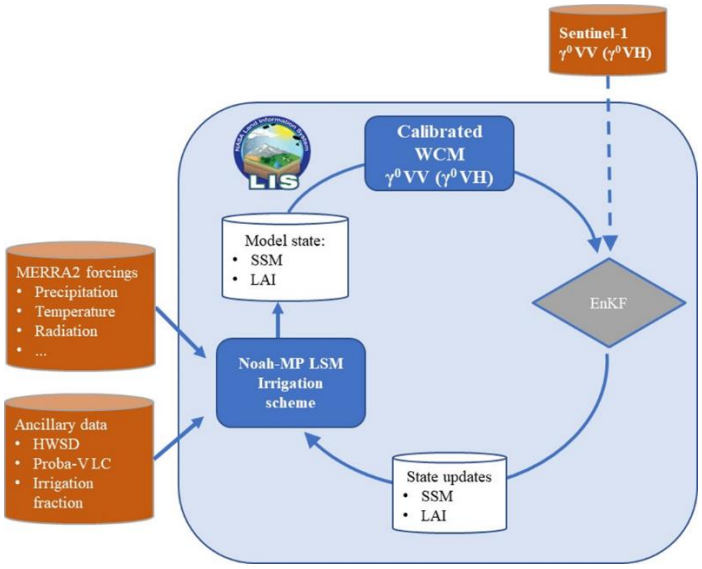

Figure 4.2. Workflow of the DA experiments realized within the LIS framework. The scheme describes how the Sentinel-1 γ^0 (VV or VH) is assimilated into the Noah-MP LSM to sequentially update SSM and LAI using an EnKF.

It is worth mentioning that Figure 4.2 only includes the workflow related to the DA experiments and that the WCM calibration procedure, which is not included, is realized using outputs from a

reference Noah-MP OL run (i.e., the ensemble mean SSM and LAI). For each pilot site, the Noah-MP model was previously spun-up from January 1982 to May 2014. Then, an ensemble spin-up was realized in Open Loop (OL) mode using 24 ensemble members from May 2014 to January 2015, in order to obtain optimal initial conditions. The OL run was continued thereafter from January 2015 onwards through December 2020. Similarly, the Sentinel-1 γ^0 VV DA and Sentinel-1 γ^0 VH DA experiments were run from January 2015 through December 2020.

4.1.7 Evaluation

The evaluation aimed at i) verifying the goodness of the DA system in terms of DA diagnostics; ii) highlighting benefits of the Sentinel-1 DA for irrigation, soil moisture and LAI estimation as well as testing the differences between the Sentinel-1 γ^0 VV DA and the Sentinel-1 γ^0 VH DA configurations, iii) verifying the influence of the spatial scale of the test sites on the irrigation simulation and evaluation, and iv) identifying shortcomings of the system.

To achieve those targets, two types of evaluation were carried out:

- The optimality of the DA system design was evaluated regionally for each pilot site, for the period January 2015-December 2020. Following Reichle et al. (2017), three different filter diagnostics were analyzed. First, the difference between the temporal mean ensemble standard deviation (or ensemble spread) of the DA and OL runs was computed to test whether the DA system successfully reduces the uncertainties compared to the OL run. Indeed, the ensemble spread depends on the perturbed forcing and states (as described in Table 4.1) which diagnose the forecast error. An update is provided by the EnKF at the time of each observation (analysis), theoretically providing a reduction of the spread. Second, the time-series standard deviation of the normalized γ^0 O-F residuals was computed to check if observation and model errors were adequately chosen. The normalized O-F residuals were obtained by normalizing each O-F residual by their simulated (expected) (forecast and observation error) standard deviation and then calculating the time-series standard deviation (Bechtold et al., 2020; Reichle et al., 2019). Third, the time-series standard deviations of the increments (analysis - forecast) in SSM and LAI were investigated.

- The OL and DA estimates of irrigation, SSM, LAI and ET were evaluated using independent reference data for the year 2018 at the German sites, and for the years 2015-2017 and 2016-2017 at the Budrio and Faenza (Italian) sites, respectively. The evaluation of ensemble mean irrigation simulations was assessed in terms of correlation and percentage bias (Pearson R and bias hereafter) between estimated irrigation volumes and benchmark irrigation data. As the irrigation timing is often driven by stakeholders' turns to withdraw water and by water availability rather than by the RZSM conditions, and because short-term DA increments influence short-term activations of the irrigation system, the comparisons between simulations and in-situ observations were carried out by accumulating irrigation data at bi-weekly time window. An evaluation of daily SSM and LAI outputs was performed against ASCAT SSM and PROBA-V LAI, respectively, in terms of Pearson-R. The ET outputs were tested against MODIS ET, considering the important role that irrigation has in affecting ET (Haddeland et al., 2014; Lawston et al., 2015). The latter however, must be considered more a comparison than a real validation given the inherent uncertainties contained in the MODIS ET product.

  The evaluation of the 0.01° irrigation simulations with benchmark data asks for careful data handling and offers opportunities to relate skill metrics to properties of the irrigated regions. First, the Italian pilot site is composed of Budrio with five small fields of 0.4 ha within one LIS grid cell (0.01°), the Faenza F1 test site of 290 ha, covering three LIS grid cells, and Faenza F2 of 760 ha including eight LIS grid cells. The benchmark irrigation data for the five fields in Budrio were averaged to obtain a unique time series, whereas at the Faenza test sites the LIS simulations were averaged to obtain a single time-series for each field (and for each analyzed variable). This allows to relate skill metrics to the spatial scale (one pixel at Budrio, to district scale at Faenza) of simulations and reference data. Second, the German pilot site is composed of 49 fields, covering 24 LIS pixels. By considering only pixels with a percentage of irrigated area larger than 25%, 8 irrigated pixels were retained of the 24 pixels. For these 8 pixels, statistical distributions of the skill metrics were obtained.

4.2 Results

4.2.1 Data assimilation diagnostics

The two DA experiments (Sentinel-1 γ^0 VV DA and Sentinel-1 γ^0 VH DA) were evaluated in terms of DA optimality and increments, over the period January 2015-December 2020 for both Germany and Italy. Figure 4.3 shows a general reduction in the time-mean ensemble spread in SSM or LAI due to DA compared to the spread of the OL runs (ΔSSM Ens. Spread mean; ΔLAI Ens. Spread mean), for both the Sentinel-1 γ^0 VV and VH DA experiments. In Italy (Figures 4.3a, c, e and g) a larger reduction of the ensemble SSM and LAI spread is identified over croplands and particularly over the western, north-western part of the study area where a higher number of observations is assimilated (maps representing the number of assimilated observations for each experiment and each test site are displayed in Figure 4.4i-l). The patches with a lower spread reduction are associated to input soil parameters and in particular to the presence of silty-loam soil texture which contrasts the sandy-loam soil of the remaining area (LIS input maps for Italy are shown in figure 4.4a-d). The two texture classes lead to very different soil moisture time series. In a previous study Modanesi et al. (2021) a lower agreement of calibrated WCM simulations with Sentinel-1 observations was found over the silty-loam soil texture, and this reflects in the lower reduction of SSM spread when assimilating Sentinel-1 (Figures 4.3a and 4.3c). These features are much less visible in the difference of LAI spreads (LAI is mainly associated with the almost homogenous vegetation class, not so much with texture). Furthermore, the Sentinel-1 γ^0 VH DA displays larger spread reduction in terms of LAI over croplands compared to the Sentinel-1 γ^0 VV DA experiment, showing a large influence of the vegetation in the γ^0 VH signal. For Germany the results show a similar link between the soil texture and the SSM spread reduction, especially for the Sentinel-1 γ^0 VV DA experiment (Figure 4.3b) where pixels with a stronger spread reduction are associated to sandy-loam soil texture (LIS input is shown in Figure 4.4e-h for Germany). The absolute mean decrease in spread (m) over Germany is less pronounced than for the Italian pilot site (e.g. for Sentinel-1 γ^0 VH DA, ΔLAI Ens. Spread mean m=-0.1 for Italy and m=-0.05 for Germany), which is partly due to the state-dependency of the spread (e.g. higher LAI values and larger spreads in Italy than in Germany).

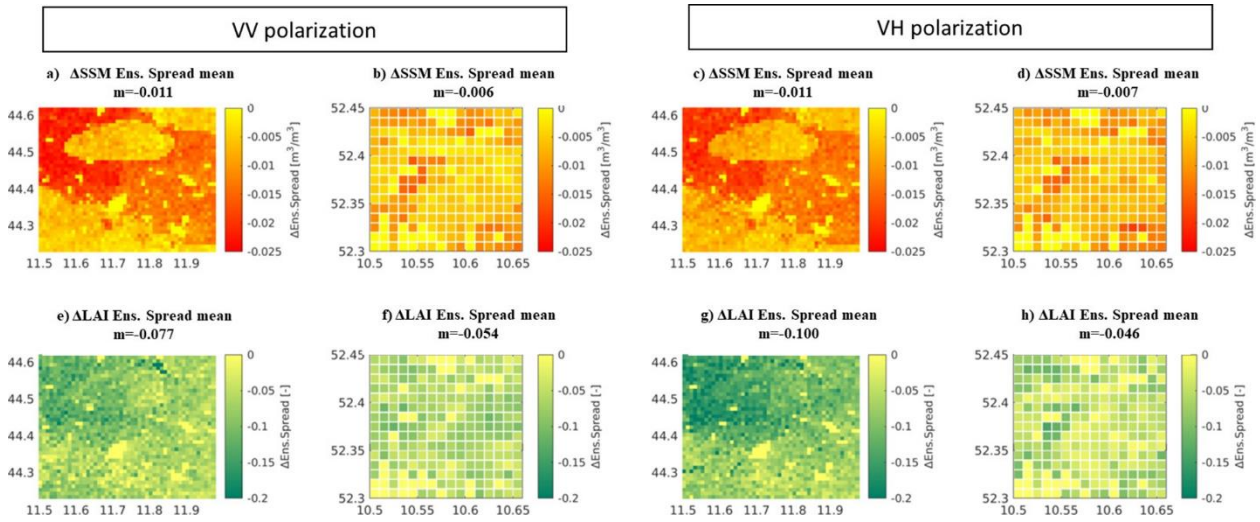

Figure 4.3. Maps of the difference in time-mean ensemble spread between the DA and OL runs for (top) SSM (ΔSSM Ens. Spread) and (bottom) LAI (ΔLAI Ens. Spread). ΔSSM Ens. Spread after Sentinel-1 γ^0 VV DA a) in Italy, b) in Germany; Sentinel-1 γ^0 VH DA c) in Italy, d) in Germany. (e,f,g,h) Similar to (a,b,c,d) but for ΔLAI Ens. Spread. m is the mean over the entire study area. The reference period is January 2015-December 2020. In each plot, the x- and y-axes represent longitudes and latitudes in degrees east and north, respectively.

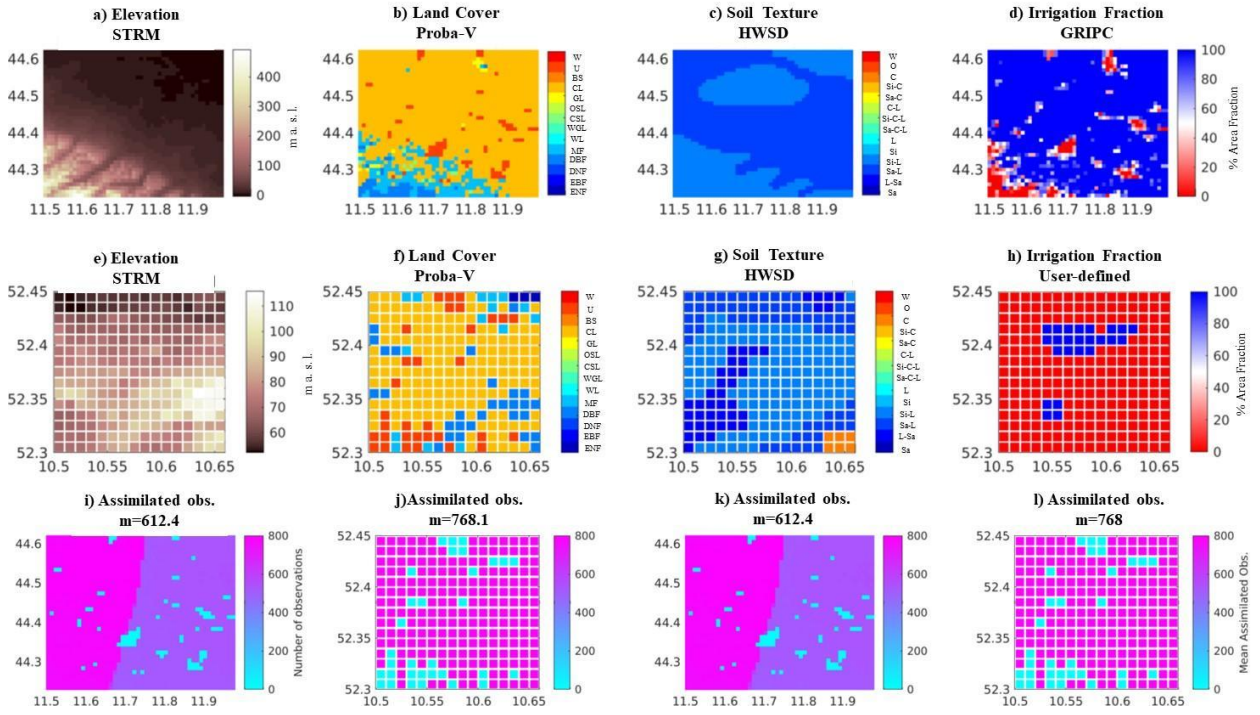

Figure 4.4. LIS input data over the Italian pilot site: a) Elevation from the Shuttle Radar Topography Mission (SRTM); b) Proba-V LC; c) HWSD soil texture; and d) GRIPC irrigation fraction map. Same in e), f) g) for Germany, except for the h) irrigation fraction, equally defined at 100% over the irrigated pixels. Maps of the number of assimilated Sentinel-1 observations for: *Sentinel-1 γ^0 VV DA* i) in Italy and j) in Germany; Sentinel-1 γ^0 VH DA k) in Italy and l) in Germany. m is the mean over the entire study area. The reference period is January 2015-December 2020. In each plot, the x- and y-axes represent longitudes and latitudes in degrees east and north, respectively.

Figure 4.5 shows the time series standard deviation of the normalized O-F residuals, for both the Sentinel-1 γ^0 VV DA and Sentinel-1 γ^0 VH DA. In an optimal DA system these values should be equal to 1 over the entire study area for an agreement between the actual and simulated (expected) forecast and the observation errors. In Italy, m=0.83 and m=0.82 are obtained for the Sentinel-1 γ^0 VV DA and the Sentinel-1 γ^0 VH DA experiments respectively but, once again, the spatial patterns are consistent with the soil texture distribution. The large ellipsoid feature, in the northern side of the study area, is characterized by values exceeding the unity, meaning that the sum of observation and forecast error, prescribed in the ensemble perturbation, underestimates the actual errors. Similarly, in Germany we obtain near-optimal results in terms of m values over the entire study area but larger error underestimations are observed over the silty-loam soil texture, with values larger than 1.5 for both DA experiments (Figures 4.5b and 4.5d). In Germany an additional source of uncertainty is related to the irrigation fraction information, which is zero over the entire cropland area, except for the pixels for which we collected irrigation benchmark data (see discussion on GRIPC input, Section 4.1.3). We hypothesize that the lack of accurate information on the irrigated fraction over other pixels can negatively affect the WCM calibration and indeed the results in terms of DA diagnostics. It has to be noted that over white pixel any observation was assimilated (Figure 4.4i-l).

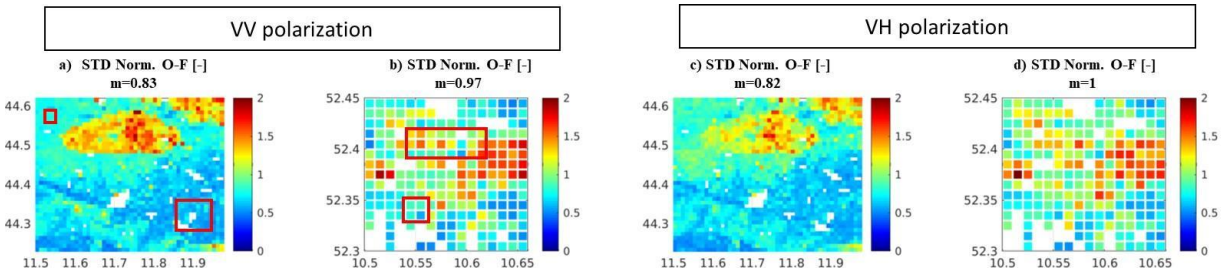

Figure 4.5. Maps of the standard deviation (STD) of the O-F residuals for: Sentinel-1 γ^0 VV DA a) in Italy and b) in Germany; Sentinel-1 γ^0 VH DA c) in Italy and d) in Germany. m is the mean over the entire study area. The reference period is January 2015-December 2020. Over white pixels observations were not assimilated. In each plot, the x- and y-axes represent longitudes and latitudes in degrees east and north, respectively.

Finally, we analyzed the increments of SSM and LAI over the study area. In a well-calibrated DA system, the long-term mean of the increments is expected to be close to zero at each pixel. As explained in Reichle et al. (2019), values close to zero indicate that no long-term net addition or

subtraction of water (or vegetation) is generated by the analysis. As expected, the temporal mean values of SSM and LAI analysis increments vanish in the regional average (results not shown).

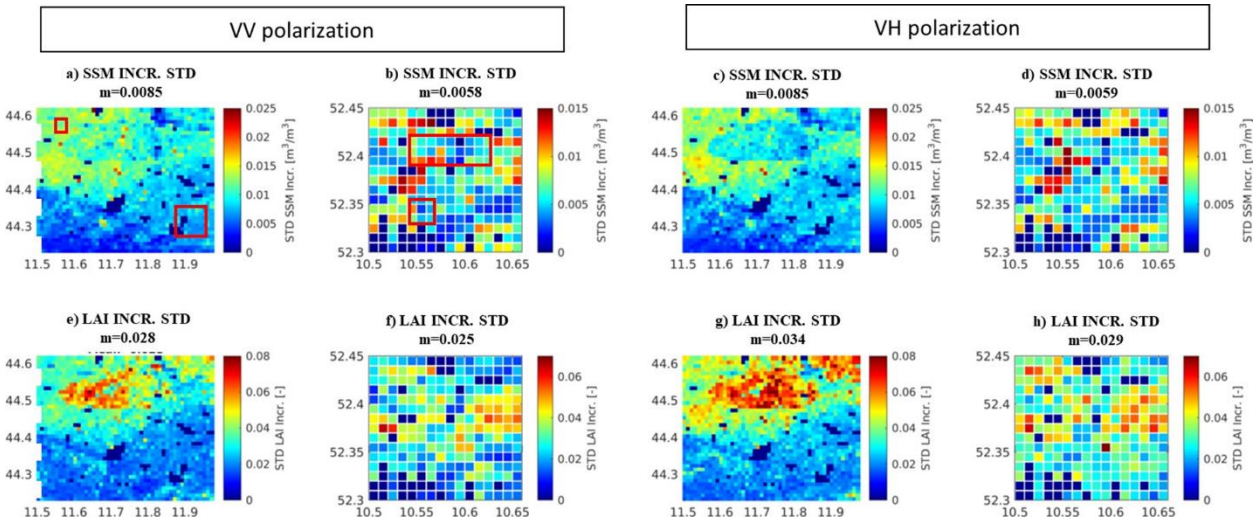

Figure 4.6. Maps of the standard deviation (STD) of the O-F residuals for: a) Sentinel-1 γ^0 VV DA in Italy; b) Sentinel-1 γ^0 VV DA in Germany; c) Sentinel-1 γ^0 VH DA in Italy; d) Sentinel-1 γ^0 VV DA in Germany. m is the mean over the entire study area. The reference period is January 2015-December 2020. In each plot, the x- and y-axes represent longitudes and latitudes in degrees east and north, respectively.

However, the standard deviation of the analysis increments provides valuable information which has been summarized in Figure 4.6. Maps of SSM (Figure 4.6a-d) and LAI (Figure 4.6e-h) show generally small increment standard deviations for both DA experiments and both the study areas. Note that zero standard deviations are found where no data were assimilated (see Figure 4.4i-l). For both areas, complementary patterns are observed for SSM and LAI increments. Larger SSM variances can be observed over the cropland area characterized by sandy soil (e.g., north-west in Italy) and where a higher number of observations are assimilated (especially in Italy), whereas larger LAI updates are related to the silty-loam soil type (e.g. ellipsoid-shaped area in Italy), corresponding to the patterns in O-F (not shown, but the pattern of standard deviations of normalized O-F in Figure 4.5 is similar to that of O-F). This is particularly true for the Sentinel-1 γ^0 VH DA experiment.

Although the DA diagnostics show satisfactory results in terms of consistency of the system, input parameters, such as soil texture and vegetation (i.e., lack of dynamic crop maps in the model) seem to have a strong impact on the performance of the DA systems. In this context, the red squares in Figure 4.5a-b and Figure 4.6a-b show areas where the test sites are located. In Italy

(Figure 4.5a or Figure 4.6a) the Budrio test site (north-west square) is placed over an area where results are close to optimal in terms of standard deviation of normalized O-F. On the other hand, the Faenza test site shows a certain overestimation of the actual observation error (south-east square in Figure 4.5a). In any case, although influences related to the mentioned input data are present, overall, the results are acceptable and near-optimal over both the Italian and German test sites.

4.2.2 Noah-MP evaluation: DA vs OL

In this section results of the DA and OL runs are shown in terms of SSM, LAI, ET and irrigation. We first discuss the Italian pilot site, where the longest record (2-3 year) of benchmark data is available for 3 test sites with different spatial extents. This allows us to focus on the impact of the spatial scale on the performance of the DA system. Next, we discuss the pilot site in Germany where the availability of 1 year of data for 49 irrigated fields (24 LIS pixels, of which only 8 were selected considering a percentage of irrigated area larger than 25%) allows for a statistical interpretation of the results.

4.2.2.1 Italy

Figure 4.7 shows an example time series of SSM, LAI, ET and irrigation at the Budrio farm for the OL and Sentinel-1 γ^0 VV DA experiment, including a comparison in terms of γ^0 observations and forecasts. Also shown are the reference data of ASCAT SSM, PROBA-V LAI and MODIS ET observations at daily time scale. For irrigation, the benchmark reference data, OL and DA output are aggregated to a bi-weekly time scale.

The irrigation simulations (Figure 4.7e) show a general deterioration of the performance with DA, with a decrease in Pearson-R from 0.78 (OL) to 0.65 (DA). However, the DA run provides better results in terms of irrigation quantities, with accumulated benchmark irrigation equal to 917.2 mm against the 842.5 mm of the DA run (as compared to the large overestimation provided by the OL run with 1220.1 mm). Figure 4.7e additionally shows the time series of rainfall from rain-gauge observations and MERRA-2 forcing (upper axes). It is worth noting that the precipitation from MERRA-2 during the summer is typically less than in situ rainfall and this aspect could also

contribute to create underestimations in irrigation simulation, which is partly corrected by the Sentinel-1 γ^0 VV DA.

Figure 4.7b shows the impact of DA in the SSM dynamics during both the summer and winter seasons. The Sentinel-1 γ^0 corrects a dry winter bias that is observed in the OL run SSM time-series, while during the summer the increments affect mainly the short-term dynamics. The LAI time-series are less affected by the ingestion of Sentinel-1 during the growing season (Figure 4.7c) than SSM. The larger updates in terms of SSM are also reflected in a larger improvement in terms of Pearson-R for SSM as compared to LAI: for SSM, the Pearson-R increases from 0.74 for the OL to 0.78 for the DA, while for LAI (Figure 4.7c) the increase in Pearson-R is smaller (from 0.69 to 0.71). This is also explained by the results shown in Figure 4.7a where the daily WCM γ^0 VV forecast time-series are compared with Sentinel-1 observations: it is worth noting that the soil contribution in both the simulated and observed γ^0 signal is much higher than the vegetation contribution, confirming what was highlighted in previous studies (i.e., Bauer-Marschallinger et al., 2018; Modanesi et al., 2021; Wagner et al., 2013). By design, the DA run provides better agreement (Pearson-R=0.81) between the WCM forecasts and Sentinel-1 observations than the OL run (Pearson-R=0.67).

When comparing the ET results against MODIS ET, a general improvement is observed when DA is performed (Figure 4.7d; Pearson-R increases from 0.69 to 0.72), and a general overestimation in the model outputs was observed for both the OL and DA runs over the late summer months (from July to October of each year). The general decrease of MODIS ET during the late summer is not explained by the irrigation benchmark time series reported in Figure 4.7e, and shows a dubious response to irrigation events. This highlights possible uncertainties related to reference ET observations or benchmark irrigation data, and we believe that in this case the ET estimates are the least reliable.

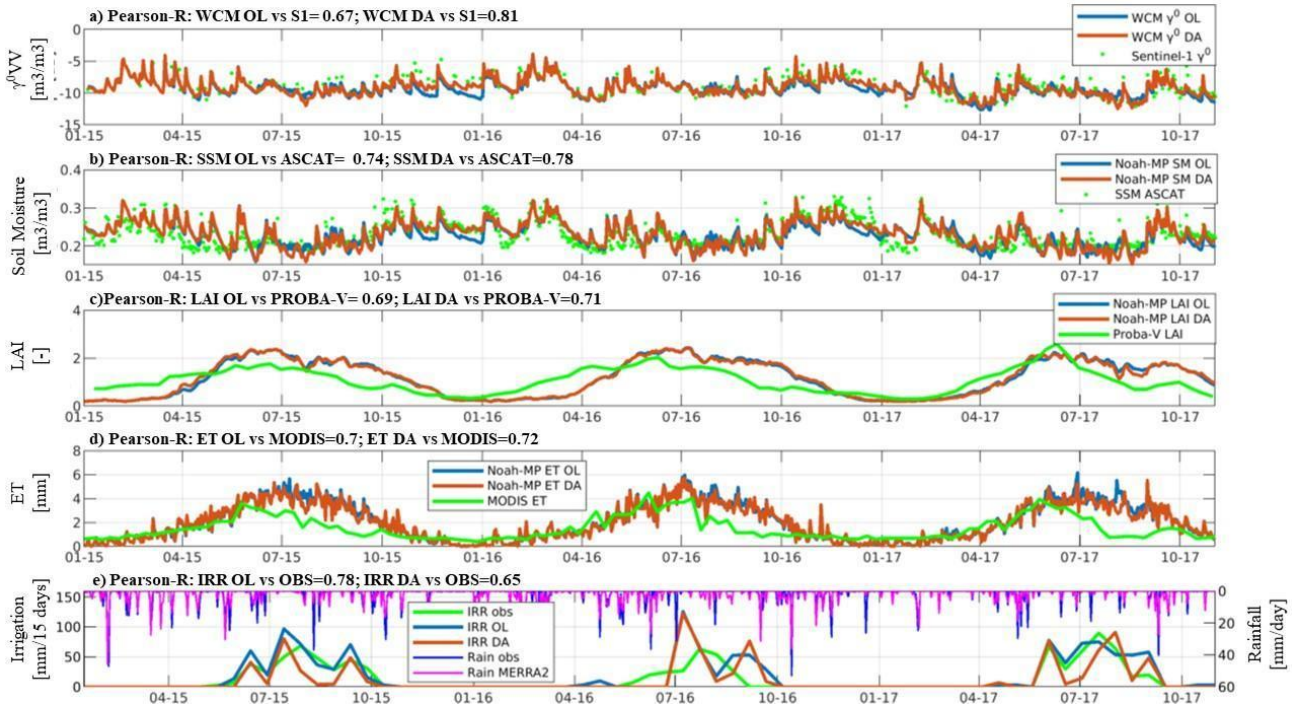

Figure 4.7. Evaluation of the OL (blue lines) and DA (orange lines) results at the Budrio test site for the Sentinel-1 γ^0 VV DA experiment: a) Sentinel-1 γ^0 VV against WCM γ^0 VV; b) ASCAT SSM against simulated SSM; c) PROBA-V LAI against simulated LAI; d) MODIS ET against simulated ET; e) Irrigation benchmark against simulated irrigation, with an indication of MERRA2 and in situ rainfall estimates.

Table 4.2 summarizes the results obtained for the 3 test sites within the Italian pilot site. For the Faenza sites, the results are first spatially aggregated over 3 or 8 pixels before computing time series metrics. The uncertainty in the reference data and the relatively short data records prevent a statistically significant evaluation, but overall, the DA runs provide a slight improvement of SSM and LAI for both the DA experiments compared to the OL run. As expected, Sentinel-1 γ^0 VV DA provides better results in terms of SSM temporal dynamics while the Sentinel-1 γ^0 VH DA shows larger improvements for LAI and ET. These findings confirm that γ^0 VV contains more information about SSM (Bauer-Marschallinger et al., 2018; Modanesi et al., 2021; Wagner et al., 2013), whereas γ^0 VH is more related to vegetation (LAI) (i.e., Macelloni et al., 2001; Vreugdenhil et al., 2018). Due to the effect of LAI and SSM on plants transpiration, ET is also minimally improved. In terms of irrigation temporal dynamics, the DA experiments slightly deteriorate the temporal dynamics for all the test sites but reduce the bias in the irrigation estimates.

Table 4.2: Evaluation results at all the Italian test sites and for both the DA experiments.

ITALIAN TEST SITES	Benchmark period	Model run	SCORE					
			SSM Pearson-R [-]	LAI Pearson-R [-]	ET Pearson-R [-]	Irrigation Pearson-R [-]	Irrigation Bias [%]	Irrigation Amount [mm]
Budrio	2015-2017	OL VV	0.74	0.69	0.70	0.78	33.00	1220.10
		DA VV	0.78	0.71	0.71	0.65	-8.10	842.50
		OL VH	0.74	0.69	0.70	0.79	33.00	1220.00
		DA VH	0.76	0.72	0.72	0.55	-20.60	842.50
		Benchmark	/	/	/	/	/	917.20
Faenza F1	2016-2017	OL VV	0.78	0.73	0.65	0.9	121.90	753.60
		DA VV	0.81	0.74	0.66	0.75	54.36	524.10
		OL VH	0.78	0.73	0.65	0.9	121.90	753.60
		DA VH	0.79	0.76	0.67	0.64	26.32	428.92
		Benchmark	/	/	/	/	/	339.50
Faenza F2	2016-2017	OL VV	0.78	0.86	0.79	0.88	115.20	751.00
		DA VV	0.80	0.86	0.8	0.86	83.60	641.00
		OL VH	0.78	0.86	0.79	0.88	115.20	751.00
		DA VH	0.79	0.87	0.81	0.80	51.26	528.00
		Benchmark	/	/	/	/	/	349.00

Figure 4.8 summarizes the Pearson-R and bias scores for the irrigation simulations for all experiments, and for the 3 Italian test sites. Even though DA always reduces the R-values compared to those of the OL, Figures 4.8a and 4.8c suggest that the R-values for the DA experiments increase when moving from the small area of Budrio (1 LIS pixel) to Faenza F2 (8 LIS pixels), and that the skill reduction introduced by DA is only marginal for the largest Faenza F2 field. An explanation could be related to the spatial mismatch between the 1-km Sentinel-1 signal and the small Budrio fields (~2 ha in total) together with to the poor model ability to reproduce stakeholder's decisions (i.e., irrigation timing) in areas extended over few ha, such as in Budrio.

Even though DA deteriorates the irrigation results in terms of R, it improves the results in percentage bias (Figures 4.8b and 4.8d). In general, the Noah-MP LSM overestimates irrigation over all the test sites in the OL run. Here, the Sentinel-1 γ^0 VH DA provides more reliable irrigation quantities. We think this could be attributed to the ability of the Sentinel-1 γ^0 VH to introduce stronger updates in LAI, which is more linked to RZSM under well-developed crops than SSM (Modanesi et al. 2021). Results in terms of bias show another important aspect: although many limitations in the simulation of the irrigation dynamics are related to the spatial scale, the

quality of the benchmark irrigation data also has an important impact. For a small site such as Budrio, irrigation benchmark is expected to be more precise, explaining lower biases in terms of irrigation quantities.

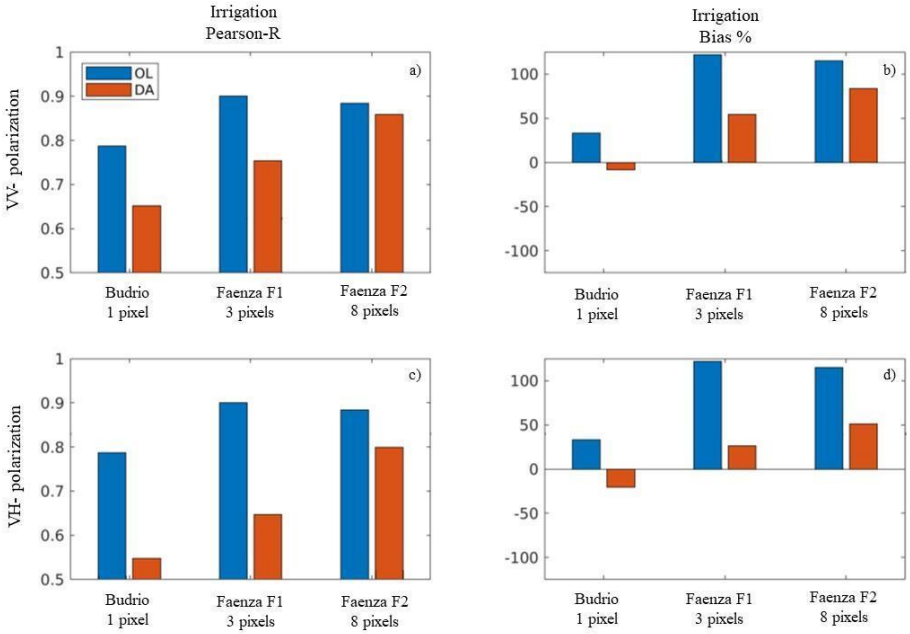

Figure 4.8. Evaluation results in terms of irrigation simulations for the three Italian test sites based on the extent of the fields in terms of LIS pixels. Blue bars refer to the OL run while orange bars refer to the DA run. The Pearson-R values are reported for: a) the Sentinel-1 $\gamma 0$ VV DA; and c) for the Sentinel-1 γ^0 VH DA experiments. (b,d) Same as (a,c), but for percentage bias.

4.2.2.2 Germany

In the Niedersachsen test site, the evaluation in terms of SSM and LAI using ASCAT SSM and PROBA-V LAI (not shown) does not display substantial differences in terms of Pearson-R between the OL and the DA runs (median Pearson-R equal to ~0.8 for SSM and ~0.7 for LAI, across 8 pixels). Regarding irrigation estimates, Figures 4.9a and 4.9b display the Pearson-R and percentage bias distributions over the 8 selected irrigated pixels for the OL and the Sentinel-1 γ^0 VV DA experiment, while Figures 4.9c and 4.9d refer to the Sentinel-1 γ^0 VH DA. In particular, Figure 4.9a and 4.9c show improved irrigation estimates for both Sentinel-1 γ^0 VV DA (Pearson-R increases from 0.47 to 0.61) and Sentinel-1 γ^0 VH DA (Pearson-R increases from 0.47 to 0.65).

Unlike the Italian site, the Niedersachsen site suffers from an irrigation underestimation by the model, in line with a previous study by Zappa et al. (2021) which used Sentinel-1 SSM retrievals

to detect and quantify irrigation at the Niedersachsen test site. Figure 4.9b shows that the median bias is reduced from a value of -40.8% for the OL to a value of -24.6% for Sentinel-1 γ^0 VV DA and Figure 4.9d shows a reduction from -40.8% for OL to -7.6% for Sentinel-1 γ^0 VH DA. Despite the improvement in median values for the bias, the overall distribution of the bias is wider than for the OL. Reasons for that might be related to the specificity of the different fields and the difference in the performance for different spatial scales (see section 4.2.2.1) when different fields of different size are bulked altogether. Beyond this, also the consistency between simulated backscatter by the coupled Noah-MP-WCM and Sentinel-1 data for some specific pixels might exert a role in spreading the distribution of the bias with respect to the OL. The latter can be caused by both poor model performance (due to the quality of the forcing, model parameters and static maps) and the quality of the Sentinel-1 γ^0 data.

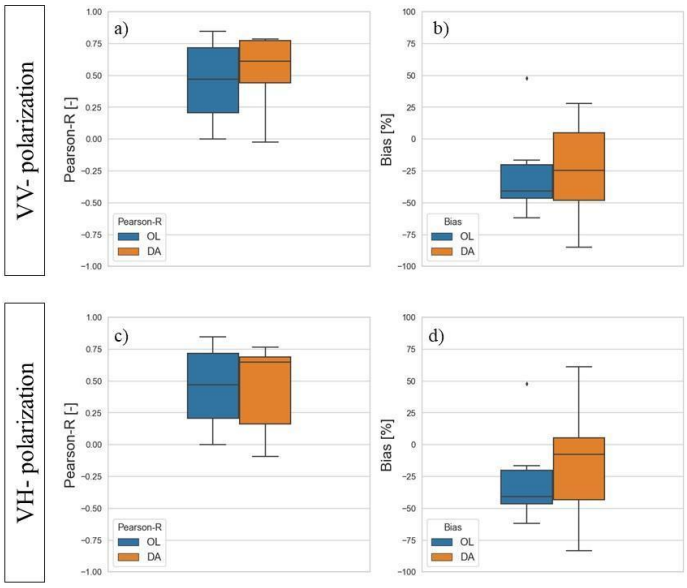

Figure 4.9. Evaluation in terms of (left) Pearson-R and (right) percentage bias of irrigation simulations for the German test sites, containing the 8 irrigated LIS pixels with percentage irrigated area larger than 25%. Blue bars refer to the OL run while orange bars refer to the DA run, with (a-b) the Sentinel-1 γ^0 VV DA and (c-d) for the Sentinel-1 γ^0 VH DA.

4.3 Discussion

4.3.1 Data assimilation

In this study a DA system was built for the ingestion of Sentinel-1 γ^0 both in VV and VH polarization into the Noah-MP LSM in order to test the ability of Sentinel-1 γ^0 to improve irrigation quantification through the update of both SSM and LAI. The regional scale analysis of internal DA diagnostics provided evidence that the DA system is self-consistent and near-optimal. Local deviations from desirable reductions in ensemble spread or from optimal O-F statistics, or higher absolute SSM or LAI increments were mainly related to poor input data to the Noah-MP LSM. Confirming what was previously found in Modanesi et al. (2021), soil texture uncertainties play an important role in reducing (or increasing) the effectiveness of the DA system. This is because the soil texture affects the RZSM and FC, which contribute to the activation of the irrigation scheme. The silty-loam soil texture generally shows a reduced variability in the soil moisture dynamics as compared to more sandy textures, providing lower amount of irrigation, especially over wetter climates (i.e., Germany). Assuming that the Sentinel-1 γ^0 contains information on irrigation, the DA system should correct poorly simulated irrigation, e.g. due to poor input parameterization or errors in MERRA-2 precipitation input as compared to observed precipitation (which was observed in the evaluation over the Italian test sites). However, this seems to be challenging in our experiments. Another important factor that influences regional DA diagnostics is the irrigation fraction information. This information was lacking in the GRIPC input for the pilot site in Germany, which forced us to simulate irrigation only over pixels where known irrigated fields were located, notwithstanding that also other cropland pixels could be irrigated, especially during the drier conditions that affected the northern countries during the 2018 summer months in northern European countries (i.e., the 2018 north-western Europe drought; Drouard et al., 2019). The standard deviation of normalized O-F higher than unity in the eastern area of the German pilot site could thus be related to the absence of irrigation simulations over areas which are actually irrigated. The lack of updated irrigation fraction input at global scale is still a strong limitation, although many studies have focused on

monitoring irrigated lands worldwide in the last decade (Ambika et al., 2016; Bazzi et al., 2020; Dari et al., 2020; Gao et al., 2018).

In the test site analysis, we focused on three different aspects: i) the added value of the DA experiments compared to the OL runs and the role of the Sentinel-1 γ^0 polarization; ii) the limitation of the Noah-MP parameterization and, more generally, of the DA system in improving irrigation simulations; and finally, iii) the spatial scale difference between the irrigation benchmark and irrigation simulations.

In Italy, we found an improvement due to DA in terms of SSM, LAI and ET, compared against RS retrievals (i.e., ASCAT SSM, PROBA-V LAI and MODIS ET). Sentinel-1 γ^0VV DA provided a larger contribution to SSM performances whereas Sentinel-1 γ^0VH DA improved mostly the vegetation and vegetation-related states (LAI and ET). This could be expected based on previous literature (i.e., Bauer-Marschallinger et al., 2018; Vreugdenhil et al., 2020, 2018) and the previous study by Modanesi et al. (2021) over the Italian test sites. Our findings also showed how the Sentinel-1 γ^0 VV DA has a larger impact on the temporal dynamics of irrigation, whereas the VH polarization has a stronger influence in adjusting the bias due to the high sensitivity of the vegetation to RZSM and vice versa (Modanesi et al., 2021).

Following the rationale that weather forecasts would be improved if land surface conditions are better constrained, the hope was to also improve irrigation forecasts with better constrained land surface conditions. However, the latter is only true if the assumption holds that the irrigation model produces the best irrigation estimates for the best estimates of land surface state variables. The latter assumption strongly depends on a good characterization of soil, vegetation and irrigation parameters which was found to be a limitation for the DA system. For instance, the OL run provided a large overestimation or underestimation of the irrigation quantities (depending on the study area) that can be attributed to limited parameterization of the irrigation scheme like for instance, detailed information on irrigation fraction input, dynamic crop rotation and rooting depths, as well as a poor description of the crop phenology in Noah-MP. The DA experiments helped in reducing the irrigation overestimation (or underestimation) at some, but not all, sites. This means that, if the sprinkler irrigation scheme is not well parameterized, the DA system is

not able to strongly correct the OL runs. In case of biased state variables or flux simulations, it is generally more interesting to study the effect of DA on anomalies from (multi-year) climatological conditions, but such an analysis could not be performed with the limited amount of available benchmark data.

The limited spatial coverage and scale of the benchmark data is another reason of concern in the evaluation of the DA results. The Sentinel-1 DA appears to degrade the temporal dynamics (Pearson-R) of the bi-weekly irrigation estimates relative to the OL, when compared to small-scale (Budrio) benchmark. This can be explained by the spatial mismatch between the 1-km Sentinel-1 signal (which can include multiple fields irrigated at different times) and the irrigation information related to the small Budrio fields. However, this degradation is not significant or not found, when the simulations at multiple LIS pixels are aggregated (Faenza) or the statistics for multiple sites are lumped (Niedersachsen), respectively. In Germany, the median Pearson-R over the irrigated pixels increased especially for the Sentinel-1 γ^0 VV DA experiment, and a reduction of the median bias was found for the Sentinel-1 γ^0 VH DA experiment.

4.3.2 Limitations and shortcomings

The evaluation highlighted many aspects that can be improved for a more reliable irrigation estimation in a DA system which involves the Noah-MP LSM, with an irrigation scheme and innovative Sentinel-1 γ^0 observations. Although good results were obtained in terms of average DA diagnostics, it should be noted that the system is influenced by errors from the LSM, the irrigation scheme and the observation operator, which can interact and compensate each other providing suboptimal assimilation results. Based on Modanesi et al., (2021) the best unbiased WCM parameters were obtained, but a single parameters set was used for each model grid cell regardless of the crop type year variability. Especially over the Po Valley, agricultural practices are characterized by crop rotation and the different structural effects of crop types on γ^0 observations can lead to an interannual variability that is only partly represented by SSM and LAI, and that could deteriorate model estimates (i.e., irrigation) in the DA runs. Additionally, the Sentinel-1 γ^0 data show slightly different statistics for different orbits and their combination results in a reduction of the signal-to-noise ratio, impacting time series analysis. We think that

the inclusion of dynamic crop information (even at 1 km spatial resolution and not at field scale) and the assimilation of γ^0 data per orbit would improve the results and this is a future step of this work that we are currently investigating.

In terms of irrigation simulations, we found that absolute irrigation amounts and timing of irrigation estimated by the irrigation scheme strongly depend on soil (e.g., texture), vegetation (e.g., crop type) and irrigation (e.g., 'intensity' or area fraction) parameters. These parameters are now based on global datasets that might not be ideal for regional to local applications, being not dynamic and updated. Likewise, irrigation estimates depend on a correct representation of natural forcing input, here re-analysis data, which is unlikely to be accurate at the local scale (where the weather is itself influenced by irrigation).

Furthermore, the irrigation estimates obtained with inclusion of DA are not always outperforming the model-only estimates. The main reason is that the irrigation model does not necessarily produce the best irrigation estimates for the best estimates of land surface state variables at the test sites due to uncertainties in irrigation parameterization or difficulties in reproducing farmer's decision. Thus, in line with the suggestions by Lawston et al. (2017), besides optimizing the DA itself, future research should also focus on improving the irrigation model to optimally use the observational information contained in the Sentinel-1 γ^0.

Another important aspect is related to the temporal and spatial variability of irrigation. We found that irrigation results become increasingly uncertain (and depend more on the irrigation parameterization) at shorter, e.g., daily, timescales. Soil moisture and vegetation increments can indeed affect the irrigation dynamics at short-term periods (i.e., daily time scale), and the benchmark data are also not representative of the effective irrigation needs at the short-term because of water management policies. It can be expected that the interannual variability in irrigation can be better estimated, as also suggested by Lawston et al. (2017). Furthermore, we found that the agreement between benchmark data and simulations of irrigation quantities increases in an analysis at pixel-level or at small-district spatial scale (Italy), showing the limitation of the system in providing information at plot scale, when simulations and RS observations are provided at coarser spatial resolution (i.e., 0.01°).

Three last aspects need to be highlighted: i) a robust evaluation analysis of land surface variables is not straightforward considering that RS observations at coarse spatial resolution (i.e., ASCAT) or constrained by reanalysis data (i.e., MODIS ET) do not necessarily provide accurate information on irrigation (Zaussinger et al., 2019); ii) additionally, evaluating irrigation estimates is also more challenging due to the scarce availability of information on the irrigation management (Massari et al., 2021); and iii) finally, the disagreement between in situ reference data and irrigation estimates obtained from the model-only or DA system can be also partly explained by the actual in situ irrigation system management, which depends on water availability and policies unknown by the modelling system. Although irrigation data are compared at bi-weekly time scale and DA is overall expected to improve the simulation of irrigation temporal dynamics, the temporal resolution of the Sentinel-1 backscatter (~3 days over the study areas) could imply to miss irrigation events and affect the results.

4.4 Conclusions

Information on the actual irrigation quantities used for agricultural purposes is still missing and a correct quantification of irrigation is a challenging topic. The joint use of models and EO observations (which contain irrigation information) can help to fill this gap, while also providing irrigation estimates at high temporal scale and medium-high spatial resolution.

In this study we assimilated, in two different experiments, 1 km Sentinel-1 γ^0 VV and VH polarization into the Noah-MP LSM, equipped with a sprinkler irrigation scheme, for the joint update of soil moisture and vegetation state variables. The main research question focused on testing if irrigation water amounts, simulated by the irrigation scheme, can be optimally estimated when optimal soil moisture and vegetation estimates are available through DA. Additionally, we aimed at: i) testing the consistency of the DA system; ii) the effects of DA on irrigation and model states predictions with a specific focus on differences due to the ingestion of Sentinel-1 γ^0 in co- or cross-polarization; and finally, ii) unveiling the limitation of the system in terms of input parameters, DA shortcomings, spatial scale analysis and benchmark uncertainties.

The main conclusions drawn from our evaluation highlight shortcomings of the system and can be summarized as follows:

- The developed DA system is consistent and close to optimal, but it could benefit from enhanced model inputs, such as more reliable soil texture maps or the introduction of dynamic and high-resolution crop maps which could improve both soil moisture and vegetation simulations (input for the WCM calibration). Additional effort will also be needed in future research to account for different Sentinel-1 orbits, both in the WCM calibration and in the DA system, which will provide a gain of the signal-to-noise ratio with a general benefit in time series analysis.
- The Sentinel-1 γ^0 observations contain useful information about SSM and LAI over irrigated areas, confirming Modanesi et al. (2021), and the γ^0 polarization has a considerable influence on the DA results. For instance, the Sentinel-1 γ^0 VV DA mainly improves temporal dynamics of SSM and irrigation, whereas the Sentinel-1 γ^0 VH DA seem to have a stronger influence on vegetation and in adjusting negative/positive bias due to the high sensitivity of the vegetation to RZSM (and vice versa).
- The Noah-MP LSM input and irrigation parameterization affect the OL and DA estimates, providing strong over- or underestimations of irrigation, depending on the study area. Those limitations are mainly related to soil texture uncertainties, lack of crop type inputs and outdated irrigated fractional area information which affect the results of the reference OL run. In this context, the DA can only correct the estimates of irrigation amounts, if the irrigation simulation is not excessively biased, meaning that future research should focus on improving the irrigation model. Alternatively, even with biased irrigation simulations, the DA should be able to correct for the interannual variability in irrigation estimates, but the record of available benchmark data on irrigation is insufficient at this time to confirm this hypothesis.
- When comparing irrigation simulations and benchmark data, the spatial and temporal resolution play an important role. Irrigation estimates were here evaluated at a bi-weekly scale, to limit the influence of short-term analysis increments on the activation of the irrigation scheme, and to reduce mismatches with benchmark data due to human choices

in the timing of irrigation application. In any case, results in terms of temporal dynamics and bias could also be partly affected by the temporal resolution of Sentinel-1 observations (~3 days) which could miss some daily irrigation events. Additional improvements could be obtained in DA analysis with higher-temporal resolution products as also demonstrated by Azimi et al. (2020). Furthermore, the evaluation in terms of irrigation quantities provides better results when irrigation benchmark data and the model have a similar spatial resolution. Evaluation is generally difficult due to the scant reporting of irrigation and extra uncertainty can derive from the reliability of in situ irrigation estimates.

- Finally, we want to highlight the important role of RS reference observations in the evaluation of DA results. The coarse resolution and retrieval uncertainties of satellite SSM products and the dependency of MODIS ET on ancillary data (i.e., reanalysis product), can reduce their ability to detect irrigation over small test sites or over areas which are not irrigated as extensively as the Po Valley.

Chapter 5: Conclusions and outlook

This Chapter concludes this PhD thesis by summarizing the key findings and main contributions of this study, based on the research questions described in Chapter 1. New scientific findings, limitations and weaknesses highlighted during this three-years activity will be summarized and finally outlooks for future research will be discussed, based on the obtained results.

This thesis explored the utility of a new generation of EO data to monitor agricultural droughts and to help models account for the effects of anthropogenic activities on the water cycle, particularly from an agricultural perspective. It linked the effects of the water scarcity to crop production and to the current need to provide reliable estimates of the water actually used for agricultural purposes (i.e., irrigation). To reach those objectives the activity was divided into two parts: 1) a first part focusing on agricultural drought analysis; and 2) a second part – more significant – related to the irrigation quantification through the development of an innovative DA system which ingests high-resolution radar observations into a LSM. Both analyses demonstrated how models (i.e., LSM) alone have difficulties to resolve the water cycle and might miss to reproduce important processes like irrigation.

The agricultural drought analysis in India in the first part of this thesis (Chapter 2) highlighted interesting aspects of the information included in EO data to monitor drought events and to detect human activities. In particular, satellite SSM was found to be more representative of soil wetness conditions and crop productivity than modeled soil moisture and ground-based precipitation data, when applied to develop drought indicators. This highlights the potential of leveraging satellite SSM for operational drought forecasting. Furthermore, even though a relatively coarse-spatial resolution satellite SSM product (~25 km) was used, its closer relation with crop productivity than SSM estimates from models or precipitation over irrigated cropland suggests that the satellite signal contains useful information on irrigation. This was also confirmed by the analysis carried out in the second part of this activity over the Po Valley. Here, coarse-resolution satellite SSM products from SMAP and ASCAT were compared with the SSM from the Noah-MP LSM, equipped with a sprinkler irrigation scheme. The results showed a better agreement between the model and satellite products when irrigation was simulated in Noah-MP.

While useful, coarse-scale satellite products have strong limitations for precision agriculture applications. Therefore, in the second part of the thesis the ability of new higher resolution EO data to correct potentially misrepresented model estimates of key agriculture variables (like soil moisture, LAI, ET) over intensively irrigated areas was explored. In particular, a DA system merging the Noah-MP LSM and 1-km radar backscatter data from Sentinel-1 through an observation operator (being the WCM) was built, calibrated and tested to improve irrigation quantification (Chapter 3 & 4). Unlike classical DA of SSM retrievals, the direct ingestion of MW radar backscatter observations was performed to remove the risk of inconsistent parameters and avoid cross-correlated errors between the model state and satellite retrievals of geophysical variables. Additionally, an irrigation scheme was activated within the LSM with the objective to directly correct irrigation simulation through the update of soil moisture and vegetation state variables, with the goal to improve the initial conditions for subsequent irrigation simulations. To our knowledge this is the first high-spatial resolution study which developed this type of approach. The backscatter DA introduced both improvements and degradations in irrigation estimates as well as in other LSM variables (i.e., soil moisture, LAI and ET). The results also highlighted the key-role of the spatial and temporal scale on the analysis. Ultimately, the DA experiments carried out over two highly irrigated European regions revealed a good potential of Sentinel-1 MW observations to improve LSM variables and irrigation estimates but also rose several issues:

- In situ data have a key role in both the agricultural drought analysis and in the irrigation quantification analysis. Crop yields and irrigation benchmark data are often not available (unless regional-national aggregated scale is considered) for an assessment of agricultural drought indices and to test the goodness of LSM simulations (i.e., irrigation estimates) respectively. Particularly, there is a real challenge to obtain reference irrigation data for two main reasons: i) the limited availability of measurements (applied irrigation volumes are often not measured); and ii) hesitance to share information about water consumption at the plot- or small-district scale. Note that, a decision to irrigate or not is commonly driven by management, economic and societal reasons instead of soil wetness or crop conditions (i.e., Foster et al., 2020; Massari et al., 2021) – another aspect that reduces the

ability of models in reproducing irrigation. In this context, two types of problems can arise: the evaluation of LSM simulations is affected by the availability or reliability of benchmark data, and models that parameterize human activities are not able to reproduce the correct timing and amounts of irrigation.

- Both the agricultural drought and irrigation quantification research activities demonstrated how models might fail to provide valuable information on irrigation. This is because they typically use unrealistic soil texture maps (e.g., too coarse with respect to the scale of agricultural applications), static land cover and crop type information and too simple irrigation parameterization schemes. Despite the valuable information contained in Sentinel-1 backscatter data (see Chapter 3), attempting to correct these issues with DA is difficult, because models are biased and produce results that are too far from reality. So, prior to DA a maximal effort should be put in improving open loop LSM simulations by using the best available ancillary data. For instance, accounting for dynamic crop maps from EO data could provide a substantial improvement of irrigation simulations, and thus make the successive DA problem better posed (by reducing the chance of unrealistic and biased surface states and fluxes). The spatial and temporal resolution of LSMs input and satellite products are additional key aspects when applied to field-scale agriculture analysis. High-temporal resolution EO data (i.e., daily revisit time as compared to ~3 to ~6 days of Sentinel-1) could improve the results in terms of irrigation quantifications and thus increase the probability to capture irrigation events. From the agricultural drought analysis point of view, 1-km satellite products are preferred but additional limitations can derive from the lack of long-term records of satellite soil moisture from relatively new satellite missions. From a LSM perspective, an analysis at 1-km spatial resolution or at district scale seems to improve the description of the hydrological cycle, but contradicting results are obtained for a detailed study at the plot scale. In this context, improving the modeling analysis in terms of spatial resolution is not straightforward given the lack of high resolution input data (i.e., forcings).

- The DA system could benefit from an improvement by accounting for different Sentinel-1 orbits in both the WCM calibration and DA. Currently, by design, the orbit bias correction applied to Sentinel-1 backscatter processing (Lievens et al., 2019) rescales the first two order moments (temporal mean and standard deviation) such that time series for all orbits have the same mean and standard deviation. Seasonally varying deviations between orbits, that e.g. originate from vegetation effects at different incidence angles, remain present in the time series for the different orbits. In this context, we assume that (i) a calibration that takes into account the incidence angle of each orbit in the WCM or (ii) a per-orbit WCM calibration with consequent improvement of the DA system through per-orbit ingestion of the Sentinel-1 could provide help to improve the backscatter DA performance. This aspect involves further developments in the LIS framework and deserves more research in the future. Additionally, separating the contribution of the soil and vegetation in the backscatter is challenging when the vegetation is well developed and further complicated by poorly-simulated vegetation of Noah-MP. We found different issues which prevented an optimal calibration of the WCM. Future research should consider the use of more sophisticated backscatter operators (also assisted or replaced by machine learning) and the use of vegetation descriptors directly from EO data to avoid the influence of suboptimal model parameterization.
- Finally, the assimilation of backscatter data only is likely not sufficient to improve irrigation estimation. Recent studies demonstrated how collecting irrigation information using multiple RS techniques (i.e., thermal, optical and MW observations) can be advantageous. For instance, Lei et al. (2020) demonstrated that incorporating satellite-based thermal infrared (TIR) imagery and radar information into a soil-vegetation-atmosphere-transfer (SVAT) model through DA could provide spatially high-resolution (less than 100 m) soil moisture maps to optimize irrigation allocation. Indeed, satellite-based SSM provides information on the first cm of the soil and if vertical coupling of soil layers is weak the DA system will have few chances of updating RZSM (Chen et al., 2011; Lievens et al., 2015). On the other hand, over densely vegetated areas, soil moisture TIR-based estimates (e.g., derived from the ratio of actual-to-potential ET) could better

represent soil moisture conditions within the entire effective vegetation rooting zone (Fang et al., 2016). This could lead to a better representation of the RZSM, which directly affects vegetation health and irrigation applications.

The limitations found in this activity allow us to focus on outlooks, future challenges and developments that will be needed to improve the analysis and to provide a better description of the water cycle.

5.1 Importance of ground and EO data in irrigation information retrieval

Collecting reliable irrigation reference data is crucial to support further development of irrigation estimates from satellite retrievals, modeling and DA analysis. In this context, it is worth mentioning that this research was also conducted in the framework of the Irrigation+ project (https://esairrigationplus.org/), funded by ESA. The project which aims at exploring, developing and validating advanced EO-based algorithms for retrieving information on irrigation from field to regional/global scale, is now at its final stage providing large-scale science cases analysis and demonstration cases. The project planned activities to collect a huge amount of data over the Ebro basin within the HyMeX (HYdrological cycle in the Mediterranean Experiment) LIAISE campaign which will provide meteorological data, surface energy budget data, soil moisture, land surface temperature and reference irrigation data. Testing the system over such an instrumented area would allow to overcome some of the issues related to missing reference data for evaluation and to have a better control on the experiments.

The collection of reference data should ideally not be limited to some test areas selected for research projects. Despite this, regional or global detailed information on irrigated lands and on the volumes of water withdrawn for irrigation practices is generally poor or lacking. Currently, existing data sets containing irrigation information (such as the Global Map of Irrigated Area (GMIA) developed by the Food and Agriculture Organization (FAO) of the United Nations (Siebert et al., 2015) or the Global Rainfed and Paddy Cropland (GRIPC; Salmon et al., 2015)) only show areas equipped for irrigation (AEI) and almost no spatial information of real water volumes used for irrigation. On the other hand, European statistics only provide annual volumes of irrigation water for some European countries and some years (the reader can refer to

https://www.europarl.europa.eu/RegData/etudes/BRIE/2019/644216/EPRS_BRI(2019)644216_EN.pdf for further details) so they are of little utility to study spatial and temporal irrigation patterns as well as to grasp relationships between irrigation and environmental and societal factors on a local scale. Reference ground-truth data also, despite ideal to validate irrigation retrieval, will never be available all the time for all locations on Earth. In this respect, satellite data can be used as alternative validation datasets and to extrapolate knowledge gained at the local scale to larger scales.

Future satellite missions are expected to widen our opportunities to better estimate vegetation, evaporation and soil moisture at higher spatial resolutions and thus provide an indirect way to understand if a certain area is irrigated and, more importantly, how much it is irrigated (see Massari et al., 2021). For instance, one of the most innovative missions for vegetation monitoring, planned to be launched by 2025, is represented by the FLuorescence EXplorer (FLEX) mission which will fly in tandem with the Copernicus Sentinel-3 mission, working in combination with the Ocean and Land Color Instrument (OLCI) and Land Surface Temperature Radiometer (SLSTR). FLEX will provide global maps of vegetation fluorescence that will reflect the plants photosynthetic activity as well as plant health and stress and that could be directly linked to irrigated crops. The exploitation of these new data will require advancements also for the vegetation modeling perspective as, to make them ready to ingest fluorescence data, they should at least dynamically simulate vegetation (as Noah-MP already does). Other future planned missions such as TRISHNA (Lagouarde et al., 2019) or the ESA land surface temperature monitoring (LSTM) will also provide enhanced high spatial-temporal resolution LST which could be used in synergy with other EO as mentioned earlier (Lei et al., 2020) with the aim to improve RZSM and evaporation even over small irrigated areas.

On the microwave side, high resolution backscatter data will benefit from the launch of Sentinel-1C and Sentinel-1D satellites that will extend the Sentinel-1 monitoring system, at least until the end of 2030, providing a long term record of radar observations that could be used for precision agriculture and irrigation monitoring. Additionally, the future launch of the US-Indian NASA-ISRO SAR (NISAR) and Radar Observing System for Europe—L-band (ROSE-L) SAR missions

(https://nisar.jpl.nasa.gov/system/documents/files/26_NISAR_FINAL_9-6-19.pdf), planned to be launched in 2022 and 2028, are expected to provide improved observations of soil moisture given the better penetration depth and the less sensitivity to vegetation of L-band observations (as compared to Sentinel-1 products in C-band).

As previously mentioned, higher temporal resolution is also needed to improve DA and irrigation information retrievals. In this context, a new era of small, lightweight satellites represented by the low-cost constellations of CubeSats is a future opportunity for hydrological sciences (McCabe et al., 2017) and a trade-off to optimize temporal and spatial resolution of EO opening new opportunities for high precision agriculture (Aragon et al., 2018).

5.2 Improving models

LSMs offer the opportunity to estimate land surface variables beyond what can be observed, i.e. at times and locations that are unobserved, or variables that are not observed. Irrigation represents one of the most difficult fluxes to model given that it is not only induced by water stress but is driven by economic and societal factors. Therefore, improving model ability to simulate irrigation is one of the most important research challenges that the model community should solve in the future. The improvement of irrigation quantification and estimation of land surface variables requires an additional effort to obtain high-quality LSM parameter input datasets such as: i) soil texture maps; ii) maps of the crop types; iii) updated information on irrigated areas; and iv) information on the irrigation types (i.e., sprinkler, drip, or flood) which affect the daily timing and quantity of irrigation water applied. All this information should be synergistically used within models to provide a more realistic representation of natural and human processes and in order to achieve the ability to provide a faithful digital (hydrological) replica of the Earth (DARTH, Rigon et al., 2022). For this, model and EO communities should have stronger and closer collaborations.

Furthermore, the meteorological input given to LSMs could be refined to better estimate the needs for irrigation. Large-scale re-analysis data are typically of a coarse resolution and are often corrected with local measurements. Such data are thus likely less certain in Africa or South America than over the study areas included in this PhD thesis. Additional structural model

changes are also needed in the next future to account for the actual source of applied water (i.e., surface water or groundwater) which currently do not allow an integrated water resource analysis.

The above discussion focuses on the prognostic LSM and irrigation model. However, the use of satellite data and their conversion to useful geophysical information requires diagnostic radiative transfer models. In this thesis, MW backscatter data were related to soil moisture and vegetation via the WCM, but preliminary results show that machine learning could possibly outperform the WCM. Active MW signals are still not fully understood and further developments of backscatter models would be a good investment for future research.

5.3 Data assimilation

In addition to the improvements needed in model structure, parameters and input data, land surface estimates can be enhanced via state updating through DA. In this thesis, a filtering approach was used, but alternative solutions such as smoothers could be more beneficial for e.g. vegetation updating. While DA experiments that ingest post-retrieval RS observations might be impacted by inconsistencies between model structure and retrieval assumptions, DA of raw MW data also strongly depends on the ability of the observation operator (WCM within this thesis) to represent the physical processes related to emitted or reflected radiations such as the influence of different satellite orbits, soil roughness and texture, vegetation structure, etc. For instance, future analyses of this work will consider the implementation of routines to take into account different satellite (Sentinel-1) orbits, because differences in backscatter statistics for different orbits were found to have an impact on DA results and on the choice of the best way to consider the vegetation descriptor within the WCM calibration (i.e, from model or from satellite observations). This and other issues could be solved via well designed synthetic experiments (planned in the near future).

The DA system developed in this research will be additionally tested and improved in the framework of international research projects such as the ESA 4D-MED project, recently started and led by the CNR-Irpi in a collaboration with different partners, including KU Leuven. The project aims at facing one of the main challenges in hydrological research which is to develop an

advanced, high-resolution, and consistent reconstruction of the Mediterranean terrestrial water cycle and to test the ability of new EO to improve predictions of hydrology extremes (floods, landslides and drought). The system implemented within this doctoral activity will serve as a basis to include the assimilation of multiple EO data next. For instance, the joint assimilation of Sentinel-1 backscatter to update soil moisture and vegetation states together with ingestion of Sentinel-1 snow depth (Lievens et al., 2019) is expected to significantly enhance model simulation of the water cycle. Indeed, an improvement in snow water equivalent simulation will impact the soil moisture after snowmelt. New developments in the project framework will theoretically enhance the water cycle description and the water resources management, in order to create a closer link between science and society via science-based tools compatible with decision making processes.

5.4 Impacts

This research activity has important scientific, technological, economic and societal impacts. A better estimation of the water used for irrigation as well as better estimates of LSM variables are necessary conditions to provide an optimal water management and help in predicting water scarcity conditions. Furthermore, a good management of water abstractions can prevent adverse events such as river degradation, groundwater depletion and human-driven alteration of land uses. From the technological point of view, the implementation of an open source DA system able to produce better estimates of LSM variables in a flexible DA framework, open to further developments, such as the NASA LIS framework can provide a solution for the current fragmentation of tools and services for water resource management (which negatively impacts every water resource management practice). In this context, the structure of LIS allows researchers contributing to future developments of the DA components, addressing this study in the direction of a Digital Twin Earth (DTE) for Hydrology system. As described in Rigon et al. (2022) a DTE should be developed with the final aim to accelerate the transition from fragmented hydrologic DA research towards community-supported and open-source systems that can operate an efficient ingestion of satellite data. In this context, an additional step forward is represented by also taking into account the influence of atmospheric processes, through a coupled

land-atmosphere system. For instance, LIS can be coupled with the NASA-Unified Weather Research and Forecasting (NU-WRF) model as in Lawston et al. (2015).

Finally, on the economic and societal perspective, the objective to realistically characterize the different components of the terrestrial water cycle will help in minimizing future water conflicts within poorly gauged regions of the planet, and in understanding potential environmental human migrations. In this context, the complex links between climate change impacts and its induced environmental human mobility need to be considered. Water scarcity and drought events, declining crop yields and biodiversity, land degradation as well as sea level rise are among the major potential climate impacts that are shifting patterns of migrations (UNEP, 2016; World Bank, 2018). In other words, this approach of this PhD thesis, further corrected for the above-identified limitations and applied over large scale areas, could ensure a better management of water resources to supply food, water and energy security to human needs, especially in developing countries.

Bibliography

Abbaszadeh, P.; Moradkhani, H.; Yan, H.X., 2018 Enhancing hydrologic data assimilation by evolutionary Particle Filter and Markov Chain Monte Carlo. Adv. Water Resour., 111, 192–204.

Abbott, B.W., Bishop, K., Zarnetske, J.P., Minaudo, C., Chapin, F.S., Krause, S., Hannah, D.M., Conner, L., Ellison, D., Godsey, S.E., 2019. Human domination of the global water cycle absent from depictions and perceptions. Nature Geoscience 12, 533–540.Ahmad, L., Kanth, R.H., Parvaze, S., Mahdi, S.S., 2017. Agro-climatic and agro-ecological zones of India, in: Experimental Agrometeorology: A Practical Manual. Springer, pp. 99–118.

Albergel, C., Munier, S., Bocher, A., Bonan, B., Zheng, Y., Draper, C., Leroux, D.J., Calvet, J.-C., 2018. LDAS-Monde sequential assimilation of satellite derived observations applied to the contiguous US: An ERA-5 driven reanalysis of the land surface variables. Remote Sensing 10, 1627.

Amante, C., Eakins, B.W., 2009. ETOPO1 arc-minute global relief model: procedures, data sources and analysis.

Ambika, A.K., Wardlow, B., Mishra, V., 2016. Remotely sensed high resolution irrigated area mapping in India for 2000 to 2015. Scientific data 3, 1–14.

Aragon, B., Houborg, R., Tu, K., Fisher, J.B., McCabe, M., 2018. CubeSats enable high spatiotemporal retrievals of crop-water use for precision agriculture. Remote Sensing 10, 1867.

Arsenault, K.R., Kumar, S.V., Geiger, J.V., Wang, S., Kemp, E., Mocko, D.M., Beaudoing, H.K., Getirana, A., Navari, M., Li, B., 2018. The Land surface Data Toolkit (LDT v7. 2)–a data fusion environment for land data assimilation systems. Geoscientific Model Development 11, 3605–3621.

Attema, E.P.W., Ulaby, F.T., 1978. Vegetation modeled as a water cloud. Radio Sci. 13, 357–364. https://doi.org/10.1029/RS013i002p00357

Azimi, S., Dariane, A.B., Modanesi, S., Bauer-Marschallinger, B., Bindlish, R., Wagner, W., Massari, C., 2020. Assimilation of Sentinel 1 and SMAP–based satellite soil moisture retrievals into SWAT hydrological model: the impact of satellite revisit time and product spatial resolution on flood simulations in small basins. Journal of hydrology 581, 124367.

Bachmair, S., Tanguy, M., Hannaford, J., Stahl, K., 2018. How well do meteorological indicators represent agricultural and forest drought across Europe? Environmental Research Letters 13, 034042.

Badger, A.M., Dirmeyer, P.A., 2015. Climate response to Amazon forest replacement by heterogeneous crop cover. Hydrology and Earth System Sciences 19, 4547–4557.

Baghdadi, N., El Hajj, M., Zribi, M., Bousbih, S., 2017. Calibration of the water cloud model at C-band for winter crop fields and grasslands. Remote Sensing 9, 969.

Bai, X., He, B., 2015. Potential of Dubois model for soil moisture retrieval in prairie areas using SAR and optical data. International Journal of Remote Sensing 36, 5737–5753.

Baldoncini, M., Albéri, M., Bottardi, C., Chiarelli, E., Raptis, K.G.C., Strati, V., Mantovani, F., 2019. Biomass water content effect on soil moisture assessment via proximal gamma-ray spectroscopy. Geoderma 335, 69–77.

Ball, J.T., Woodrow, I.E., Berry, J.A., 1987. A model predicting stomatal conductance and its contribution to the control of photosynthesis under different environmental conditions, in: Progress in Photosynthesis Research. Springer, pp. 221–224.

Bauer-Marschallinger, B., Freeman, V., Cao, S., Paulik, C., Schaufler, S., Stachl, T., Modanesi, S., Massari, C., Ciabatta, L., Brocca, L., 2018. Toward global soil moisture monitoring with Sentinel-1: Harnessing assets and overcoming obstacles. IEEE Transactions on Geoscience and Remote Sensing 57, 520–539.

Bazzi, H., Baghdadi, N., Ienco, D., El Hajj, M., Zribi, M., Belhouchette, H., Escorihuela, M.J., Demarez, V., 2019. Mapping irrigated areas using Sentinel-1 time series in Catalonia, Spain. Remote Sensing 11, 1836.

Bechtold, M., De Lannoy, G.J.M., Reichle, R.H., Roose, D., Balliston, N., Burdun, I., Devito, K., Kurbatova, J., Strack, M., Zarov, E.A., 2020. Improved groundwater table and L-band brightness temperature estimates for Northern Hemisphere peatlands using new model physics and SMOS observations in a global data assimilation framework. Remote Sensing of Environment 246, 111805.

Bhat, G.S., 2006. The Indian drought of 2002—a sub-seasonal phenomenon? Quarterly Journal of the Royal Meteorological Society: A journal of the atmospheric sciences, applied meteorology and physical oceanography 132, 2583–2602.

Bousbih, S., Zribi, M., El Hajj, M., Baghdadi, N., Lili-Chabaane, Z., Gao, Q., Fanise, P., 2018. Soil moisture and irrigation mapping in A semi-arid region, based on the synergetic use of Sentinel-1 and Sentinel-2 data. Remote Sensing 10, 1953.

Breña-Naranjo, J.A., Kendall, A.D., Hyndman, D.W., 2014. Improved methods for satellite-based groundwater storage estimates: A decade of monitoring the high plains aquifer from space and ground observations. Geophysical Research Letters 41, 6167–6173.

Bretreger, D., Yeo, I.-Y., Hancock, G., Willgoose, G., 2020. Monitoring irrigation using landsat observations and climate data over regional scales in the Murray-Darling Basin. Journal of Hydrology 590, 125356.

Brocca, L., Ciabatta, L., Massari, C., Moramarco, T., Hahn, S., Hasenauer, S., Kidd, R., Dorigo, W., Wagner, W., Levizzani, V., 2014. Soil as a natural rain gauge: Estimating global rainfall from satellite soil moisture data. Journal of Geophysical Research: Atmospheres 119, 5128–5141.

Brocca, L., Tarpanelli, A., Filippucci, P., Dorigo, W., Zaussinger, F., Gruber, A., Fernández-Prieto, D., 2018. How much water is used for irrigation? A new approach exploiting coarse resolution satellite soil moisture products. International journal of applied earth observation and geoinformation 73, 752–766.

Brocca, L., Tullo, T., Melone, F., Moramarco, T., Morbidelli, R., 2012. Catchment scale soil moisture spatial–temporal variability. Journal of hydrology 422, 63–75.

Brodzik, M.J., Billingsley, B., Haran, T., Raup, B., Savoie, M.H., 2012. EASE-Grid 2.0: Incremental but significant improvements for Earth-gridded data sets. ISPRS International Journal of Geo-Information 1, 32–45.

Buchhorn, M., Lesiv, M., Tsendbazar, N.-E., Herold, M., Bertels, L., Smets, B., 2020. Copernicus global land cover layers—collection 2. Remote Sensing 12, 1044.

Carrão, H., Russo, S., Sepulcre-Canto, G., Barbosa, P., 2016. An empirical standardized soil moisture index for agricultural drought assessment from remotely sensed data. International journal of applied earth observation and geoinformation 48, 74–84.

Carrera, M.L., Bilodeau, B., Bélair, S., Abrahamowicz, M., Russell, A., Wang, X., 2019. Assimilation of passive L-band microwave brightness temperatures in the Canadian Land Data Assimilation System: Impacts on short-range warm season numerical weather prediction. Journal of Hydrometeorology 20, 1053–1079.

Ceppi, A., Ravazzani, G., Corbari, C., Salerno, R., Meucci, S., Mancini, M., 2014. Real-time drought forecasting system for irrigation management. Hydrology and Earth System Sciences 18, 3353–3366. https://doi.org/10.5194/hess-18-3353-2014

Chan, S.K., Bindlish, R., O'Neill, P., Jackson, T., Njoku, E., Dunbar, S., Chaubell, J., Piepmeier, J., Yueh, S., Entekhabi, D., Colliander, A., Chen, F., Cosh, M.H., Caldwell, T., Walker, J., Berg, A., McNairn, H., Thibeault, M., Martínez-Fernández, J., Uldall, F., Seyfried, M., Bosch, D., Starks, P., Holifield Collins, C., Prueger, J., van der Velde, R., Asanuma, J., Palecki, M., Small, E.E., Zreda, M., Calvet, J., Crow, W.T., Kerr, Y., 2018. Development and assessment of the SMAP enhanced passive soil

moisture product. Remote Sensing of Environment 204, 931–941. https://doi.org/10.1016/j.rse.2017.08.025

Chen, F.; Crow, W.T.; Ryu, D., 2014. Dual forcing and state correction via soil moisture assimilation for improved rainfall-runoff modeling. J. Hydrometeorol. 15, 1832–1848.

Chen, F., Crow, W.T., Starks, P.J., Moriasi, D.N., 2011. Improving hydrologic predictions of a catchment model via assimilation of surface soil moisture. Advances in Water Resources 34, 526–536.

Chen, F., Dudhia, J., 2001. Coupling an advanced land surface–hydrology model with the Penn State–NCAR MM5 modeling system. Part I: Model implementation and sensitivity. Monthly weather review 129, 569–585.

Chen, F., Mitchell, K., Schaake, J., Xue, Y., Pan, H.-L., Koren, V., Duan, Q.Y., Ek, M., Betts, A., 1996. Modeling of land surface evaporation by four schemes and comparison with FIFE observations. Journal of Geophysical Research: Atmospheres 101, 7251–7268.

Chen, S., Gan, T.Y., Tan, X., Shao, D., and Zhu, J., 2019: Assessment of CFSR, ERA-Interim, JRA-55, MERRA-2, NCEP-2 reanalysis data for drought analysis over China, Clim. Dynam., 53, 737-757, https://doi.org/10.1007/s00382-018-04611-1.

Collow, T.W., Robock, A., Basara, J.B., Illston, B.G., 2012. Evaluation of SMOS retrievals of soil moisture over the central United States with currently available in situ observations J. Geophys. Res.-Atmos., 117, Article D09113

Cottrell, R.S., Nash, K.L., Halpern, B.S., Remenyi, T.A., Corney, S.P., Fleming, A., Fulton, E.A., Hornborg, S., Johne, A., Watson, R.A., 2019. Food production shocks across land and sea. Nat. Sustain. 2, 130–137.

Crow, W.T., Chen, F., Reichle, R.H., Liu, Q., 2017. L band microwave remote sensing and land data assimilation improve the representation of prestorm soil moisture conditions for hydrologic forecasting. Geophysical research letters 44, 5495–5503.

Crutzen, P., 2002. Geography of Mankind. Nature 415, 23.

D Udmale, P., Ichikawa, Y., S Kiem, A., N Panda, S., 2014. Drought impacts and adaptation strategies for agriculture and rural livelihood in the Maharashtra State of India. The Open Agriculture Journal 8.

Darby, H., Lauer, J., 2004. Plant physiology—critical stages in the life of a corn plant. Technical Rep.

Dari, J., Brocca, L., Quintana-Seguí, P., Escorihuela, M.J., Stefan, V., Morbidelli, R., 2020. Exploiting high-resolution remote sensing soil moisture to estimate irrigation water amounts over a Mediterranean region. Remote Sensing 12, 2593.

Das, N.N., Entekhabi, D., Njoku, E.G., 2010. An algorithm for merging SMAP radiometer and radar data for high-resolution soil-moisture retrieval. IEEE Transactions on Geoscience and Remote Sensing 49, 1504–1512.

De Lannoy, G.J., Reichle, R.H., 2016a. Assimilation of SMOS brightness temperatures or soil moisture retrievals into a land surface model. Hydrology and Earth System Sciences 20, 4895–4911.

De Lannoy, G.J., Reichle, R.H., 2016b. Global assimilation of multiangle and multipolarization SMOS brightness temperature observations into the GEOS-5 catchment land surface model for soil moisture estimation. Journal of Hydrometeorology 17, 669–691.

De Lannoy, G.J., Reichle, R.H., Pauwels, V.R., 2013. Global calibration of the GEOS-5 L-band microwave radiative transfer model over nonfrozen land using SMOS observations. Journal of Hydrometeorology 14, 765–785.

De Lannoy, G.J., Reichle, R.H., Vrugt, J.A., 2014. Uncertainty quantification of GEOS-5 L-band radiative transfer model parameters using Bayesian inference and SMOS observations. Remote Sensing of Environment 148, 146–157.

De Santis, D., Biondi, D., Crow, W.T., Camici, S., Modanesi, S., Brocca, L., Massari, C., 2021. Assimilation of Satellite Soil Moisture Products for River Flow Prediction: An Extensive Experiment in over 700

Catchments throughout Europe. Water Resources Research, 57, 6.https://doi.org/10.1029/2021WR029643

Di Gregorio, A., 2005. Land cover classification system: classification concepts and user manual: LCCS. Food & Agriculture Org.

Dierckx, W., Sterckx, S., Benhadj, I., Livens, S., Duhoux, G., Van Achteren, T., Francois, M., Mellab, K., Saint, G., 2014. PROBA-V mission for global vegetation monitoring: standard products and image quality. International Journal of Remote Sensing 35, 2589–2614.

Dorigo, W., Wagner, W., Albergel, C., Albrecht, F., Balsamo, G., Brocca, L., Chung, D., Ertl, M., Forkel, M., Gruber, A., 2017. ESA CCI Soil Moisture for improved Earth system understanding: State-of-the art and future directions. Remote Sensing of Environment 203, 185–215.

Dorigo, W.A., Gruber, A., De Jeu, R.A.M., Wagner, W., Stacke, T., Loew, A., Albergel, C., Brocca, L., Chung, D., Parinussa, R.M., 2015. Evaluation of the ESA CCI soil moisture product using ground-based observations. Remote Sensing of Environment 162, 380–395.

Dorigo, W. A., Scipal, K., Parinussa, R. M., Liu, Y. Y., Wagner, W., de Jeu, R. A. M., and Naeimi, V., 2010: Error characterization of global active and passive microwave soil moisture datasets, Hydrol. Earth Syst. Sci., 14, 2605–2616, doi:10.5194/hess-14- 2605-2010.

Drusch, M., 2007. Initializing numerical weather prediction models with satellite-derived surface soil moisture: Data assimilation experiments with ECMWF's Integrated Forecast System and the TMI soil moisture data set. Journal of Geophysical Research: Atmospheres 112.

Dutra, E., Viterbo, P., Miranda, P.M.A., 2008. Era-40 reanalysis hydrological applications in the characterization of regional drought Geophys. Res. Lett., 35, p. L19402

Dunne, S., and Entekhabi, D. 2005. An ensemble-based reanalysis approach to land data assimilation, Water Resour. Res., 41, W02013, doi:10.1029/2004WR003449

EC: Council Directive 2000/60/EC of 23. October 2000 establishing a framework for community action in the field of water policy Off. J. Eur. Communities, L 327, 1–72, 200

Ek, M.B., Mitchell, K.E., Lin, Y., Rogers, E., Grunmann, P., Koren, V., Gayno, G., Tarpley, J.D., 2003. Implementation of Noah land surface model advances in the National Centers for Environmental Prediction operational mesoscale Eta model. Journal of Geophysical Research: Atmospheres 108.

El Hajj, M., Baghdadi, N., Zribi, M., Belaud, G., Cheviron, B., Courault, D., Charron, F., 2016. Soil moisture retrieval over irrigated grassland using X-band SAR data. Remote Sensing of Environment 176, 202–218.

Entekhabi, D., Njoku, E.G., O'Neill, P.E., Kellogg, K.H., Crow, W.T., Edelstein, W.N., Entin, J.K., Goodman, S.D., Jackson, T.J., Johnson, J., Kimball, J., Piepmeier, J.R., Koster, R.D., Martin, N., McDonald, K.C., Moghaddam, M., Moran, S., Reichle, R., Shi, J.C., Spencer, M.W., Thurman, S.W., Tsang, L., Van Zyl, J., 2010. The Soil Moisture Active Passive (SMAP) Mission. Proceedings of the IEEE 98, 704–716. https://doi.org/10.1109/JPROC.2010.2043918

Escorihuela, M.J., Quintana-Seguí, P., 2016. Comparison of remote sensing and simulated soil moisture datasets in Mediterranean landscapes. Remote sensing of environment 180, 99–114.

Evans, J.P., Zaitchik, B.F., 2008. Modeling the large-scale water balance impact of different irrigation systems. Water Resources Research 44.

Evensen, G., 2003. The ensemble Kalman filter: Theoretical formulation and practical implementation. Ocean dynamics 53, 343–367.

Evensen, G., 1994. Sequential data assimilation with a nonlinear quasi-geostrophic model using Monte Carlo methods to forecast error statistics. Journal of Geophysical Research: Oceans 99, 10143–10162.

Falkenmark, M., 2003. Freshwater as shared between society and ecosystems: from divided approaches to integrated challenges. Philosophical Transactions of the Royal Society of London. Series B: Biological Sciences 358, 2037–2049.

Falkenmark, M., Rockström, J., 2006. The new blue and green water paradigm: Breaking new ground for water resources planning and management.

Falkenmark, M., Wang-Erlandsson, L., Rockström, J., 2019. Understanding of water resilience in the Anthropocene. Journal of Hydrology X 2, 100009.

Fang, L., Hain, C.R., Zhan, X., Anderson, M.C., 2016. An inter-comparison of soil moisture data products from satellite remote sensing and a land surface model. International journal of applied earth observation and geoinformation 48, 37–50.

Fang, L., Zhan, X., Hain, C.R., Liu, J., 2018. Impact of using near real-time green vegetation fraction in Noah land surface model of NOAA NCEP on numerical weather predictions. Advances in Meteorology 2018.

Farahmand, A., AghaKouchak, A., 2015. A generalized framework for deriving nonparametric standardized drought indicators. Advances in Water Resources 76, 140–145.

Ferrazzoli, P., Paloscia, S., Pampaloni, P., Schiavon, G., Solimini, D., Coppo, P., 1992. Sensitivity of microwave measurements to vegetation biomass and soil moisture content: A case study. IEEE Transactions on Geoscience and Remote Sensing 30, 750–756.

Filippucci, P., Tarpanelli, A., Massari, C., Serafini, A., Strati, V., Alberi, M., Raptis, K.G.C., Mantovani, F., Brocca, L., 2020. Soil moisture as a potential variable for tracking and quantifying irrigation: A case study with proximal gamma-ray spectroscopy data. Advances in Water Resources 136, 103502.

Foley, J.A., Ramankutty, N., Brauman, K.A., Cassidy, E.S., Gerber, J.S., Johnston, M., Mueller, N.D., O'Connell, C., Ray, D.K., West, P.C., Balzer, C., Bennett, E.M., Carpenter, S.R., Hill, J., Monfreda, C., Polasky, S., Rockström, J., Sheehan, J., Siebert, S., Tilman, D., Zaks, D.P.M., 2011. Solutions for a cultivated planet. Nature 478, 337–342. https://doi.org/10.1038/nature10452

Foster, T., Mieno, T., Brozović, N., 2020. Satellite-Based Monitoring of Irrigation Water Use: Assessing Measurement Errors and Their Implications for Agricultural Water Management Policy. Water Resources Research 56, e2020WR028378.

Francois, M., Santandrea, S., Mellab, K., Vrancken, D., Versluys, J., 2014. The PROBA-V mission: The space segment. International Journal of Remote Sensing 35, 2548–2564.

Fung, A.K., 1994. Microwave scattering and emission models and their applications. Norwood, MA: Artech House, 1994.

Gao, Q., Zribi, M., Escorihuela, M.J., Baghdadi, N., Segui, P.Q., 2018. Irrigation mapping using Sentinel-1 time series at field scale. Remote Sensing 10, 1495.

Gelaro, R., McCarty, W., Suárez, M.J., Todling, R., Molod, A., Takacs, L., Randles, C.A., Darmenov, A., Bosilovich, M.G., Reichle, R., 2017. The modern-era retrospective analysis for research and applications, version 2 (MERRA-2). Journal of climate 30, 5419–5454.

Gibon, F., Pellarin, T., Román-Cascón, C., Alhassane, A., Traoré, S., Kerr, Y., Seen, D.L., Baron, C., 2018. Millet yield estimates in the Sahel using satellite derived soil moisture time series. Agricultural and Forest Meteorology 262, 100–109.

Girotto, M., De Lannoy, G.J., Reichle, R.H., Rodell, M., Draper, C., Bhanja, S.N., Mukherjee, A., 2017. Benefits and pitfalls of GRACE data assimilation: A case study of terrestrial water storage depletion in India. Geophysical research letters 44, 4107–4115.

Gruber, A., Wagner, W., Hegyiova, A., Greifeneder, F., Schlaffer, S., 2013. Potential of Sentinel-1 for high-resolution soil moisture monitoring, in: 2013 IEEE International Geoscience and Remote Sensing Symposium-IGARSS. IEEE, pp. 4030–4033.

Gunst, L., Rego, F., Dias, S.M.A., Bifulco, C., Stagge, J.H., Rocha, M.S., Van Lanen, H.A.J., 2014. Links between meteorological drought indices and yields (1979-2009) of the main European crops. No. Technical Report.

Gupta, H.V., Kling, H., Yilmaz, K.K., Martinez, G.F., 2009. Decomposition of the mean squared error and NSE performance criteria: Implications for improving hydrological modelling. Journal of hydrology 377, 80–91.

Gutman, G., Ignatov, A., 1998. The derivation of the green vegetation fraction from NOAA/AVHRR data for use in numerical weather prediction models. International Journal of remote sensing 19, 1533–1543.

Guttman, N.B., 1999. Accepting the standardized precipitation index: a calculation algorithm 1. JAWRA Journal of the American Water Resources Association 35, 311–322.

Haddeland, I., Heinke, J., Biemans, H., Eisner, S., Flörke, M., Hanasaki, N., Konzmann, M., Ludwig, F., Masaki, Y., Schewe, J., 2014. Global water resources affected by human interventions and climate change. Proceedings of the National Academy of Sciences 111, 3251–3256.

Hao, Z., AghaKouchak, A., 2013. Multivariate standardized drought index: a parametric multi-index model. Advances in Water Resources 57, 12–18.

Hayes, M., Svoboda, M., Wall, N., Widhalm, M., 2011. The Lincoln declaration on drought indices: universal meteorological drought index recommended. Bulletin of the American Meteorological Society 92, 485–488.

Hinkle, D.E., Wiersma, W., Jurs, S.G., 2003. Applied statistics for the behavioral sciences (Vol. 663).

Hoekstra, A.Y., 2011. The global dimension of water governance: Why the river basin approach is no longer sufficient and why cooperative action at global level is needed. Water 3, 21–46.

Houser, P. R., Shuttleworth, W. J., Famiglietti, J. S., Gupta, H. V., Syed, K. H., Goodrich, D. C., 1998. Integration of soil moisture remote sensing and hydrological modeling using data assimilation, Water Resour. Res., 34(12), 3405–3420.

Houser, P.R., De Lannoy, G., Walker, J.P., 2012. Hydrologic Data Assimilation J.P. ITiefenbacher (Ed.), In: Approaches to Managing Disaster – Assessing Hazards, Emergencies, Disaster Impacts, InTech, p. 162 ISBN: 978-953-51-0294-6

Hu, X., Shi, L., Zeng, J., Yang, J., Zha, Y., Yao, Y., Cao, G., 2016. Estimation of actual irrigation amount and its impact on groundwater depletion: A case study in the Hebei Plain, China. Journal of Hydrology 543, 433–449.

IPCC. 2021: Summary for Policymakers. In Climate Change 2021: The Physical Science Basis. Contribution of Working Group I to the Sixth Assessment Report of the Intergovernmental Panel on Climate Change; Masson-Delmotte, V., Zhai, P., Pirani, A., Connors, S.L., Péan, C., Berger, S., Caud, N., Chen, Y., Goldfarb, L., Gomis, M.I., et al., Eds.; Cambridge University Press: Cambridge, UK, 2021; in press; Available online: https://www.ipcc.ch/report/ar6/wg1/downloads/report/IPCC_AR6_WGI_SPM.pdf (accessed on 5 September 2021Jalilvand, E., Tajrishy, M., Hashemi, S.A.G.Z., Brocca, L., 2019. Quantification of irrigation water using remote sensing of soil moisture in a semi-arid region. Remote Sensing of Environment 231, 111226.

Jayasree, V., Venkatesh, B., 2015. Analysis of rainfall in assessing the drought in semi-arid region of Karnataka State, India. Water Resources Management 29, 5613–5630.

Kennedy, J., Eberhart, R., 1995. Particle swarm optimization, in: Proceedings of ICNN'95-International Conference on Neural Networks. IEEE, pp. 1942–1948.

Kerr, Y.H., 2007. Soil moisture from space: where are we) Hydrogeol. J., 15, pp. 117-120

Kolassa, J., Reichle, R.H., Draper, C.S., 2017. Merging active and passive microwave observations in soil moisture data assimilation. Remote Sensing of Environment 191, 117–130.

Krishna Kumar, K., Rupa Kumar, K., Ashrit, R.G., Deshpande, N.R., Hansen, J.W., 2004. Climate impacts on Indian agriculture. International Journal of Climatology 24, 1375–1393. https://doi.org/10.1002/joc.1081

Kumar, K., Suryanarayana Rao, H.P., Arora, M.K., 2015. Study of water cloud model vegetation descriptors in estimating soil moisture in Solani catchment. Hydrological processes 29, 2137–2148.

Kumar, S.V., Holmes, T.R., Bindlish, R., Jeu, R. de, Peters-Lidard, C., 2020. Assimilation of vegetation optical depth retrievals from passive microwave radiometry. Hydrology and Earth System Sciences 24, 3431–3450.

Kumar, S. V., Mocko, D. M., Wang, S., Peters-Lidard, C. D., Borak, J., 2019. Assimilation of remotely sensed Leaf Area Index into the Noah-MP land surface model: Impacts on water and carbon fluxes and states over the Continental U.S., Journal of Hydrometeorology, doi:10.1175/JHM-D-18-0237.1.

Kumar, S.V., Peters-Lidard, C.D., Mocko, D., Reichle, R., Liu, Y., Arsenault, K.R., Xia, Y., Ek, M., Riggs, G., Livneh, B., 2014. Assimilation of remotely sensed soil moisture and snow depth retrievals for drought estimation. Journal of Hydrometeorology 15, 2446–2469.

Kumar, S.V., Peters-Lidard, C.D., Santanello, J.A., Reichle, R.H., Draper, C.S., Koster, R.D., Nearing, G., Jasinski, M.F., 2015. Evaluating the utility of satellite soil moisture retrievals over irrigated areas and the ability of land data assimilation methods to correct for unmodeled processes. Hydrology and Earth System Sciences 19, 4463–4478.

Kumar, S.V., Reichle, R.H., Peters-Lidard, C.D., Koster, R.D., Zhan, X., Crow, W.T., Eylander, J.B., Houser, P.R., 2008. A land surface data assimilation framework using the land information system: Description and applications. Advances in Water Resources 31, 1419–1432.

Lagouarde, J.-P., Bhattacharya, B., Crébassol, P., Gamet, P., Adlakha, D., Murthy, C., Singh, S., Mishra, M., Nigam, R., Raju, P., Babu, S., Shukla, M., Pandya, M., Boulet, G., Briottet, X., Dadou, I., Dedieu, G., Gouhier, M., Hagolle, O., Irvine, M., Jacob, F., Kumar, K., Laignel, B., Maisongrande, P., Mallick, K., Olioso, A., Ottle, C., Roujean, J.-L., Sobrino, J., Ramakrishnan, R., Sekhar, M., Sarkar, S., 2019. Indo-French High-resolution Thermal Infrared Space Mission for Earth Natural Resources Assessment and Monitoring -Concept and Definition of TRISHNA. Presented at the ISPRS-GEOGLAM-ISRS Joint International Workshop on "Earth Observations for Agricultural Monitoring," p. 403. https://doi.org/10.5194/isprs-archives-XLII-3-W6-403-2019

Laloy, E., Vrugt, J.A., 2012. High-dimensional posterior exploration of hydrologic models using multiple-try DREAM (ZS) and high-performance computing. Water Resources Research 48.

Lawston, P.M., Santanello Jr, J.A., Kumar, S.V., 2017. Irrigation signals detected from SMAP soil moisture retrievals. Geophysical Research Letters 44, 11–860.

Lawston, P.M., Santanello Jr, J.A., Zaitchik, B.F., Rodell, M., 2015. Impact of irrigation methods on land surface model spinup and initialization of WRF forecasts. Journal of Hydrometeorology 16, 1135–1154.

Le, M.H., Kim, H.; Moon, H.; Zhang, R., Lakshmi, V., Nguyen, L.B., 2020. Assessment of drought conditions over Vietnam using standardized precipitation evapotranspiration index, MERRA-2 re-analysis, and dynamic land cover.J. Hydrol. Reg. Stud., 32, 100767.

Le Page, M., Jarlan, L., El Hajj, M.M., Zribi, M., Baghdadi, N., Boone, A., 2020. Potential for the detection of irrigation events on maize plots using sentinel-1 soil moisture products. Remote Sensing 12, 1621.

Lei, F., Crow, W.T., Kustas, W.P., Dong, J., Yang, Y., Knipper, K.R., Anderson, M.C., Gao, F., Notarnicola, C., Greifeneder, F., 2020. Data assimilation of high-resolution thermal and radar remote sensing retrievals for soil moisture monitoring in a drip-irrigated vineyard. Remote sensing of environment 239, 111622.

Li, J., Wang, S., 2018. Using SAR-derived vegetation descriptors in a water cloud model to improve soil moisture retrieval. Remote Sensing 10, 1370.

Lievens, H., Demuzere, M., Marshall, H.-P., Reichle, R.H., Brucker, L., Brangers, I., de Rosnay, P., Dumont, M., Girotto, M., Immerzeel, W.W., Jonas, T., Kim, E.J., Koch, I., Marty, C., Saloranta, T., Schöber, J.,

De Lannoy, G.J.M., 2019. Snow depth variability in the Northern Hemisphere mountains observed from space. Nature Communications 10, 4629. https://doi.org/10.1038/s41467-019-12566-y

Lievens, H., Martens, B., Verhoest, N.E.C., Hahn, S., Reichle, R.H., Miralles, D.G., 2017a. Assimilation of global radar backscatter and radiometer brightness temperature observations to improve soil moisture and land evaporation estimates. Remote Sensing of Environment 189, 194–210.

Lievens, H., Reichle, R.H., Liu, Q., De Lannoy, G.J., Dunbar, R.S., Kim, S.B., Das, N.N., Cosh, M., Walker, J.P., Wagner, W., 2017b. Joint Sentinel-1 and SMAP data assimilation to improve soil moisture estimates. Geophysical research letters 44, 6145–6153.

Lievens, H., Tomer, S.K., Al Bitar, A., De Lannoy, G.J., Drusch, M., Dumedah, G., Franssen, H.-J.H., Kerr, Y.H., Martens, B., Pan, M., 2015. SMOS soil moisture assimilation for improved hydrologic simulation in the Murray Darling Basin, Australia. Remote Sensing of Environment 168, 146–162.

Lim, C.-H., Kim, S.H., Chun, J.A., Kafatos, M.C., Lee, W.-K., 2019. Assessment of agricultural drought considering the hydrological cycle and crop phenology in the Korean Peninsula. Water 11, 1105.

Liu, C., Shi, J., 2016. Estimation of vegetation parameters of water cloud model for global soil moisture retrieval using time-series L-band Aquarius observations. IEEE Journal of Selected Topics in Applied Earth Observations and Remote Sensing 9, 5621–5633.

Liu, Y.Y., Dorigo, W.A., Parinussa, R.M., de Jeu, R.A., Wagner, W., McCabe, M.F., Evans, J.P., Van Dijk, A., 2012. Trend-preserving blending of passive and active microwave soil moisture retrievals. Remote Sensing of Environment 123, 280–297.

Liu, Y.Y., Parinussa, R.M., Dorigo, W.A., De Jeu, R.A., Wagner, W., Van Dijk, A., McCabe, M.F., Evans, J.P., 2011. Developing an improved soil moisture dataset by blending passive and active microwave satellite-based retrievals. Hydrology and Earth System Sciences 15, 425–436.

Macelloni, G., Paloscia, S., Pampaloni, P., Marliani, F., Gai, M., 2001. The relationship between the backscattering coefficient and the biomass of narrow and broad leaf crops. IEEE Transactions on Geoscience and Remote Sensing 39, 873–884.

Mahrt, L., Pan, H., 1984. A two-layer model of soil hydrology. Boundary-Layer Meteorology 29, 1–20.

Martínez-Fernández, J., González-Zamora, A., Sánchez, N., Gumuzzio, A., 2015. A soil water based index as a suitable agricultural drought indicator. Journal of Hydrology 522, 265–273.

Martínez-Fernández, J., González-Zamora, A., Sánchez, N., Gumuzzio, A., Herrero-Jiménez, C.M., 2016 Satellite soil moisture for agricultural drought monitoring: assessment of the SMOS derived Soil Water Deficit Index Remote Sens. Environ., 177, pp. 277-286, 10.1016/j.rse.2016.02.064

Massari, C., Modanesi, S., Dari, J., Gruber, A., De Lannoy, G.J., Girotto, M., Quintana-Seguí, P., Le Page, M., Jarlan, L., Zribi, M., 2021. A review of irrigation information retrievals from space and their utility for users. Remote Sensing 13, 4112.

Massey Jr, F.J., 1951. The Kolmogorov-Smirnov test for goodness of fit. Journal of the American statistical Association 46, 68–78.

Matthews, O.P., Germain, D.S., 2007. Boundaries and transboundary water conflicts. Journal of Water Resources Planning and Management 133, 386–396.

McCabe, M.F., Aragon, B., Houborg, R., Mascaro, J., 2017. CubeSats in Hydrology: Ultrahigh-Resolution Insights Into Vegetation Dynamics and Terrestrial Evaporation. Water Resources Research 53, 10017–10024. https://doi.org/10.1002/2017WR022240

McKee, T.B., Doesken, N.J., Kleist, J., 1993. The relationship of drought frequency and duration to time scales, in: Proceedings of the 8th Conference on Applied Climatology. Boston, pp. 179–183.

Miller, J., Barlage, M., Zeng, X., Wei, H., Mitchell, K., Tarpley, D., 2006. Sensitivity of the NCEP/Noah land surface model to the MODIS green vegetation fraction data set. Geophysical research letters 33.

Mishra, A., Vu, T., Veettil, A.V., Entekhabi, D., 2017. Drought monitoring with soil moisture active passive (SMAP) measurements. Journal of Hydrology 552, 620–632.

Mishra, A.K., Singh, V.P., 2010. A review of drought concepts. Journal of hydrology 391, 202–216.

Mishra, V., Aadhar, S., Asoka, A., Pai, S., Kumar, R., 2016. On the frequency of the 2015 monsoon season drought in the Indo-Gangetic Plain. Geophysical Research Letters 43, 12–102.

Mishra, V., Shah, R., Azhar, S., Shah, H., Modi, P., Kumar, R., 2018. Reconstruction of droughts in India using multiple land-surface models (1951–2015). Hydrology and Earth System Sciences 22, 2269–2284.

Modanesi, S., Massari, C., Camici, S., Brocca, L., Amarnath, G., 2020. Do Satellite Surface Soil Moisture Observations Better Retain Information About Crop-Yield Variability in Drought Conditions? Water Resources Research 56, e2019WR025855.

Modanesi, S., Massari, C., Gruber, A., Lievens, H., Tarpanelli, A., Morbidelli, R., De Lannoy, G.J.M., 2021. Optimizing a backscatter forward operator using Sentinel-1 data over irrigated land. Hydrology and Earth System Sciences 25, 6283–6307. https://doi.org/10.5194/hess-25-6283-2021

Monfreda, C., Ramankutty, N., Foley, J.A., 2008. Farming the planet: 2. Geographic distribution of crop areas, yields, physiological types, and net primary production in the year 2000. Global biogeochemical cycles 22.

Montanari, A., Young, G., Savenije, H.H.G., Hughes, D., Wagener, T., Ren, L.L., Koutsoyiannis, D., Cudennec, C., Toth, E., Grimaldi, S., 2013. "Panta Rhei—everything flows": change in hydrology and society—the IAHS scientific decade 2013–2022. Hydrological Sciences Journal 58, 1256–1275.

Musolino, D., de Carli, A., Massarutto, A., 2017. Evaluation of socio-economic impact of drought events: The case of Po river basin. European Countryside 9, 163.

Narasimhan, B., Srinivasan, R., 2005. Development and evaluation of Soil Moisture Deficit Index (SMDI) and Evapotranspiration Deficit Index (ETDI) for agricultural drought monitoring. Agricultural and forest meteorology 133, 69–88.

Nie, W., Zaitchik, B.F., Rodell, M., Kumar, S.V., Anderson, M.C., Hain, C., 2018. Groundwater withdrawals under drought: Reconciling GRACE and land surface models in the United States High Plains Aquifer. Water Resources Research 54, 5282–5299.

Niu, G.-Y., Yang, Z.-L., Dickinson, R.E., Gulden, L.E., 2005. A simple TOPMODEL-based runoff parameterization (SIMTOP) for use in global climate models. Journal of Geophysical Research: Atmospheres 110.

Niu, G.-Y., Yang, Z.-L., Dickinson, R.E., Gulden, L.E., Su, H., 2007. Development of a simple groundwater model for use in climate models and evaluation with Gravity Recovery and Climate Experiment data. Journal of Geophysical Research: Atmospheres 112.

Niu, G.-Y., Yang, Z.-L., Mitchell, K.E., Chen, F., Ek, M.B., Barlage, M., Kumar, A., Manning, K., Niyogi, D., Rosero, E., 2011. The community Noah land surface model with multiparameterization options (Noah-MP): 1. Model description and evaluation with local-scale measurements. Journal of Geophysical Research: Atmospheres 116.

Norman, J.M., Kustas, W.P., Humes, K.S., 1995. Source approach for estimating soil and vegetation energy fluxes in observations of directional radiometric surface temperature. Agricultural and Forest Meteorology 77, 263–293.

Oh, Y., 2004. Quantitative retrieval of soil moisture content and surface roughness from multipolarized radar observations of bare soil surfaces. IEEE Transactions on Geoscience and Remote Sensing 42, 596–601.

Oh, Y., Sarabandi, K., Ulaby, F.T., 1992. An empirical model and an inversion technique for radar scattering from bare soil surfaces. IEEE transactions on Geoscience and Remote Sensing 30, 370–381.

Ozdogan, M., Gutman, G., 2008. A new methodology to map irrigated areas using multi-temporal MODIS and ancillary data: An application example in the continental US. Remote Sensing of Environment 112, 3520–3537.

Ozdogan, M., Rodell, M., Beaudoing, H.K., Toll, D.L., 2010a. Simulating the effects of irrigation over the United States in a land surface model based on satellite-derived agricultural data. Journal of Hydrometeorology 11, 171–184.

Ozdogan, M., Yang, Y., Allez, G., Cervantes, C., 2010b. Remote sensing of irrigated agriculture: Opportunities and challenges. Remote sensing 2, 2274–2304.

Paloscia, S., Pettinato, S., Santi, E., Notarnicola, C., Pasolli, L., Reppucci, A., 2013. Soil moisture mapping using Sentinel-1 images: Algorithm and preliminary validation. Remote Sensing of Environment 134, 234–248.

Peel, M.C., Finlayson, B.L., McMahon, T.A., 2007. Updated world map of the Köppen-Geiger climate classification. Hydrology and earth system sciences 11, 1633–1644.

Peled, E., Dutra, E., Viterbo, P., Angert, A., 2010. Comparing and ranking soil drought indices performance over Europe, through remote-sensing of vegetation. Hydrology and Earth System Sciences 14, 271–277.

Piles, M., Camps, A., Vall-Llossera, M., Corbella, I., Panciera, R., Rudiger, C., Kerr, Y.H., Walker, J., 2011. Downscaling SMOS-derived soil moisture using MODIS visible/infrared data. IEEE transactions on Geoscience and Remote Sensing 49, 3156–3166.

Postel, S.L., Daily, G.C., Ehrlich, P.R., 1996. Human appropriation of renewable fresh water. Science 271, 785–788.

Po River Watershed Authority: Caratteristiche del bacino del fiume Po e primo esame dell'impatto ambientale delle attività umane sulle risorse idriche, available at http://www.adbpo.it/PBI/Piano_adottato/Relazione_Generale_07_12_2016.pdf, 2016.

Qian, Y., Yang, Z., Feng, Z., Liu, Y., Gustafson, W.I., Berg, L.K., Huang, M., Yang, B., Ma, H.-Y., 2020. Neglecting irrigation contributes to the simulated summertime warm-and-dry bias in the central United States. npj Climate and Atmospheric Science 3, 1–10.

Rahmani, A., Golian, S., Brocca, L., 2016. Multiyear monitoring of soil moisture over Iran through satellite and reanalysis soil moisture products. International journal of applied earth observation and geoinformation 48, 85–95.

Reichle, R.H., De Lannoy, G.J., Liu, Q., Ardizzone, J.V., Colliander, A., Conaty, A., Crow, W., Jackson, T.J., Jones, L.A., Kimball, J.S., 2017a. Assessment of the SMAP level-4 surface and root-zone soil moisture product using in situ measurements. Journal of Hydrometeorology 18, 2621–2645.

Reichle, R.H., Draper, C.S., Liu, Q., Girotto, M., Mahanama, S.P., Koster, R.D., De Lannoy, G.J., 2017b. Assessment of MERRA-2 land surface hydrology estimates. Journal of Climate 30, 2937–2960.

Reichle, R.H., Liu, Q., Koster, R.D., Crow, W.T., De Lannoy, G.J., Kimball, J.S., Ardizzone, J.V., Bosch, D., Colliander, A., Cosh, M., 2019. Version 4 of the SMAP Level-4 Soil Moisture algorithm and data product. Journal of Advances in Modeling Earth Systems 11, 3106–3130.

Reichle, R.H., McLaughlin, D.B., Entekhabi, D., 2002. Hydrologic data assimilation with the ensemble Kalman filter. Monthly Weather Review 130, 103–114.

Rigon, R., Formetta, G., Bancheri, M., Tubini, N., D'Amato, C., David, O., Massari, C., 2022. HESS Opinions: Participatory Digital Earth Twin Hydrology systems (DARTHs) for everyone: a blueprint for hydrologists. Hydrology and Earth System Sciences Discussions 1–38. https://doi.org/10.5194/hess-2021-644

Romaguera, M., Krol, M.S., Salama, M., Su, Z., Hoekstra, A.Y., 2014. Application of a remote sensing method for estimating monthly blue water evapotranspiration in irrigated agriculture. Remote sensing 6, 10033–10050.

Salmon, J.M., Friedl, M.A., Frolking, S., Wisser, D., Douglas, E.M., 2015. Global rain-fed, irrigated, and paddy croplands: A new high resolution map derived from remote sensing, crop inventories and climate data. International Journal of Applied Earth Observation and Geoinformation 38, 321–334.

Savenije, H.H.G., Hoekstra, A.Y., Van der Zaag, P., 2013. Evolving water science in the Anthropocene. Hydrol. Earth Syst. Sci. Discuss 10, 7619–7649.

Schneider, U., Becker, A., Finger, P., Meyer-Christoffer, A., Ziese, M., Rudolf, B., 2014. GPCC's new land surface precipitation climatology based on quality-controlled in situ data and its role in quantifying the global water cycle. Theoretical and Applied Climatology 115, 15–40.

Shapiro, S.S., Wilk, M.B., 1965. An analysis of variance test for normality (complete samples). Biometrika 52, 591–611.

Sheffield, J., Goteti, G., Wen, F., Wood, E.F., 2004. A simulated soil moisture based drought analysis for the United States. Journal of Geophysical Research: Atmospheres 109.

Siebert, S., Kummu, M., Porkka, M., Döll, P., Ramankutty, N., Scanlon, B.R., 2015. A global data set of the extent of irrigated land from 1900 to 2005. Hydrology and Earth System Sciences 19, 1521–1545.

Sigdel, M., Ikeda, M., 2010. Spatial and temporal analysis of drought in Nepal using standardized precipitation index and its relationship with climate indices. Journal of Hydrology and Meteorology 7, 59–74.

Sol'áková, T., De Michele, C., Vezzoli, R., 2014. Comparison between parametric and nonparametric approaches for the calculation of two drought indices: SPI and SSI. Journal of Hydrologic Engineering 19, 04014010.

Stagge, J.H., Tallaksen, L.M., Gudmundsson, L., Van Loon, A.F., Stahl, K., 2015. Candidate distributions for climatological drought indices (SPI and SPEI). International Journal of Climatology 35, 4027–4040.

Steffen, W., Grinevald, J., Crutzen, P., McNeill, J., 2011. The Anthropocene: conceptual and historical perspectives. Philosophical Transactions of the Royal Society A: Mathematical, Physical and Engineering Sciences 369, 842–867.

Steffen, W., Richardson, K., Rockström, J., Cornell, S.E., Fetzer, I., Bennett, E.M., Biggs, R., Carpenter, S.R., De Vries, W., De Wit, C.A., 2015. Planetary boundaries: Guiding human development on a changing planet. Science 347.

Stephens, M.A., 1974. EDF statistics for goodness of fit and some comparisons. Journal of the American statistical Association 69, 730–737.

Strati, V., Albéri, M., Anconelli, S., Baldoncini, M., Bittelli, M., Bottardi, C., Chiarelli, E., Fabbri, B., Guidi, V., Raptis, K.G.C., 2018. Modelling soil water content in a tomato field: proximal gamma ray spectroscopy and soil–crop system models. Agriculture 8, 60.

Strosser, P., Dworak, T., Garzon Delvaux, P.A., Berglund, M., Schmidt, G., Mysiak, J., Kossida, M., Iacovides, I., Ashton, V., 2012. Final Report Gap Analysis of the Water Scarcity and Droughts Policy in the EU European Commission. European Commission.

Su, C.-H., Zhang, J., Gruber, A., Parinussa, R., Ryu, D., Crow, W.T., Wagner, W., 2016 Remote sensing of environment error decomposition of nine passive and active microwave satellite soil moisture data sets over Australia.Remote Sens., 182, pp. 128-140, 10.1016/j.rse.2016.05.008

Van Loon, A.F., 2015. Hydrological drought explained. Wiley Interdisciplinary Reviews: Water 2, 359–392.

Veloso, A., Mermoz, S., Bouvet, A., Le Toan, T., Planells, M., Dejoux, J.-F., Ceschia, E., 2017. Understanding the temporal behavior of crops using Sentinel-1 and Sentinel-2-like data for agricultural applications. Remote sensing of environment 199, 415–426.

Velpuri, N.M., Senay, G.B., Morisette, J.T., 2016. Evaluating new SMAP soil moisture for drought monitoring in the rangelands of the US high plains. Rangelands 38, 183–190.

Verger, A., Baret, F., Weiss, M., 2014. Near real-time vegetation monitoring at global scale. IEEE Journal of Selected Topics in Applied Earth Observations and Remote Sensing 7, 3473–3481.

Vicente-Serrano, S.M., Quiring, S.M., Pena-Gallardo, M., Yuan, S., Dominguez-Castro, F., 2020. A review of environmental droughts: Increased risk under global warming? Earth-Science Reviews 201, 102953.

Vreugdenhil, M., Navacchi, C., Bauer-Marschallinger, B., Hahn, S., Steele-Dunne, S., Pfeil, I., Dorigo, W., Wagner, W., 2020. Sentinel-1 cross ratio and vegetation optical depth: A comparison over Europe. Remote Sensing 12, 3404.

Vreugdenhil, M., Wagner, W., Bauer-Marschallinger, B., Pfeil, I., Teubner, I., Rüdiger, C., Strauss, P., 2018. Sensitivity of Sentinel-1 backscatter to vegetation dynamics: An Austrian case study. Remote Sensing 10, 1396.

Vrugt, J. A., Diks, C. G. H., Gupta, H. V., Bouten, W., Verstraten J. M., 2005. Improved treatment of uncertainty in hydrologic modeling: Combining the strengths of global optimization and data assimilation, Water Resour. Res., 41, W01017, doi:10.1029/2004WR003059.

Vrugt, J.A., Ter Braak, C.J., Clark, M.P., Hyman, J.M., Robinson, B.A., 2008. Treatment of input uncertainty in hydrologic modeling: Doing hydrology backward with Markov chain Monte Carlo simulation. Water Resources Research 44.

Wada, Y., Bierkens, M.F., Roo, A. de, Dirmeyer, P.A., Famiglietti, J.S., Hanasaki, N., Konar, M., Liu, J., Müller Schmied, H., Oki, T., 2017. Human–water interface in hydrological modelling: current status and future directions. Hydrology and Earth System Sciences 21, 4169–4193.

Wagner, W., Dorigo, W., de Jeu, R., Fernandez, D., Benveniste, J., Haas, E., Ertl, M., 2012. Fusion of active and passive microwave observations to create an essential climate variable data record on soil moisture. ISPRS Annals of the Photogrammetry, Remote Sensing and Spatial Information Sciences (ISPRS Annals) 7, 315–321.

Wagner, W., Hahn, S., Kidd, R., Melzer, T., Bartalis, Z., Hasenauer, S., Figa-Saldaña, J., De Rosnay, P., Jann, A., Schneider, S., 2013. The ASCAT soil moisture product: A review of its specifications, validation results, and emerging applications, Meteorol. Z., 22, 5–33.

Wagner, W., Lemoine, G., Borgeaud, M., Rott, H., 1999. A study of vegetation cover effects on ERS scatterometer data. IEEE Transactions on Geoscience and Remote Sensing 37, 938–948.

Tramblay, Y., Koutroulis, A., Samaniego, L., Vicente-Serrano, S.M., Volaire, F., Boone, A., Le Page, M., Llasat, M.C., Albergel, C., Burak, S., 2020. Challenges for drought assessment in the Mediterranean region under future climate scenarios. Earth-Science Reviews 103348.

Zappa, L., Schlaffer, S., Bauer-Marschallinger, B., Nendel, C., Zimmerman, B., Dorigo, W., 2021. Detection and Quantification of Irrigation Water Amounts at 500 m Using Sentinel-1 Surface Soil Moisture. Remote Sensing 13, 1727.

Zargar, A., Sadiq, R., Naser, B., Khan, F.I., 2011. A review of drought indices. Environmental Reviews 19, 333–349.

Zaussinger, F., Dorigo, W., Gruber, A., Tarpanelli, A., Filippucci, P., Brocca, L., 2019. Estimating irrigation water use over the contiguous United States by combining satellite and reanalysis soil moisture data. Hydrology and earth system sciences 23, 897–923.

Zhang, X., Obringer, R., Wei, C., Chen, N., Niyogi, D., 2017. Droughts in India from 1981 to 2013 and implications to wheat production. Scientific reports 7, 1–12.

Zhu, Q., Luo, Y., Xu, Y.-P., Tian, Y., Yang, T., 2019. Satellite soil moisture for agricultural drought monitoring: Assessment of SMAP-derived soil water deficit index in Xiang River Basin, China. Remote Sensing 11, 362.

Zribi, M., Baghdadi, N., Holah, N., Fafin, O., 2005. New methodology for soil surface moisture estimation and its application to ENVISAT-ASAR multi-incidence data inversion. Remote sensing of environment 96, 485–496.

Zribi, M., Chahbi, A., Shabou, M., Lili-Chabaane, Z., Duchemin, B., Baghdadi, N., Amri, R., Chehbouni, A., 2011. Soil surface moisture estimation over a semi-arid region using ENVISAT ASAR radar data for soil evaporation evaluation. Hydrology and Earth System Sciences 15, 345–358.

UNEP, 2016, Loss and Damage: the Role of Ecosystem Services World Bank, 2018, Ground Swell: Preparing

for Internal Climate Migration

Publications

Submitted

Modanesi, S., Massari, C., Bechtold, M., Lievens, H., Tarpanelli, A., Brocca, L., Zappa, L. and De Lannoy, G. J. M. **Challenges and benefits of quantifying irrigation through the assimilation of Sentinel-1 backscatter observations into Noah-MP**. Submitted to HESS, 2022.

Published in peer reviewed journal

Elwan, E., Le Page, M., Jarlan, L., Brocca, L., **Modanesi, S.**, Dari, J., Quintana Segui, P., Zribi, M. **Irrigation mapping on two contrasted climatic contexts using Sentinel-1 and Sentinel-2 data.** Water 2022, 14, 804. https://doi.org/10.3390/w14050804

Modanesi, S., Massari, C., Gruber, A., Lievens, H., Tarpanelli, A., Morbidelli, R., and De Lannoy, G. J. M. **Optimizing a backscatter forward operator using Sentinel-1 data over irrigated land, Hydrol.** Earth Syst. Sci., 25, 6283–6307, https://doi.org/10.5194/hess-25-6283-2021, 2021.

Modanesi, S., Dari, J., Massari, C., Tarpanelli, A., Barbetta, S., De Lannoy, G. J. M., Gruber, A., Lievens, H., Bechtold, M., Quast, R., Vreugdenhil, M., Zribi, M., Le Page, M., Brocca, L. **A comparison between satellite- and model-based approaches developed in the ESA Irrigation+project framework to estimate irrigation quantities**. IEEE International Workshop on Metrology for Agriculture and Forestry (MetroAgriFor), 2021, pp. 268-272, doi: 10.1109/MetroAgriFor52389.2021.9628453, 2021.

Massari, C., **Modanesi, S**., Dari, J., Gruber, A., De Lannoy, G.J.M., Girotto, M., Quintana-Seguí, P., Le Page, M.; Jarlan, L., Zribi, M., Ouaadi, N., Vreugdenhil, M., Zappa, L., Dorigo, W., Wagner, W., Brombacher, J., Pelgrum, H., Jaquot, P., Freeman, V., Volden, E., Fernandez Prieto, D., Tarpanelli, A., Barbetta, S., Brocca, L. **A Review of Irrigation Information Retrievals from Space and Their Utility for Users.** Remote Sens., *13*, 4112. https://doi.org/10.3390/rs13204112, 2021.

De Santis, D., Biondi, D., Crow, W.T., Camici, S., **Modanesi, S.**, Brocca, L., Massari, C. **Assimilation of Satellite Soil Moisture Products for River Flow Prediction: An Extensive Experiment in Over 700 Catchments Throughout Europe** Water Resour. Res., 57, (6), Article e2021WR029643, https://doi.org/10.1029/2021WR029643, 2021.

Modanesi, S., Massari, C., Camici, S., Brocca, L., Amarnath, G. **Do satellite surface soil moisture observations better retain information about crop-yield variability in drought conditions?** Water Resour. Res., 56, (2), Article e2019WR025855, https://doi.org/10.1029/2019WR025855, 2020.

Azimi, SH., Dariane, A.B., **Modanesi, S.**, Marschallinger, B.B., Bindish, R., Wagner, W., Massari, C. **Understanding the benefit of Sentinel 1 and SMAP- era satellite soil moisture retrievals for flood forecasting in small basins: effect of revisit time and spatial resolution.** Journal of Hydrology, 581. DOI: 10.1016/j.jhydrol.2019.124367, 2019.

Bauer-Marschallinger, B., Naeimi, V., Cao, S., Paulik, C., Schaufler, S., Stachl, T., **Modanesi, S.**, Massari, C., Ciabatta, L., Brocca, L., Wagner, W. **Towards Global Soil Moisture Monitoring with Sentinel-1: Harnessing Assets and Overcoming Obstacles.** IEEE Trans. Geosci. Remote Sens. DOI: 10.1109/TGRS.2018.2858004, 2018.

Bauer-Marschallinger, B., Paulik, C., Hochstöger, S., Mistelbauer, T., **Modanesi, S.**, Ciabatta, L., Massari, C., Brocca, L., Wagner, W. **Soil Moisture from Fusion of Scatterometer and SAR: Closing the Scale Gap with Temporal Filtering.** Remote Sens. 2018, 10(7), 1030. https://doi.org/10.3390/rs10071030, 2018.

Conferences contributions

Modanesi, S., Massari, C., Bechtold, M., Tarpanelli, A., Brocca, L., Lievens, H., Dorigo, W., Zappa, L., De Lannoy, G.J.M. Benefits of Sentinel-1 backscatter assimilation to improve land surface model irrigation estimates in Europe. Accepted for oral presentation at EGU 2022, 23-27 May 2022, Wien, Austria.

Bechtold, M., **Modanesi, S.,** Lievens, H., Brangers, I., Getirana, A., Gruber, A., Massari, C., Gabrielle, G.J.M. Assimilation of Sentinel-1 backscatter into a land surface model for soil moisture and leaf area index updating: Impact on streamflow simulations. Accepted for oral presentation at EGU 2022, 23-27 May 2022, Wien, Austria.

Bechtold, M., **Modanesi, S.,** Lievens, H., Brangers, I., Getirana, A., Gruber, A., Massari, C., De Lannoy, G. **Updating Soil Moisture and Vegetation by Assimilating Sentinel-1 Backscatter: Impact on Streamflow Simulations.** AGU Fall Meeting. 13-17 December 2021, New Orleans, USA.

Bechtold, M., **Modanesi, S.,** Lievens, H., Brangers, I., Getirana, A., Gruber, A., Massari, C., De Lannoy, G. **Updating soil moisture and vegetation by assimilating Sentinel-1 backscatter: Impact on streamflow simulations.** ECMWF workshop - Connecting global to local hydrological modelling and forecasting: scientific advances and challenges. Online session, 29 June - 1 July 2021.

Modanesi, S., Massari, C., Gruber, A., Brocca, L., Lievens, H., Morbidelli, R., De Lannoy, G. J., M. **On the ability of Sentinel-1 backscatter to detect soil moisture and vegetation changes caused by irrigation fluxes over the Po River Valley (Italy)**. vEGU General Assembly 2021. Online session, 19 -30 April 2021.

Modanesi, S., Massari, C., Gruber, A., Brocca, L., Lievens, H., Morbidelli, R., De Lannoy, G. J., M. **Irrigation detection over the Po River Valley (Italy) using Sentinel-1 radar backscatter observations.** Earth Observation for Water Cycle Science 2020. Online session. 16-19 November 2020.

Modanesi, S., De Lannoy, G. J. M., Gruber, A., Massari, C., Brocca, L., Lievens, H., Morbidelli, R. **Irrigation detection with Sentinel-1 radar backscatter observations over an agricultural area in**

the Po River Valley (Italy). EGU General Assembly 2020. Online session.

Modanesi, S., Massari, C., Camici, S., Brocca, L., Amarnath, G. **On the relation between satellite soil moisture and crop production during drought events in India**. AGU Fall Meeting 9 – 13 December 2019, San Francisco, USA.

Santi, E., Paloscia, S., Pettinato, S., Fontanelli, G., Brocca, L., Ciabatta, L., Massari, C., **Modanesi, S. Combining SMAP and Sentinel-1 by means of Neural Networks to improve the Soil Moisture retrievals**. H SAF and HEPEX joint workshop on "Satellite inspired hydrology for an uncertain future", 25-28 November 2019, Reading, UK.

Modanesi, S., Massari, C., Camici, S., Brocca, L., Amarnath, G. **Performance of a Standardized Soil Moisture Index based on the ESA-CCI soil moisture product for assessing agricultural drought in India**. H SAF and HEPEX joint workshop on "Satellite inspired hydrology for an uncertain future", 25-28 November 2019, Reading, UK.

Brocca, L., Camici, S., **Modanesi, S.,** Filippucci, P., Ciabatta, L., Massari, C., Hahn, S., Wagner, W., Campione, E., Puca, S., Cacciamani, C. **Operational services of satellite soil moisture products for flood, landslide, drought and precipitation.** EMS Annual Meeting 2019, 9-13 September 2019, Copenhagen, Denmark.

Modanesi, S., Massari, C., Camici, S., Brocca, L., Amarnath, G. **Utility of a Standardized Soil Moisture Index based on satellite data in estimating crop yield during drought events**. Giornate dell'Idrologia, 16-18 September 2019, Bologna, Italy.

Brocca, L., Camici, S., Ciabatta, L., Tarpanelli, A., **Modanesi, S.**, Filippucci P., Massari C., Brunetti M. T., Peruccacci S., Gariano S. L., Melillo M. **Recent advances in using satellite soil moisture and precipitation for flood and landslide prediction in the Mediterranean basin**. EGU General Assembly 2019. 7-12 April 2019. Wien, Austria.

Modanesi, S., Massari, C., Camici, S., Brocca, L., Amarnath, G. **Performance of a drought Standardized Soil Moisture Index based on ESA CCI Soil Moisture product: validation in India using crop data.** EGU General Assembly 2019. 7-12 April 2019. Wien, Austria.

Azimi, S., Massari, C., Darian, A. B., **Modanesi, S.,** Filippucci, P., De Santis, D., Maschallinger, B. B., Wagner, W. **Benefit of coarse- and medium-scale satellite soil moisture products for flood modelling in small basins: temporal versus spatial resolution**. EGU General Assembly 2019. 7-12 April 2019. Wien, Austria.

Modanesi, S., Massari, C., Camici, S., Brocca, L., Amarnath, G. **ESA-CCI soil moisture for agricultural drought: validation by using crop data.** 16th Plinius Conference on Mediterranean Risks, 9–11 October 2018. Montpellier, France.

Modanesi, S., Massari, C., Camici, S., Brocca, L., Amarnath, G. **ESA-CCI soil moisture for agricultural drought in India: validation by using crop data**. Giornate dell'Idrologia, 18-20 June

2018, Rome, Italy.